Electronic and Structural Dynamics of Complex Materials

Nicky Dean

Jesus College, Oxford

Submitted for the degree of Doctor of Philosophy

Trinity Term 2010

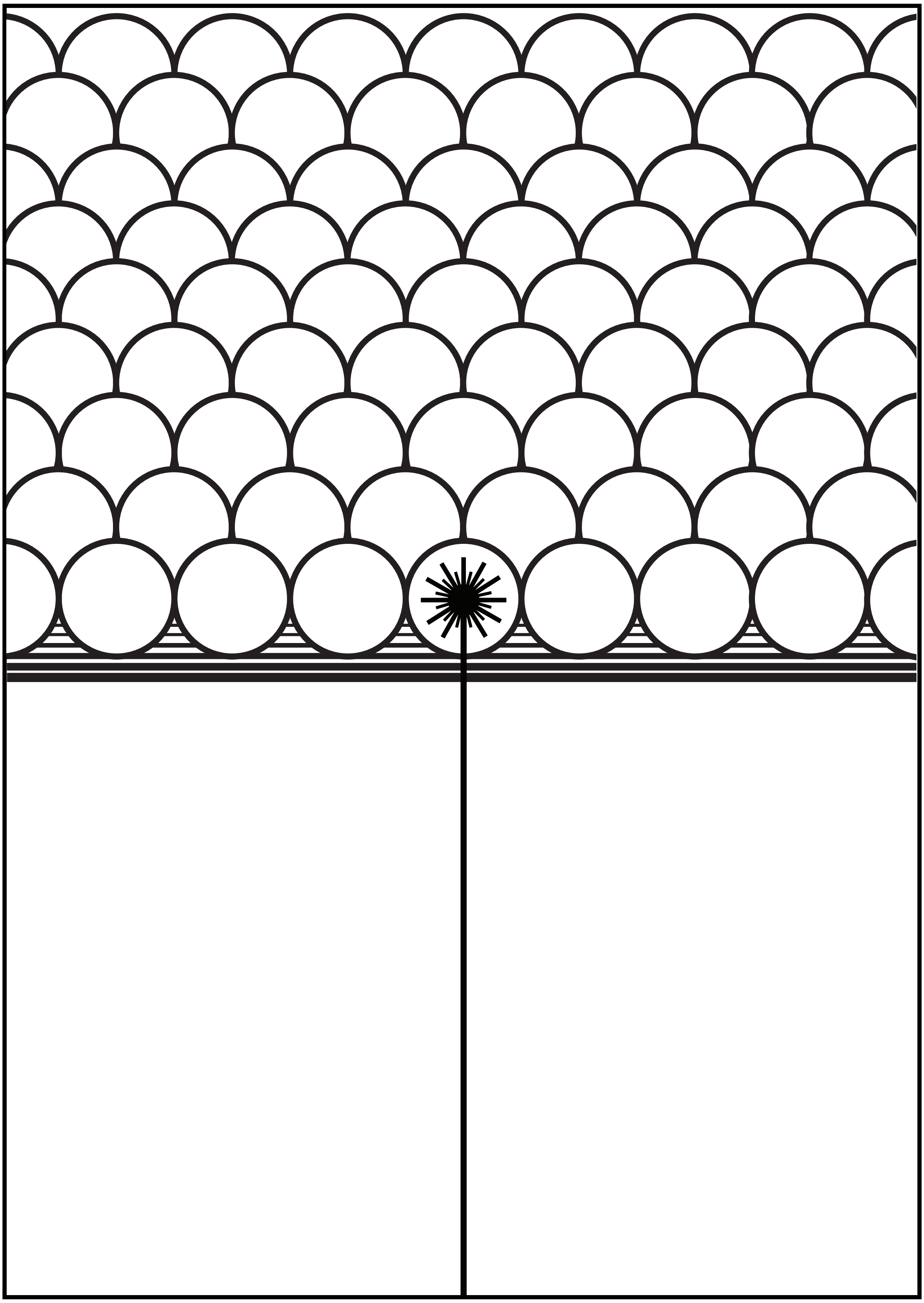

Illustration by Joey Dean.

for my family

Wake, butterfly -
It’s late,
We’ve miles to go together.
— Bashō

Abstract

The time-resolved determination of dynamics in complex materials is an important goal for understanding and controlling material properties, especially on ultrafast timescales. This thesis reports on the development of broadband spectroscopic techniques for characterising electronic and structural dynamics in such materials and their application to the quasi-two-dimensional charge-density-wave Mott insulator $1T$-TaS_2. The experiments take two main approaches. First, optical pump-probe spectroscopy from the terahertz to the visible regions of the electromagnetic spectrum is used to investigate the collective response. Secondly, time- and angle-resolved photoemission spectroscopy monitors single-electron dynamics on the earliest timescales across the Brillouin zone.

In the photoinduced phase of TaS_2, terahertz spectroscopy demonstrates an increase in conductivity as the phase transition occurs and reveals the evolution of three phonon modes, which undergo transient Fano reshaping due to electron-lattice interactions. Pump-probe measurements at higher energy highlight coherent excitation of the charge density wave amplitude mode and the emergence of a broad resonance feature associated with polaron formation in the new phase. The photoemission experiments show that photoexcitation causes prompt collapse of the Mott gap and leads to partial unfolding of the Brillouin zone on longer timescales, as structural distortions relax.

The emerging picture of this transient phase is one in which the Mott gap is melted but the low-temperature symmetry is retained. Meanwhile, transport is dominated by polaronic conductivity. This unique phase is only accessible by photo-doping.

Finally, a new method of ultrafast control, in which light is coupled to vibrational modes of the system rather than electronic excitations, is introduced and demonstrated in the manganites. An exploration of this technique using FELs promises to reveal the role of different types of distortion in driving ultrafast processes, while phase stabilisation of excitation pulses opens up new paths to coherent control.

Role of the author

Many of the experimental results presented in this thesis were obtained in the Oxford laboratory of the Cavalleri Group. Others were taken elsewhere as part of multi-national collaborations. Unless otherwise clearly stated, the data acquisition and analysis was performed by the author.

The pulse characterisation schemes in chapter 3 were built by the author, who also took the measurements.

In chapter 4, the terahertz spectroscopy system presented was designed and built by the author and R. Tobey. The derivation of optical constants from time-resolved terahertz measurements was performed by the author with assistance from J. Petersen.

All of the experimental apparatus described in chapter 5 was designed and built by the author and R. Tobey, with additional help from D. Fausti. The results presented were all taken and analysed by the author, with helpful input from J. Petersen and S. Kaiser. L. Gasparov provided the static FTIR data.

The time- and angle-resolved photoemission spectroscopy measurements in chapter 6 were carried out on the Artemis beamline at the Central Laser Facility, as part of a collaboration involving J. Petersen, S. Kaiser, the author, A. Simoncig, A. L. Cavalieri, and C. Cacho.

In chapter 7, the laboratory-based results in $Pr_{0.7}Ca_{0.3}MnO_3$ were taken by R. Tobey and the author, in collaboration with M. Rini at the Lawrence Berkeley National Laboratory, USA and A. Cavalleri. The free electron laser experiments were carried out at the FELBE facility at the Forschungszentrum Dresden-Rossendorf, Germany. The optical switch was designed and built by S. Winnerl and W. Seidel. The remainder of the experimental apparatus was designed and built by M. Gensch and the author. The data presented were acquired by M. Gensch, the author, and N. Stojanovic, with assistance from S. Winnerl and W. Seidel. The carrier–envelope phase stable measurements were conceived by A. Cavalleri. The apparatus was designed and built by the author, who also took the measurements presented.

Acknowledgements

To say that I have enjoyed my time as a D.Phil student is something of an understatement. It has been an eye-opening experience which has enabled me to travel to many exciting places all over the world. And to Long Island. For this I am deeply indebted to my supervisor, Andrea Cavalleri, without whom I would never have stumbled upon this fascinating field of physics. His enthusiasm seems to know no bounds, and his personal support was a great help whenever anything was refusing to do as it was supposed to.

As far as the rest of the research group is concerned, I couldn't have been luckier with the selection of colleagues. Scientifically, they were invaluable, even as I stared blankly back at them in ignorance. Special mention must go to Ron Tobey for teaching me how to put an experiment together in the first place. Socially, they have been some of the best friends I have ever made. The early days with Ron and Simon Wall will be fondly remembered, as will late nights in the Hi-Lo with Julia Stähler, Jesse Petersen, Daniele Fausti, and Andreas Dienst. I should also like to thank Jesse for still talking to me after all those endless weeks at RAL in the cold.

As one of the loudest and most disruptive people in the Simon Room, I also owe a debt of thanks to the rest of my office, who made it a fun and pleasant working environment. Kevin O'Keeffe was a man of constant surprises, and I have missed Charlotte Woolley's presence on Saturdays dearly these last few months.

I am grateful for the support of my housemates George Duncan-Jones, Fil Wyszynski, and Melissa Coll-Smith, who seemed to enjoy my grumbling more than anyone really ought to. The endless gossiping and nights rounded off at the Fir Tree will be sorely missed, along with my strolls in the park and visits to the ducks with George. I owe a great deal to Matt Gray, who was always ready with a wrap and a bowl of soup when needed. The constitutionals, the trips to Blackwell's, and the hunts for pretzels came to define a large part of my life in the last four years. I would also very much like to thank Jojo, Shani, and all the girls who broke my heart at the Woodstock Road Deli, for keeping me in fresh supply of butter beans, pasta, coleslaw, cheese, and basil pesto.

Finally, I would like to thank my parents and my brothers for their continued support and encouragement through all this. I couldn't have done it without them.

Contents

Figures

1 Introduction 1

2 Tantalum Disulphide 9

3 Aspects of Ultrafast Spectroscopy 21

4 Terahertz Time-Domain Spectroscopy 35

Chapter 1

Introduction

1.1 Capturing Dynamics

This year sees the fiftieth anniversary of the laser, and while it may have started out life as a scientific curiosity, the great ‘solution looking for a problem’ [1], it has since become one of the most ubiquitous pieces of technology in existence, finding a home for itself in environments as diverse as the research laboratory, the hospital, and the living room. At its birth, many considered the laser as little more than a death ray [2], undoubtedly fuelled by Cold War paranoia [3]. Scientists working on laser development had other ideas. Shortly after demonstrating the first working laser [4], Theodore Maiman described the five potential applications he foresaw for his creation: (i) true amplification of light; (ii) increasing the number of communication channels; (iii) probing matter for basic research; (iv) high-power beams for space communications; (v) concentrating light for industry, chemistry, and medicine [5].

With the subsequent decades of intense laser research and development, the probing of matter has become an important area of research for the laser. This is especially true with pulsed lasers, which can be used to trigger and measure dynamical behaviour in solids on extremely fast timescales.

Such time-resolved measurements capture snapshots of an event as it happens, which can then be built up into a full sequence, mapping out exactly what is going on at any given time. In the late 19th century, Eadweard Muybridge performed one of the first ever time-resolved

Figure 1.1: *'Plate Number 156. Jumping; running straight high jump'* by Eadweard Muybridge (1887), courtesy of Corcoran Gallery of Art, Washington, DC [6]. These early time-resolved photographs were used to understand dynamical motion of people and animals.

experiments when he captured Leland Stanford's horse in motion, settling the debate as to whether or not a horse's hooves are ever all off the ground at the same time. Muybridge used a series of cameras with high shutter speeds, each triggered by a trip wire, to capture the horse at different points in its gallop. Each exposure was short enough to clearly capture the horse at a distinct point in its motion, revealing for the first time the nature of its movements, previously too fast to be resolved by the eye. Muybridge went on to capture an enormous number of dynamical events from both animals and humans, unveiling their actions for all to see [7]; an example of such a measurement is shown in figure 1.1.

This concept can be applied to laser-based time-resolved experiments used to study physical, chemical, and biological processes. In the contemporary version of Muybridge's measurements, the cameras are replaced by laser pulse trains, with their short pulse durations acting as the high-speed 'shutters'. A first intense pulse is used to initiate dynamics in the system under scrutiny. Then a second laser pulse interacts with the system, becoming encoded with information about its properties at the moment of arrival. By changing the relative time delay between the pulses a series of snapshots is created, providing an image of the system's evolution, much like Muybridge's images captured their subjects in motion. This technique lies at the heart of the pump-probe experiment.

In order for these snapshots to be of any use, regardless of the century, they need to clearly resolve what they are measuring. Any image taken of a dynamic event captures its progress throughout the exposure time. If the system being observed is changing during this period, then the image gets blurred, and whilst this leads to interesting photographic effects, it is not helpful in providing information on what is actually happening. Thus it becomes crucial to reduce the exposure time to a timescale comparable to or shorter than the event taking place. It is this principal which allowed Muybridge to understand the movements of racehorses and which allows scientists to understand the motion of atoms and electrons in all manner of processes around us.

1.2 The Ultrafast Regime

Time-resolved science has garnered two Nobel Prizes, marking important milestones in the speed with which dynamical events can be recorded. In 1967, the Nobel Prize in Chemistry was awarded to Manfred Eigen, Ronald G.W. Norrish, and George Porter *'for their studies of extremely fast chemical reactions, effected by disturbing the equilibrium by means of very short pulses of energy'* [8]. They were able to monitor chemical reactions taking place on microsecond (10^{-6} seconds) and nanosecond (10^{-9} seconds) timescales. The rapid growth in femtosecond technology in the '80s and '90s paved the way for the second prize, awarded to Ahmed Zewail in 1999 *'for his studies of the transition states of chemical reactions using femtosecond spectroscopy'* [8]. By using light in a manner similar to that described earlier, Zewail was able to capture reactions taking place on picosecond (ps, 10^{-12} seconds) and femtosecond (fs, 10^{-15} seconds) timescales.

Processes occurring on such short timescales are referred to as 'ultrafast' processes. They include not only chemical reactions, but also many operations taking place in solid state systems, where the nature of interactions and ordering in a crystal gives rise to an abundance of ultrafast effects. The continuing development of ultrafast laser sources, and the ever-shorter probes they provide, has enabled a great deal of progress to be made in observing and understanding these fundamental processes, extending the approach of Zewail in new and exciting directions.

In addition to studying underlying interactions, ultrafast technology has opened up the ability to control matter in new ways. Using laser radiation, material systems can be driven into new non-equilibrium states, inaccessible by more traditional methods. The properties of these new meta-stable phases can be controlled and altered by varying the properties of the driving laser, suggesting a wealth of potential technological applications based on short-lived or rapidly-changing effects.

1.3 Strongly Correlated Electron Materials

Oftentimes, when trying to describe the electronic properties of solids, conventional band theory is invoked. Within this framework, electron-electron interactions are ignored and each electron is treated as independent from the rest. The electrons occupy atomic orbitals, which form a set of discrete energy levels. When the atoms are brought into a crystal formation, these energy levels become very close and form bands, which are separated by energy gaps. The number of electrons in a band and the size of the gap separating successive bands dictates the properties of the solid. Band theory has proved immensely successful at describing the electronic properties of many materials, such as metals, insulators, and semiconductors.

However, this independent-electron model is only an approximation to the true behaviour, albeit a very good one in many cases. In reality, the electrons are interacting with one another all the time. As the strength of the interactions becomes increasingly important, the independent-electron picture begins to break down and the predictions of band theory no longer match the observed behaviour. This is the realm of strongly correlated electron, or complex, materials. These are materials in which the Coulomb interaction between electrons is larger than their kinetic energy, meaning an electron remains on a given lattice site long enough to feel the presence of other electrons nearby. This results in a large number of exotic ordered states and unusual phase transitions. The properties of such materials are often vastly different to those predicted by conventional band theory [9, 10].

In general, it is not just the inter-electron correlations which are important, but also the correlation between the electrons and many other degrees of freedom, such as the lattice. The ground state properties of a complex material are then determined by the competition between these various interactions. If several different couplings are competing on similar energy scales, then these properties become very sensitive to subtle perturbations, resulting in a variety of different phases. This complex interplay produces such fascinating effects as superconductivity, where electron-lattice coupling not only reduces the electronic bandwidth, but also creates an attractive force between the electrons, leading to the formation of Cooper pairs [11].

The properties of correlated materials can be controlled by changing the strength of different interactions, causing some to become more prevalent than others. Typically, this involves the application of pressure or magnetic or electric fields, varying the temperature, or chemical doping, which adds or removes electrons from the system. Tipping the balance in this way produces interesting phase transitions separated by only small differences in energy [12]. Understanding the nature of these couplings is vital to understanding the macroscopic behaviour of the material.

1.4 Photoinduced Phenomena

In addition to those methods of control mentioned above, the properties of a material can also be perturbed using light. Unlike those methods, photoexcitation is a non-adiabatic process, shaking the system up in a highly non-equilibrium fashion. The effects of photoexcitation can vary depending on the material properties and nature of the light used, and range from simple carrier excitation to photoinduced structural and electronic phase transitions. Many different types of dynamics can arise from photoexcitation, and studying them can reveal a lot about the nature of the underlying interactions in the solid.

Photoexcitation has been used in semiconductors for a long time to understand carrier relaxation and early-timescale dynamics in both absorption spectroscopy [13, 14] and, more recently, THz spectroscopy [15]. The parallels between photoexcitation and chemical doping have led to the process often being described as ‘photo-doping’ [16].

Light is also frequently used for controlling the behaviour of a material through photoinduced phase transitions [17]. In these types of transition, excitation of electrons upsets the interplay between degrees of freedom, driving the system into a new regime where its properties can become quite different: structural relaxation can take place, shifting the positions of ions towards some new symmetry position [18–20], the optical properties can undergo large-scale changes [21], and metallic states can be formed [22]. All of these effects last for only fractions of a second, with the system eventually relaxing back to its equilibrium state.

1.5 Characterising Ultrafast Behaviour

The range of tools available for studying ultrafast processes has blossomed in the last couple of decades. The frontiers of ultrafast science continue to explore ever shorter timescales, studying effects on the scale of a few femtoseconds [23, 24] and pushing on into the attosecond (10^{-18} seconds) regime [25]. Observing the collapse of gaps after photoexcitation on the fastest timescales and clocking the rate at which processes occur can reveal a great deal of information on the formation of states in complex materials.

However, whilst these endeavours provide insight into the fundamental timescales and electronic interactions, there is still the important task of characterising the dynamics of photoinduced phases in solids. In the same way that it is important to fully determine the equilibrium properties of a material by studying its electrodynamic response over a broad energy range, a full understanding of photoinduced phenomena can only be attained by looking across different energy scales. This requires an array of different ultrafast probes covering large portions of the electromagnetic spectrum, from terahertz (THz, 10^{12} Hz) frequencies, up through the infrared and visible spectrum, and into the ultraviolet and X-ray regions.

Time-resolved analogues of established static techniques such as X-ray diffraction, which can provide information on the ordering of electronic states [26, 27], and photoelectron spectroscopy, which maps out the band structure as photoinduced processes occur [28, 29], are powerful tools in approaching a fuller appreciation of the effects of photoexcitation.

It is the aim of this thesis to develop a series of sophisticated characterisation techniques to produce a more detailed depiction of the photoinduced phases of complex materials, focussing on the intriguing Mott-insulating charge-density-wave compound $1T$-TaS$_2$. This necessitates the use of a variety of different ultrafast probes, all based on the same stroboscopic experimental principal outlined at the start of this chapter, making use of photon energies from the milli-electron volt scale up to tens of electron volts.

The methods employed will take two routes, each of which interrogates the system in a slightly different manner. Broadband optical spectroscopy measurements offer insight into the transport properties and collective behaviour of the system, capturing dynamics between 1 meV and 1 eV during the first few picoseconds after photoexcitation. Meanwhile, time- and angle-resolved photoelectron spectroscopy gives information on the single particle picture, providing momentum-resolved snapshots of the evolution of the electronic band structure during the onset of the photoinduced phase transition. The combination of these techniques allows for detailed characterisation of the electronic and structural dynamics of photoinduced phases in complex materials. By widening the window over which ultrafast processes are observed, a richer understanding of the exotic phases accessible with light may be achieved.

Chapter 2

Tantalum Disulphide

2.1 Transition Metal Dichalcogenides

Throughout the 1960s and 1970s, layered transition metal dichalcogenides were the subject of intense experimental scrutiny [30, 31], and they continue to find themselves constantly under the microscope to this day [32–38]. This class of materials is interesting due to its two-dimensional behaviour, which results in a wide variety of phenomena, from ordinary insulating and metallic behaviour, to semimetallic and superconducting properties [30, 38]. It has also proven a rich hunting ground for various types of charge and spin density wave ordering [39–41], as well as Mott and Peierls transitions [42, 43].

Two phenomena have emerged as the dominant features of transition metal dichalcogenides: the formation of various types of charge density wave state and the existence of a Mott insulating phase at low temperatures. This chapter will first discuss these phenomena in more detail, before elaborating further on a specific transition metal dichalcogenide, $1T$-TaS$_2$, in which these two effects play a key role.

2.2 Charge Density Waves

In materials with highly anisotropic band structures, electron-electron and electron-phonon interactions can lead to new ground states and collective excitations known as charge density waves (CDWs). Such ground states occur predominantly in low-dimensional materials, and are especially prevalent in one-dimensional systems [43, 44]. Their name aptly describes the

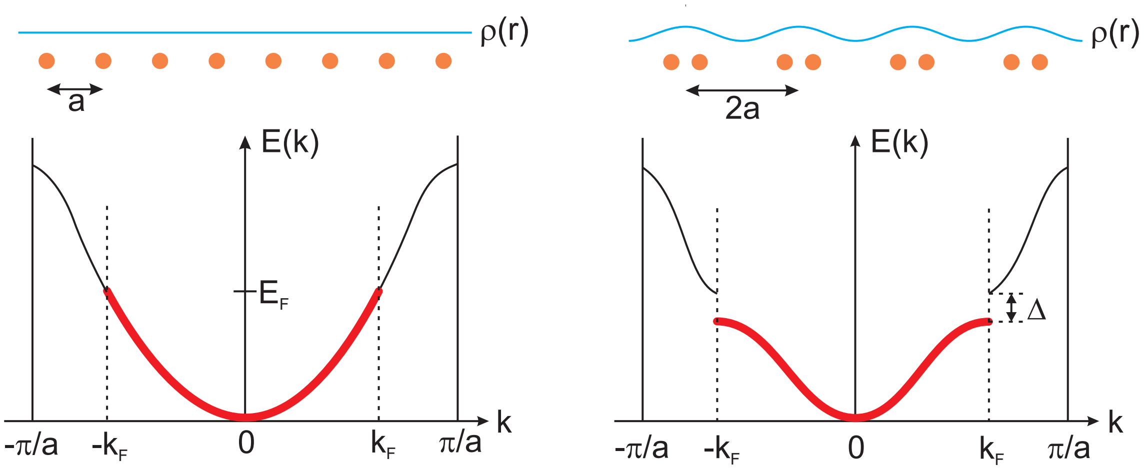

Figure 2.1: The Peierls distortion in a 1D metal. Left: undistorted metal chain. Right: the Peierls distortion turns the metal into an insulator. Light blue lines at the top of the figure show the spatial charge density, $\rho(r)$, and orange dots represent atoms. The lower portion describes the dispersion relation in both cases, with red lines indicating occupied states.

salient feature of the CDW ground state: a periodic charge density modulation throughout the crystal, accompanied by a periodic lattice distortion.

The formation of the CDW is usually explained through the simple one-dimensional model of the Peierls transition [45]. In the absence of electron-electron and electron-phonon interactions, a linear chain of atoms is separated by a distance a, with each atom representing a lattice point and with one atom per unit cell. The electrons occupy states up to the Fermi energy E_F, and the dispersion relation is that of a free electron gas. This situation is illustrated on the left of figure 2.1. If an electron-phonon interaction is introduced and the chain is distorted to shift every other atom slightly, as shown in the top right of figure 2.1, then the unit cell doubles in size, halving the Brillouin zone. A gap opens at the new Brillouin zone boundary, $k = \pi/2a$, turning the previously metallic chain into an insulator. In this one-dimensional case, the reduction in energy at the Fermi surface is greater than the elastic energy required for the lattice distortion [46], meaning a one-dimensional chain cannot be a metal.

The other consequence of the modified dispersion relation is a modulation of the charge density along the chain. As indicated in the top right of figure 2.1, the periodic lattice distortion creates a spatially varying distribution of charge of the form $\cos(\rho x + \phi)$. This

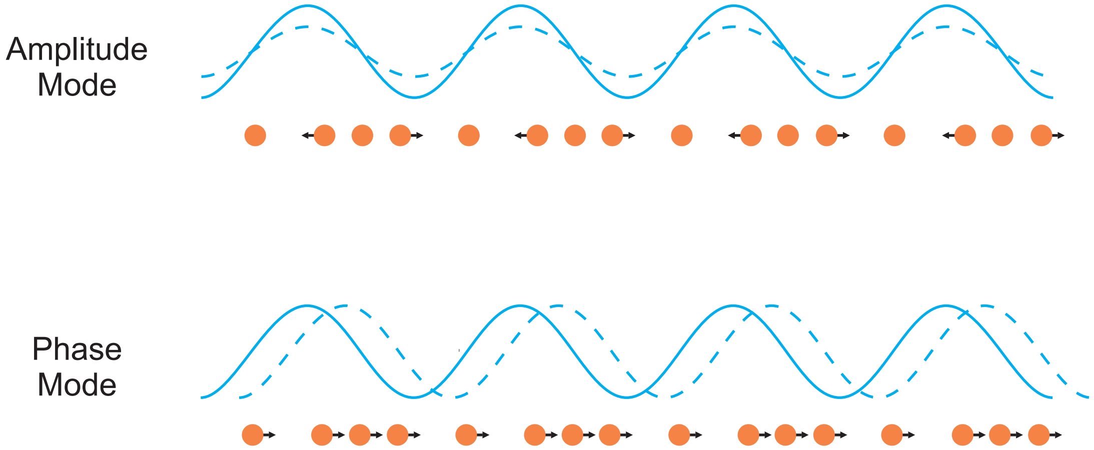

Figure 2.2: Excitations of the charge density wave state. Lines show changes to the charge density whilst dots are the ions. Arrows indicate the changes in the ion position.

charge density is associated with a new collective mode of the condensate called the charge density wave [44, 46].

The spatial modulations of electronic density and lattice displacement of the CDW state are described by a complex order parameter $\Psi \propto \Delta e^{i\phi}$, much like superconductors. This makes it possible to have excitations of both amplitude (Δ) and phase (ϕ). These two modes can be seen in figure 2.2 for the $k = 0$ case. Phase excitations, or phasons, represent translations of the condensate (in the limit of $k = 0$). The electronic charge density is displaced relative to the ions, resulting in a dipole moment, so the phason is optically active. Amplitude excitations, or amplitudons, represent changes in the charge density amplitude throughout the lattice. There is no displacement of the charge density relative to the ions, and so no dipole moment; as such, amplitudons are Raman active [44].

CDW materials are intensely studied, especially due to their close connection with superconductivity [47, 48]. They also provide an ideal playground for time-resolved studies, where the excitation of the CDW modes or collapse of the CDW gap leads to understanding of the collective behaviour of the system [35, 49]. Their prominent role in the transition metal dichalcogenides, and TaS_2 in particular, make a basic understanding of their properties essential.

2.3 Mott Insulators

Band theory is enormously successful at describing the electronic properties of materials where electrons can be treated as independent from one another. However, as electron correlations become stronger, this theory begins to break down and the measured properties can become vastly different from the predictions. This was first noticed in the case of transition metal oxides by de Boer and Verwey [50]. A class of these compounds have only partially filled $3d$ bands, and so in the context of band theory they should be conductors; in fact, they turn out to be insulators. This was subsequently explained by considering electron-electron interactions [51].

Mott went on to describe how electron-electron interactions could suppress metallic behaviour in favour of an insulating state in NiO [9]. If an electron hops from one atom to another, it leaves behind it a positively charged hole. The electron and hole attract each other with a force resulting from the potential $U \propto -e^2/r$, where e is the electron charge and r is the electron-hole separation. Mott reasoned that the existence of electron-hole pairs would screen the field between an electron and a hole, reducing the potential to $U \propto -(e^2/r)\exp(-qr)$, where q depends on the density of electron-hole pairs. If the density of pairs becomes large enough then the potential U will no longer support bound states of electrons and holes and the system can conduct. Crucially, it is the Coulomb potential which is the dominant factor, with a large U causing electrons to be localised on-site.

Hubbard took Mott's ideas and used them to formulate an approximate model for the Hamiltonian of a system with strong electron-electron interactions, demonstrating how the transition between the localised and non-localised states may occur. The theory produced the Mott-Hubbard Hamiltonian [52]:

$$H = -t \sum_{<i,j>,\sigma} (c^{\dagger}_{i,\sigma} c_{j,\sigma} + h.c.) + U \sum_{i=1}^{N} n_{i,\uparrow} n_{i,\downarrow}. \tag{2.1}$$

The first term comes from the tight-binding approximation of band theory and describes the kinetic energy of the electrons, where t is the transfer integral, representing the inter-site hopping of electrons, and $c^{\dagger}_{i,\sigma}$, $c_{i,\sigma}$ are the creation and annihilation operators for an electron at site i with spin up or down ($\sigma =\uparrow, \downarrow$). t depends on the atomic separation and on the particular orbitals the electrons occupy.

The second term in the Hamiltonian arises from the on-site Coulomb repulsion of the electrons, and hence takes into account Mott's consideration of electron-electron interactions. U represents the Coulomb potential of two electrons on the same lattice site and $n_{i,\sigma} = c^{\dagger}_{i,\sigma} c_{i,\sigma}$ is the electron number operator for the spin state σ.

From this model, it may be seen that the competition between t and U drives the system between two different states, as initially described by Mott. When $t \gg U$, such that the mutual electron repulsion is weak compared to the kinetic energy, the system behaves according to the tight-binding model and band theory adequately describes its behaviour. In the other limit, $U \gg t$, the Coulomb repulsion prevents electrons from moving to occupied sites and the charges become localised. This leads to the formation of a Mott insulator, when band theory predicts metallic behaviour but the electron-electron repulsion is dominant, causing a gap to open of size

$$E_g = U - 2Nt, \tag{2.2}$$

where N is the number of nearest-neighbour atoms.

Mott insulators are of great importance in understanding the interplay between electron-electron and electron-lattice interactions. They are significant to the work of this thesis since the ground state of $\mathrm{TaS_2}$ exhibits both charge density wave and Mott characteristics, which respond independently to photoexcitation, leading to an exotic phase of this material which cannot be reached in equilibrium.

2.4 Tantalum Disulphide

2.4.1 Basic properties

Transition metal dichalcogenides have the basic chemical structure $\mathrm{MX_2}$, where M is a transition metal and X a chalcogenide. Structurally, they form sheets of X–M–X sandwiches, which are loosely bound together by van der Waals forces; it is this weak interlayer coupling which provides the quasi-two-dimensional character. Within the sandwich, the coordination of the metal atom may be octahedral or trigonal prismatic, and the different possible sandwich stackings result in a large number of possible polytypes, the simplest two of which are the pure octahedral ($1T$) and pure trigonal prismatic ($2H$) structures. However, all $\mathrm{MX_2}$ materials share hexagonal symmetry. It is this wide variation in structural as well as chemical

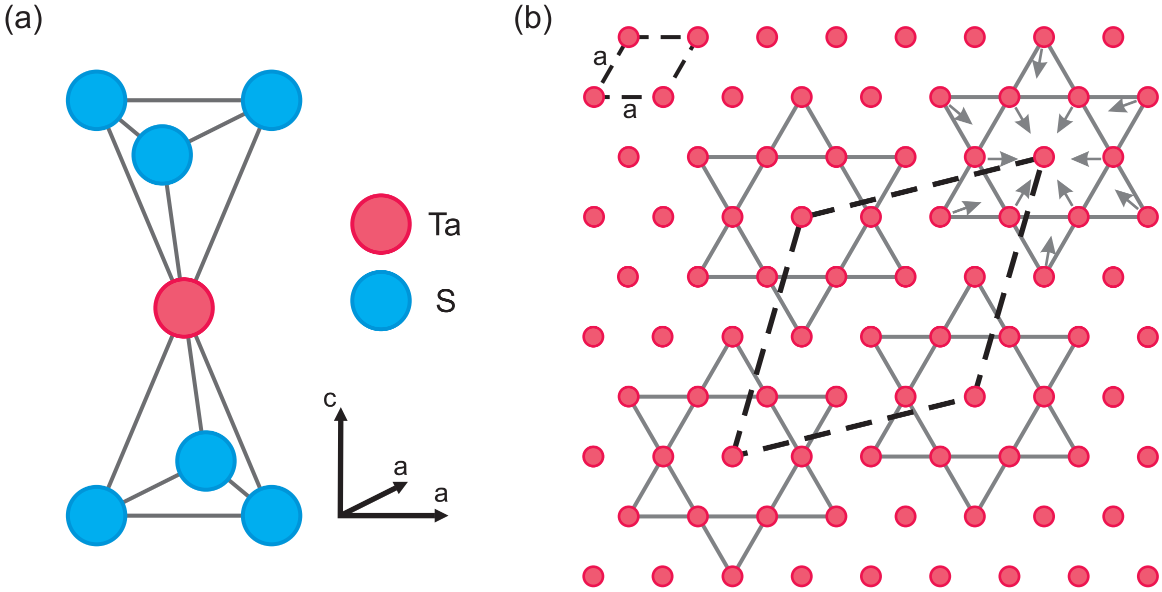

Figure 2.3: Structure of $1T$-TaS$_2$. Unit cell dimensions: $a = 3.36$ Å, $c = 5.90$ Å [53]. (a) Octahedral coordination unit forming the S–Ta–S sandwiches. (b) The Ta plane. Without the CDW, the unit cell is that shown by the dashed line in the upper left corner. With the CDW, "Star of David" cluster formation takes place, shown by the solid lines. Arrows show the displacement of Ta atoms and the dashed line connecting the stars gives the new unit cell.

properties which leads to the myriad opportunities for experimental study.

Of all the quasi-two-dimensional transition metal dichalcogenides, the $1T$ polytype of tantalum disulphide, $1T$-TaS$_2$(hereafter referred to simply as TaS$_2$), is one of the most widely studied. Its basic structure is shown in figure 2.3(a). Historically, it is notable for being the among the first two-dimensional materials in which a charge density wave was observed [31]. It also becomes Mott insulating at low temperature [54], which is intimately connected to the CDW behaviour. A number of studies have been carried out on this material, including low-energy electron diffraction [55], photoemission spectroscopy [34, 56, 57], Fourier transform infrared spectroscopy [58–60], Raman spectroscopy [32, 33, 61], and pump-probe spectroscopy [28, 35], all in the hope of understanding the relationship between the charge density wave behaviour and the Mott physics in this peculiar compound.

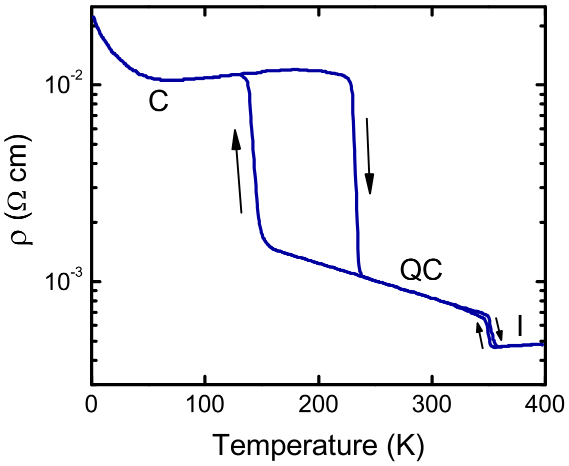

Figure 2.4: Resistivity of TaS_2 as a function of temperature for the CDW phases, taken from [53]. C, QC, and I denote commensurate, quasicommensurate, and incommensurate phases, respectively. The three phases can be distinguished by the abrupt hysteretic changes in resistivity. The arrows indicate the paths for heating and cooling.

2.4.2 Thermal phases of 1*T*-TaS_2

TaS_2 has four thermodynamic phases, separated by first-order phase transitions, and differentiated by significant differences in resistivity [53] and CDW commensuration [54, 57]. At high temperatures, $T > 550\,\mathrm{K}$, TaS_2 is metallic and no CDW is present. The structure is that of CdI_2, with space group $P\bar{3}m1$ [33, 39]. As it is cooled below $T = 550\,\mathrm{K}$, a CDW distortion occurs. The CDW is incommensurate with the underlying lattice for temperatures $550 > T > 350\,\mathrm{K}$ (I phase). Figure 2.4 shows resistivity measurements as a function of temperature, highlighting the different CDW phases. Figure 2.3(b) shows the structure of the tantalum plane; the unit cell of the undistorted and I phases is shown in the upper left corner.

Below $T_c = 180\,\mathrm{K}$, a periodic lattice distortion creates clusters of tantalum atoms in the so-called "Star of David" formation, as illustrated in figure 2.3(b). The CDW wave vector rotates 13.9° from the a-axis to become fully commensurate with the lattice (C phase), with each star cluster finding itself at the corner of a new superlattice unit cell. This new superlattice, indicated by the dashed line in the centre of figure 2.3(b), has $\sqrt{13} \times \sqrt{13}$ periodicity. Raman spectroscopy shows good separation between E_g and A_g modes, and it was therefore argued that the symmetry of the single layer best describes the symmetry of the whole crystal, leading to the symmetry assignment of $P\bar{3}$ [33].

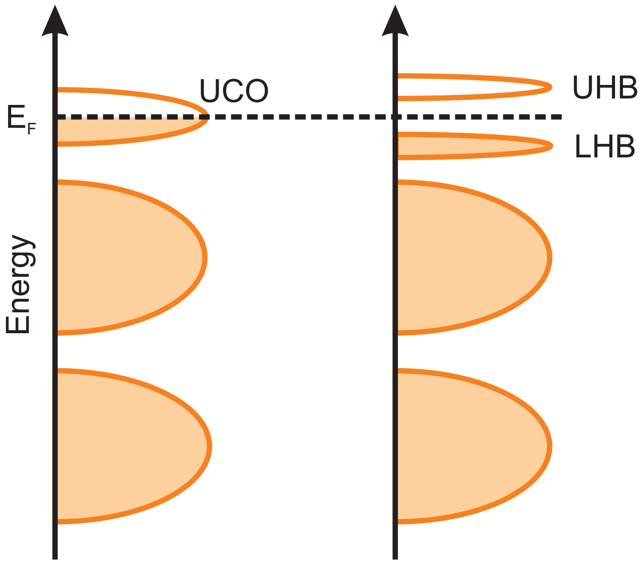

Figure 2.5: Schematic representation of the band structure of 1T-TaS$_2$. Left: the commensurate CDW splits the electrons into three manifolds, with the star-centre electron occupying the top band arising from the uppermost cluster orbital (UCO). Right: the narrow band is prone to a Mott-Hubbard transition, splitting it into two Hubbard bands (LHB and UHB).

Between these two phases, for 180 K $< T <$ 350 K, commensurate domains of stars form into a hexagonal array, with a domain size of about 70 Å [38, 62]. The domain size increases with decreasing temperature, and neighbouring domains are separated by discommensurate regions. In addition, the orientation of the domains relative to the CDW changes slightly as the C phase is approached [63]. Furthermore, as the temperature is lowered, the CDW rotates away from the lattice, starting at around 11° and ending at around 13° [63]. The angle between the lattice and the CDW never reaches the commensurate value of 13.9°; instead there is a discontinuous jump in angle on going below 180 K. Hence this phase is described as the quasi-commensurate (QC) phase. Its electronic behaviour is metallic.

2.4.3 Effects of commensuration

In the C phase, the structural distortion and resulting lock-in of the CDW to the lattice cause the electrons to pair up around the star, leaving only the electron at the star centre unpaired. The new lattice periodicity leads to reconstruction of the Brillouin zone and a collapse of the band structure into a series of manifolds [57, 64, 65], as shown in figure 2.5. The two

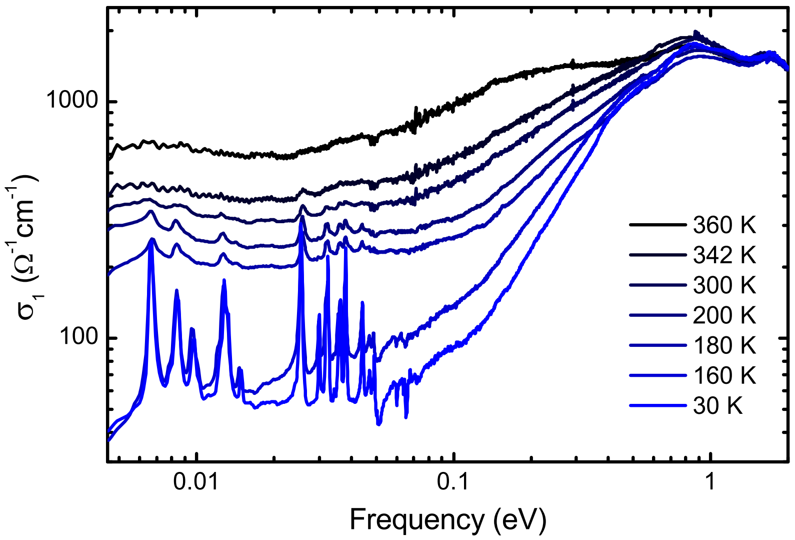

Figure 2.6: Optical conductivity of TaS_2 for a variety of temperatures in the QC and C phases, indicating the opening of a gap at 100 meV, taken from [60]. All measurements were taken upon cooling.

lower-lying bands each consist of six of the Ta 5*d* valence electrons from the outer rings of the star. The thirteenth star-centre electron sits alone above these manifolds in a narrow half-filled band straddling the Fermi energy, occupying the uppermost cluster orbital (UCO). This band is split off from higher energy bands due to spin-orbit coupling [65], whilst its small size makes it highly susceptible to Mott localisation.

Fazekas and Tosatti argued that band structure effects alone would result in TaS_2 being metallic [42, 54], as is apparent from the schematic diagram of figure 2.5. However, this could not be reconciled with the existing resistivity data, which was much larger than expected for a two-dimensional metal. They therefore proposed that Mott localisation must take place in the commensurate phase in order to explain the observed electrical properties. The Mott-Hubbard transition splits the UCO band of the zone-folded structure into lower (LHB) and upper (UHB) Hubbard bands, as indicated on the right of figure 2.5. Importantly, Fazekas and Tosatti also pointed out that the Mott localisation arises as a consequence of the CDW commensuration, and does not drive the lock-in transition [54]; it is possible to have a commensurate CDW state with metallic as well as insulating behaviour [66].

Thus it may be seen that, at $T_c = 180\,\mathrm{K}$, the CDW commensuration leads to a reduction of the bandwidth below the energy necessary for double occupation of the upper cluster orbital and a Mott gap opens in the electronic structure, with electrons becoming localised at the star-centres [34, 67, 68]. Optical conductivity measurements, shown in figure 2.6, demonstrate the drop in low frequency conductivity and opening of the gap, estimated to be at 100 meV [60]. These measurements also clearly show a large increase in the number of phonon modes as the symmetry changes between the I and C phases. Additionally, more modes become visible as the temperature is lowered due to changes in the screening of the modes by electrons.

There is one final interesting remark to be made on the adiabatic phase transitions in $1T$-TaS$_2$. It has recently been shown that below 5 K and under increasingly high pressure, the Mott phase melts giving way to a textured CDW state, similar to that of the QC phase, but with the emergence of superconductivity [38]. The superconducting phase persists even as the CDW is eventually lost. It is thought that this phase arises from commensurability effects and competition between the superconducting and CDW states.

2.4.4 Time-resolved studies

The coexistence of the charge density wave and Mott insulating states in TaS$_2$ highlights important contributions from both electron-electron and electron-phonon interactions in determining the ground state of the system. In order to gain better insight into the interplay between the two, it is necessary to dissect the system and examine effects caused by one process or the other. This is where time-resolved experiments come in: a light pulse perturbs the equilibrium state and its response is monitored on ultrafast timescales. By examining the different timescales involved as the system recovers, information can be yielded on the role of phonons and electrons in the ground state.

Initial time-resolved explorations in TaS$_2$ looked at the response to photoexcitation in the near-infrared [35, 69, 70]. These experiments studied both single particle and collective excitations by monitoring changes in the reflectance at a single frequency following excitation. They found further evidence for the existence of a gap at T_c as well as the excitation of the coherent CDW amplitude mode at 2.4 THz. The temperature dependence of the frequency and width of this mode was examined and found to show hysteresis effects in agreement with previous Raman spectroscopy measurements [32, 33]. Furthermore, the single particle dynamics were strongly influenced by the transition at T_c, with a marked drop in the amplitude and decay time of the reflectance change on going from the insulating to metallic states. This observation describes the importance of commensuration in the C and QC phases: the lack of a fully commensurate CDW results in rapid dephasing of the coherent oscillations and hence strong damping of the distortions.

Time-resolved photoemission spectroscopy measurements on $\mathrm{TaS_2}$ then helped develop a clearer understanding of the electronic and phononic excitations in this compound [28, 37]. The technique enables a mapping of the electron states close to the Fermi energy in time as they respond to photoexcitation. Similar oscillatory behaviour to the near-infrared experiments was observed in the QC and C phases. Crucially, however, the photoemission spectroscopy measurements revealed a prompt collapse of the Mott gap at $k = 0$. This occurs on a timescale short compared to the amplitude mode period (i.e. less than 100 fs) and was found to recover with a time constant of ~ 680 fs.

This important work provided two key pieces of information in the study of $\mathrm{TaS_2}$. First, the time-dependent behaviour of the LHB showed that the ground state was indeed a Mott insulator, rather than a Peierls insulator. Whilst the nature of the ground state was not strongly contested, little hard evidence had arisen until this point to conclusively prove that the gap was of electronic rather than structural origin. This also highlights the importance of such time-resolved experiments in unpicking the contributions of electron-electron and electron-phonon interactions to the equilibrium properties.

The second, and perhaps more interesting, piece of information uncovered was the existence of a photoinduced insulator–metal phase transition in $\mathrm{TaS_2}$, as evidenced by the collapse of the gap seen in the photoemission spectra. By comparing the time-dependent measurements with theoretical spectra, it was concluded that the transition is caused by an elevated electron temperature, with only minor contributions due to photo-doping. The photoinduced phase is deemed metallic due to the disappearance of the Mott insulating gap and an increase in the density of states at the Fermi level. However, its dynamics were shown to be qualitatively different to the equilibrium metallic state at high temperature, including the existence of a mid-gap resonance [37].

More recently, ultrafast electron diffraction experiments have studied the response of the CDW to photoexcitation [71]. They found that the CDW order was not fully suppressed by the light pulse, indicating that the periodic lattice distortion could not be undone in spite of large changes to the electronic structure. This provided further evidence for the notion of a Mott transition at T_c, but also directly indicated that the photoinduced phase retains the distortions caused by the CDW, even as the Mott gap is melted.

The existence of this new transient photoinduced phase provides an opportunity to study a unique state of TaS_2, in which the electronic correlations have been removed and the gap has melted, and yet the lattice symmetry of the insulator is retained, with only weak structural perturbations. Additionally, understanding the relaxation of this phase back to equilibrium may shed further light on the formation of the commensurate Mott-localised low-temperature phase.

The characterisation of the transient state is best approached via time-resolved optical spectroscopy, which enables the electrodynamics of the system to be probed over a range of energies and at all times through the phase transition, and also allows for a separation of structural and electronic effects. This determination of the optical properties will proceed through two main routes. The first will be through the use of time-resolved terahertz spectroscopy, which provides field-resolved information on the low-frequency dynamics around 1 THz and elucidates information about long-range transport. The second method relies on more conventional pump-probe techniques, measuring reflectance changes. However, in the pump-probe experiments performed in this thesis, the probe can be varied over a broad energy range to provide information on transient changes taking place around the gap energy (100 meV) and up to the visible region (~ 2 eV). Finally, time- and angle-resolved photoemission spectroscopy will be employed to study the single particle response across the Brillouin zone, rather than just at the zone centre, as in earlier experiments.

The description of these techniques and the results obtained in characterising the photoinduced phase will now form the content of the next chapters.

Chapter 3

Aspects of Ultrafast Spectroscopy

3.1 Ultrafast Sources

Rapid growth in the development of ultrafast lasers in the 1990s, aided by the discovery of new lasing materials and new mode-locking techniques, such as Kerr lens mode-locking [72], led to tremendous advances in the field of ultrafast science. Thanks to gains in their reliability and ease of operation, ultrafast lasers have become a ubiquitous tool for a broad number of disciplines within physics, chemistry, and biology.

The majority of ultrafast lasers are based on Ti:sapphire as the lasing medium, typically producing radiation with a central wavelength near 800 nm (1.55 eV). While there is much that can be understood using the bare laser pulse at this wavelength, many features of physical systems occur at energies other than this. As such, it is desirable to be able to tune the laser wavelength continuously over a broad spectrum. This is achievable through nonlinear optics, which has led to the development of numerous tunable femtosecond sources [73].

This chapter will introduce the methods required to generate pulses across a broad frequency range using optical parametric amplifiers. It will also discuss the pump-probe technique in more detail, since it underlies all the experimental methods employed in this thesis. Due to its importance and experimental complications, the generation and application of low-energy terahertz radiation will be left to a separate chapter.

3.2 Optical Parametric Amplifiers

3.2.1 Nonlinear optics

The interaction of intense laser light with matter results in changes to a material's optical properties, leading to a number of different phenomena. This occurs through nonlinear optical processes. An applied electric field E induces a polarisation P in a medium. For weak fields, the polarisation is linearly dependent on the field. However, for the intense fields usually encountered with laser pulses the response becomes nonlinear. In general, the polarisation may be described by a power series in the applied field:

$$P = \chi^{(1)}E + \chi^{(2)}E^2 + \chi^{(3)}E^3 + \dots \; . \tag{3.1}$$

In this expression, $\chi^{(n)}$ is the n^{th} order nonlinear susceptibility [74]. Depending on the laser intensity and optical properties of the nonlinear medium, the relative contributions of higher order susceptibilities become more or less important.

A laser beam has a time-varying electric field of the form

$$E(t) = E_0 e^{-i\omega t} + \text{c.c.} \; . \tag{3.2}$$

The simplest nonlinear interaction occurs when just the second-order susceptibility $\chi^{(2)}$ is non-zero, in which case the nonlinear polarisation from equation (3.1) is

$$P^{(2)}(t) \propto 2E_0E_0^* + E_0^2 e^{-i2\omega t} + \text{c.c.} \; . \tag{3.3}$$

The result of the nonlinear interaction is to generate a zero-frequency field (which does not radiate) and a field at twice the frequency of the laser pulse. This process is known as second-harmonic generation.

However, in general a laser pulse contains more than one frequency, leading to two different important effects. Consider a pulse which contains two frequencies:

$$E(t) = E_1 e^{-i\omega_1 t} + E_2 e^{-i\omega_2 t} + \text{c.c.} \; . \tag{3.4}$$

Using only the $\chi^{(2)}$ term again, the laser induces a nonlinear polarisation of the form

$$\begin{aligned} P^{(2)}(t) \propto \text{constant} &+ E_1^2 e^{-i2\omega_1 t} + E_2^2 e^{-i2\omega_2 t} \\ &+ 2E_1E_2 e^{-i(\omega_1+\omega_2)t} + 2E_1E_2^* e^{-i(\omega_1-\omega_2)t} + \text{c.c.} \; . \end{aligned} \tag{3.5}$$

As before, there is a rectified zero-frequency field and second-harmonic generation from the fundamental frequencies, but now there are also contributions at the sum and difference frequency of the two components. Sum and difference frequency generation form the basis of many of the nonlinear optical techniques employed in this work.

The other remaining process which is integral to the optical parametric amplifier is supercontinuum, or white light, generation. This is a highly nonlinear process, by which the spectrum of a laser is broadened in a transparent nonlinear medium [75, 76]. It arises primarily due to the interplay between self-phase modulation and self-focussing. In these processes, an intense laser pulse creates an intensity-dependent refractive index through the third-order susceptibility. This refractive index varies in time, leading to the creation of frequency sidebands and a broadening of the pulse spectrum. There are further contributions from other nonlinear processes which affect the output, though a complete description is yet to be understood [76].

3.2.2 Optical parametric amplification

The general principle of optical parametric amplification stems from the processes described in section 3.2.1. In an optical parametric amplifier (OPA), a high intensity light pulse with frequency ω_p (the pump beam) entering a nonlinear medium amplifies a lower intensity pulse at ω_s (the signal beam) and generates a third pulse at ω_i (the idler beam). The frequencies are related according to energy conservation by the expression

$$\hbar\omega_p = \hbar\omega_s + \hbar\omega_i, \tag{3.6}$$

where by definition $\omega_i < \omega_s < \omega_p$. For the process to occur efficiently, momentum conservation must also be satisfied. That is,

$$\mathbf{k}_p = \mathbf{k}_s + \mathbf{k}_i, \tag{3.7}$$

where $\mathbf{k}_p$, $\mathbf{k}_s$, and $\mathbf{k}_i$ are the pump, signal, and idler wave vectors, respectively. This is also referred to as the phase matching condition.

The phase matching condition (3.7) can be rewritten in terms of the refractive index n in the nonlinear medium as

$$n_p = \frac{n_i\omega_i + n_s\omega_s}{\omega_p}, \tag{3.8}$$

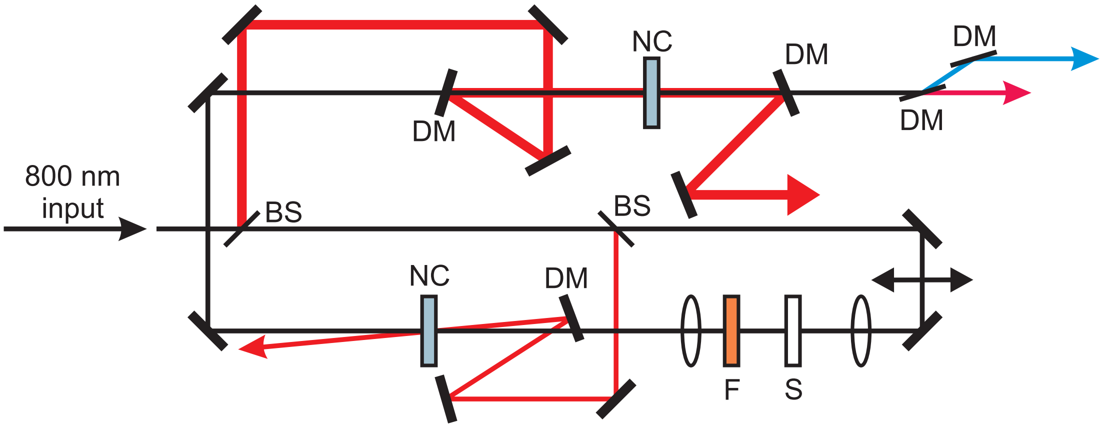

Figure 3.1: Schematic diagram of a near-infrared optical parametric amplifier. Red lines indicate pump beams. BS – beam splitter. S – sapphire. F – filter. DM – dichroic mirror. NC – nonlinear crystal.

since $k = n\omega/c$. In general, different frequencies travel at different speeds in a medium, so the difficulty for an OPA lies in finding a suitable nonlinear medium in which this condition can be satisfied. This can be done using uniaxial crystals, in which the refractive index at a given frequency depends on both the polarisation of the light and the direction of propagation. This dependence of refractive index on polarisation is called birefringence. Phase matching then proceeds by selecting appropriate polarisations of pump and signal beams and correctly orienting the nonlinear crystal. By careful selection of the medium, an OPA can efficiently amplify a broad range of frequencies.

3.2.3 Design of the infrared optical parametric amplifier

The near-infrared (IR) OPA used for the experiments in this thesis was a two-stage TOPAS-C from Light Conversion. Two amplification stages are used in order to minimise effects of group velocity mismatch between pump and signal beams, which would be a concern if a larger crystal were used instead. A schematic layout of the OPA is shown in figure 3.1. The 800 nm output of a Ti:sapphire femtosecond laser serves as the input. A large percentage of the beam is split off for later use in the second stage. Of the remaining light, a small portion is used to generate a white light continuum seed in sapphire. The bulk of the 800 nm light is then filtered out to leave only the broadened spectrum, which serves as the signal beam for the first stage of amplification.

In the first stage, the continuum is mixed non-collinearly with a split-off portion of the 800 nm light in a β-barium borate (BBO) crystal. This crystal is chosen for its efficient phase matching properties over the near-IR region. Dichroic mirrors are used to combine the two beams at a narrow angle before mixing them. The white light continuum is dispersed, meaning different frequency components arrive at different times within the pulse envelope. Furthermore, it is desirable to have relatively narrow bandwidth pulses, to enable better frequency selectivity when driving and studying ultrafast phenomena. To this end, only a portion of the continuum is amplified to produce the required wavelength. To select the correct wavelength for amplification, the relative time delay between the white light and the 800 nm pulse is adjusted using a translation stage, indicated by the double-headed arrow in figure 3.1. The phase matching condition is then met by tuning the angle of the crystal. Non-collinear mixing is chosen to provide easy filtration of the pump and idler beam after amplification.

Next, the amplified signal beam is mixed with the second stage pump beam in another BBO crystal, this time in a collinear arrangement to allow for maximum amplification. After this final amplification stage, the pump, signal, and idler are all co-propagating. The pump is separated out using a dichroic mirror and blocked in a beam dump.

The OPA is capable of producing wavelengths between 1180 and 1620 nm in the signal beam and 1620 and 2680 nm in the idler beam. They leave the OPA collinearly, but can be separated using a chicane of dichroic mirrors, as illustrated in figure 3.1. By judicious choice of these mirrors, the signal or idler can be selected to leave the chicane with maximum power.

Two OPAs were employed for some of the experiments to be described, though the layout of both was as described above. By operating them at different powers, one OPA can be used as a pump source and the other as a probe source. This facilitates not only frequency-resolved probing of a system, but also frequency-resolved pumping, which is useful to examine excitations at different wavelengths. Both OPAs were driven by 60 fs pulses from a 1 kHz Ti:sapphire amplified laser. The pump used 1.4 mJ of this source laser and output a maximum energy of 370 μJ at 1450 nm (combined signal and idler energy), while the probe took 0.3 mJ and produced a peak energy of 100 μJ, also at 1450 nm.

The range of the near-IR OPAs may be extended into the mid-IR through difference frequency generation (DFG), a process described in section 3.2.1, where pulses at frequencies ω_1

and ω_2 are mixed in a nonlinear crystal to produce a third pulse at their difference frequency, $\omega_3 = \omega_1 - \omega_2$ [74]. GaSe is used as the nonlinear medium as it has a large nonlinear susceptibility and its birefringent properties mean that it can be angled tuned to provide phase matching over almost the whole of its transparency window. As such, it is ideally suited to produce light on the microjoule scale down to approximately 22 μm.

The DFG scheme is implemented with only a minor modification to the OPA design of figure 3.1. It requires the removal of the final chicane, which separates the signal and idler, replacing it with the GaSe crystal. This results in the collinear interaction of signal and idler beams to produce the DFG beam. The mid-IR wavelengths can then be separated by a careful selection of filters. The disadvantage of this arrangement is that the filters can substantially reduce the DFG pulse energy, making it suitable only for probing applications. In order to use it as a pump, it is better to use a non-collinear scheme, where spatial filtering of signal and idler does not reduce the mid-IR power.

3.2.4 Determining the wavelength

Characterising the output of the OPA is relatively simple in the near-IR range. Second-harmonic generation produces wavelengths in the visible, which can be easily detected on a commercial spectrometer. This allows the OPA to be easily calibrated over the basic wavelength range. However, the mid-IR region is harder to determine due to a lack of detectors and spectrometers sensitive to these wavelengths.

Therefore, to ascertain the wavelength in the mid-IR, a Michelson interferometer was built, as illustrated in figure 3.2(a). The incoming light is split into two equal parts by a beamsplitter, each of which travels down a separate arm. They are then reflected back and recombined on the other side of the splitter. A pellicle beamsplitter is used to prevent the introduction of dispersion to the pulse. The path length of one of the arms can be adjusted by an amount $\tau = \Delta x/c$, where Δx is the distance the mirror is moved. The beams are then focussed onto a liquid nitrogen cooled HgCdTe detector, which offers sensitivity down to around 21 μm. The fields of the recombined beams interfere to give a net field $E = E_1(t-\tau) + E_2(t)$ and the detector measures the resulting intensity [77].

The intensity recorded depends on the temporal separation of the fields, such that when $\tau = 1/2\omega$, so that the fields are separated by a half-period, there is a minimum in intensity,

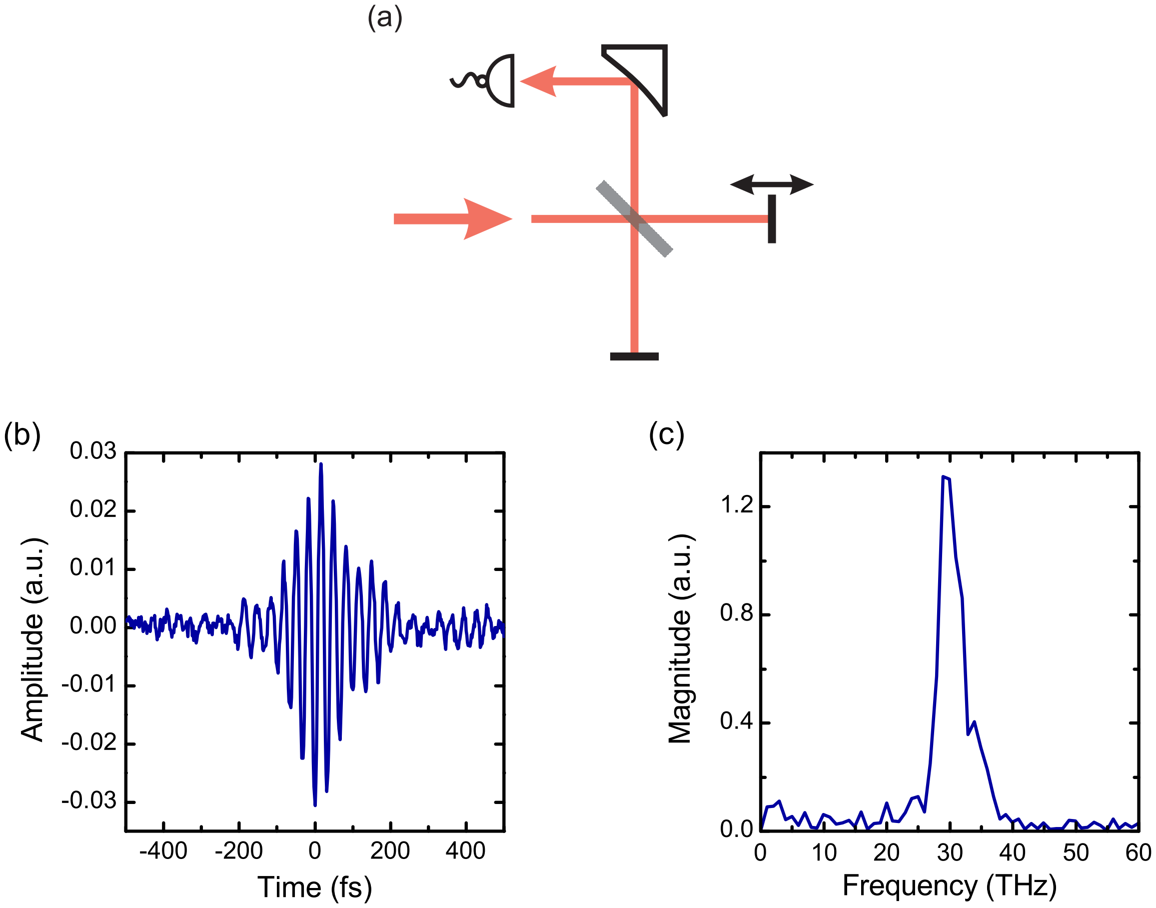

Figure 3.2: Measuring wavelengths. (a) Schematic of a Michelson interferometer. (b) Time domain trace. (c) FFT of time domain measurement.

whilst for $\tau = 1/\omega$ there is a maximum. By varying the time delay τ and recording the intensity at each point, an interferogram is built up which depends on the field of the light, not its intensity. An example interferogram is shown in figure 3.2(b) for a DFG pulse centred at 10 µm. This type of interferogram is called an electric field autocorrelation [77]. Its Fourier transform gives the spectral intensity of the light. The spectrum corresponding to the field autocorrelation of figure 3.2(b) is illustrated in figure 3.2(c).

The mid-IR pulses output by the DFG stage of the OPAs can be measured using the Michelson interferometer to provide spectral information, though the pulse duration cannot be accurately ascertained from this measurement. Intensity cross- or autocorrelations must be performed instead, as will be described below.

3.2.5 Determining the pulse duration

As well as characterising the wavelength of the OPA pulses, it is important to know their duration. As mentioned above, this is done using cross- or autocorrelations of the pulses in a nonlinear crystal. A number of approaches exist for these measurements [77], though only two will be mentioned here.

The first method applies to near-IR wavelengths. For wavelengths down to around 2 µm, the pulses can interact in BBO and generate a third pulse at their sum frequency, as outlined in section 3.2.1. This sum frequency is in the visible region, so can be measured using a standard silicon photodiode. The intensity of the sum-frequency pulse depends on the intensities of the input pulses according to:

$$I_{\mathrm{SF}}(t) = \int_{-\infty}^{\infty} I_1(t) I_2(t-\tau) d\tau. \tag{3.9}$$

By varying the time delay between the two pulses, the intensity profile of their cross-correlation (or autocorrelation, if two copies of the same pulse are used) is obtained. This may then be used to calculate the duration of the individual pulses. This process is illustrated schematically in figure 3.3(a), while figure 3.3(b) shows an autocorrelation profile for 1.3 µm pulses obtained from one of the OPAs. The autocorrelation has a FWHM of 287 fs, meaning the single pulse duration is 203 fs after deconvolution.

The mid-IR pulse durations were determined by cross-correlation between them and the 1.3 µm near-IR pulses. Due to their low intensity and the nonlinear properties of BBO, a different scheme needs to be employed to that for the near-IR pulses. Instead of using sum frequency generation in BBO, the pulses were mixed in ZnTe, where the Kerr effect was used. In this case, the field of the mid-IR light induces a birefringence in the ZnTe crystal, which causes a rotation of the polarisation of the co-propagating pulse. By measuring the degree of polarisation rotation as the two pulses are delayed relative to one another, their cross-correlation profile can be mapped out, similar to that found for the near-IR case. This technique closely resembles the electro-optic sampling method of terahertz spectroscopy, which will be described in detail in chapter 4. A schematic of the mid-IR/near-IR cross-correlation apparatus is shown in figure 3.3(c). A cross-correlation intensity profile obtained in this manner between a 1.3 µm pulse and a 14.8 µm pulse is shown in figure 3.3(d). Using the 1.3 µm pulse duration calculated above, the 14.8 µm pulse is found to have a duration of

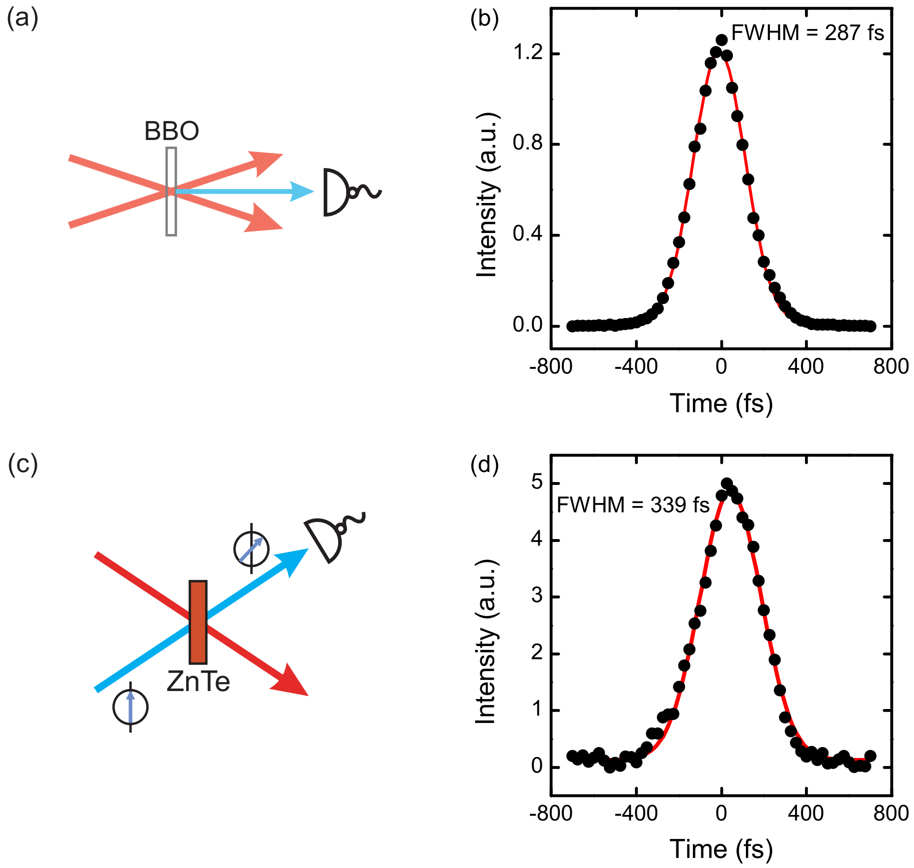

Figure 3.3: Determining pulse durations. (a) Schematic representation of the intensity autocorrelation scheme used to measure near-IR pulse durations. (b) Autocorrelation of a 1.3 μm pulse using the setup illustrated in (a). (c) Schematic layout of the cross-correlation scheme used to measure mid-IR pulse durations. Arrows in circles represent the polarisation of the near-IR light field. (d) Cross-correlation of a 1.3 μm pulse with a 14.8 μm pulse using the setup sketched in (c).

approximately 270 fs.

The pulse durations determined using the methods described in this section are all measured in situ for the experiments they relate to. This means that any temporal effects caused by non-collinear experimental geometries are taken into account. Furthermore, the use of thin nonlinear crystals in the measurement process ensures that dispersion effects are kept to a minimum. As such, the pulse durations measured are representative of their interaction time at the sample.

3.3 Pump-Probe Spectroscopy

Femtosecond pulses are ideally suited to the study of ultrafast processes in condensed matter physics, as well as a variety of other systems. They are regularly employed in pump-probe experiments, which have arisen as the predominant technique to study dynamics on the ultrafast timescale. In these experiments, an intense ‘pump’ pulse is used to excite the system into a non-equilibrium state, driving dynamics in various degrees of freedom as it does so. The system then relaxes back to its ground state, usually via some intermediate meta-stable state. A second weaker ‘probe’ pulse is then used to interrogate the response of the system as it undergoes this evolution. By changing the arrival time of the probe pulse relative to the pump and measuring the resulting changes to the probe, a series of snapshots of the system can be acquired, which allow for a complete mapping of the properties of the system in time.

The pump-probe time delay is controlled by varying the distance one of the two beams travels, usually using a pair of mirrors on a mechanical delay stage. Then a relative time delay of $\tau = 50\,\mathrm{fs}$, for instance, can be introduced by moving the delay stage by $\Delta x = c\tau/2 = 7.5\,\mu\mathrm{m}$, where the factor of two accounts for the retroreflection of the light. With the availability of high precision stages, the limiting factor for the temporal resolution of an experiment becomes the pulse durations themselves, rather than the mechanical precision of the stage.

The pump-probe spectroscopy technique is furthered by changing not just the pump-probe time delay but also the photon energy of the interrogation or excitation pulses. Changing the probe frequency allows for the investigation of the response at different energy scales, and can provide information on different processes and phenomena within the system. Changing the pump frequency is useful to explore the importance of photon energy in driving specific processes, such as gap collapse in insulators or intra-band excitations in charge-transfer materials.

In general, optical pump-probe experiments are carried out by measuring the intensity of the probe pulse after it is reflected or transmitted by the sample under scrutiny. Changes in the reflectance or transmittance are recorded, which can then be interpreted to give information on the changes to the optical properties. Transmission experiments are generally easier to interpret, since they give direct information on the absorption properties of the material. Also, by using thin samples, problems concerning the mismatch of pump and probe penetration depths may be avoided, if the samples are thinner than the pump skin depth. However, transmission experiments are frequently not possible due to the difficulties in preparing thin samples or because of the opacity of the material of interest. Therefore, reflection geometry experiments must often be employed.

The experiments in this thesis are all based on reflection measurements. The probe pulse is reflected from the photoexcited surface and measured by a detector downstream. The nature of detection depends on the frequency of the probe light: in the case of visible to mid-IR frequencies, the intensity of the light pulse is recorded by a diode, resulting in measurements of the reflectance; in THz reflection spectroscopy, the electric field of the probe pulse is directly recorded after reflection, thereby measuring changes to the complex reflectivity. In the former case, the selection of appropriate diodes is important for the frequency range under investigation, since the sensitivity of diode materials varies across the spectrum. The detection scheme in the latter case will be discussed in detail in chapter 4.

The reflectivity has a complicated dependence on the optical properties of the material and the incident angles involved. Often, it is also necessary to consider the problem of pump-probe penetration depth mismatch mentioned above. These issues mean that a straightforward analysis of the signals acquired is not always possible, and different approaches and approximations need to be made. This is especially true in the case of terahertz-based pump-probe experiments, which measure electric fields rather than intensities, and will be discussed in chapter 4. An analysis of these concerns in optical measurements will be discussed in chapter 5.

3.4 Anatomy of Transient Reflectivity Measurements

3.4.1 Timescales

The pump pulse excites the system in a non-trivial way, leading to sometimes dramatic changes in the optical properties. As the system relaxes, energy is redistributed through different processes on different timescales. Most commonly, the energy from the pump is initially deposited in the electronic subsystem. This excites electrons into new states and leads to a prompt change in the reflectivity; for example, they may be promoted across the band gap in an insulator or semiconductor. The subsequent redistribution of energy among different degrees of freedom in the system then leads to further changes in the reflectivity. The timescales for changes in the signal then provide information on these processes.

The evolution of the reflectivity often undergoes a series of events as follows [78, 79]. Immediately after photoexcitation, the electron distribution is non-thermal and it thermalises via electron-electron scattering on a timescale $\tau_{e\text{-}e}$ of typically just a few femtoseconds to hundreds of femtoseconds [80]. Electrons then begin to thermalise with the lattice through electron-phonon scattering. This occurs on a timescale $\tau_{e\text{-}ph}$ which is typically on the order of a hundred femtoseconds to a few picoseconds. Measurements of this longer relaxation rate can reveal information on the electron-phonon coupling constant [81].

Generally speaking, these processes lead to close to exponential decay of the reflectivity back towards the equilibrium value. The overall generic form of a pump-probe reflectance trace then is zero signal before the arrival of the pump, a prompt change on excitation, and approximately exponential decay, with one or more timescales, back towards zero.

3.4.2 Coherent phonons

The incoherent processes described in section 3.4.1 are not the only ones that can affect the transient optical properties of the solid. It is also possible to observe large oscillatory changes in the reflectance or transmittance whose frequency corresponds to Raman-active phonon modes. These oscillations indicate that it is possible to excite lattice vibrations in the crystal; indeed, it is a general phenomenon which occurs whenever an intense laser pulse interacts with a solid.

In a crystal lattice, phonons exist with a density described by the Bose-Einstein distribution $n(\omega) = \left[\exp(\frac{\hbar\omega}{k_B T}) - 1\right]^{-1}$ [82]. Their phases are random, so their motion cancels out and there is no macroscopic influence on the polarisation. However, the impact of an ultrafast laser pulse can cause the phonons to oscillate in phase with one another, inducing time-dependent macroscopic changes in the optical properties, which translate into changes in the reflectivity or transmission measured by a probe pulse [83, 84]. Crucially, the excitation pulse must have a duration less than the phonon period.

Coherent phonon generation in absorptive materials has been explained via the displacive excitation of coherent phonons (DECP) mechanism [85]. The phonon equilibrium displacements are a function of the free energy of the system, and so are dependent on temperature. The arrival of a pump pulse creates a quasi-equilibrium state, where the electron temperature, and hence the free energy, has been modified. This creates a new quasi-equilibrium position for the phonon, which now finds itself in an excited state. The phonon experiences a restoring force due to this change, and begins to oscillate as it returns back to its ground state.

The quasi-equilibrium position $Q_0(t)$ is dependent on the electron temperature and also the density of electrons promoted to excited bands, described by $n(t)$. In DECP this dependence is taken to be linear:

$$Q_0(t) = \kappa n(t), \tag{3.10}$$

where κ is a constant of proportionality. The electron density in the excited bands can be described by the rate equation

$$\dot{n}(t) = \rho P(t) - \beta n(t), \tag{3.11}$$

where the first term gives the excitation rate of the pump pulse and the second term is the rate of electron transfer back to the equilibrium state.

The oscillation of the phonon coordinate $Q(t)$ in this linear regime is given by

$$\ddot{Q}(t) = -\omega_0^2 \left(Q(t) - Q_0(t)\right) - 2\gamma\dot{Q}(t), \tag{3.12}$$

where ω_0 is the equilibrium frequency of the phonon mode and γ is the damping constant of the mode. A solution to equation (3.11) is $n(t) = \rho\varepsilon_{\text{pump}} \int_0^\infty g(t-\tau)e^{-\beta\tau}d\tau$, where $\varepsilon_{\text{pump}}$ is the energy density of the pump pulse and $g(t)$ is the normalised pump pulse shape. This produces a result for the phonon coordinate of the form

$$Q(t) \propto \int_0^\infty g(t-\tau)\left\{e^{-\beta\tau} - e^{-\gamma\tau}\left(\cos(\Omega\tau) - \frac{\beta'}{\Omega}\sin(\Omega\tau)\right)\right\}d\tau, \tag{3.13}$$

with $\Omega^2 = \omega_0^2 + \gamma^2$ and $\beta' = \beta - \gamma$. In the limit of impulsive excitation and weak damping, such that $g(t)$ tends to a δ function and $\omega_0 \gg \gamma$, equation (3.13) shows that the motion of the phonon coordinate is oscillatory and decays exponentially in time. Furthermore, in the limit of the phonon lifetime being longer than the phonon period ($\beta \ll \omega_0$), the cosine term dominates. Hence phonons generated by DECP are expected to oscillate as $\cos(\omega_0 \tau)$. This modulation directly alters the reflectivity, producing reflectance changes along the lines of

$$\frac{\Delta R(t)}{R} \propto e^{-\beta\tau} + e^{-\gamma\tau}\left(\cos(\Omega\tau) - \frac{\beta'}{\Omega}\sin(\Omega\tau)\right). \tag{3.14}$$

It was originally expected that the changes initiated by DECP were of A-type symmetry, since such modes do not alter the symmetry of the system [78]. It was later shown that other Raman-active modes of E as well as A-type could be excited [86]. Observations of coherent phonons can provide important information on the coupling between the lattice and other degrees of freedom in strongly correlated electron materials [24, 87, 88]. Their presence will help determine the role of the CDW distortion in the photoinduced phase of $\mathrm{TaS_2}$.

3.5 Summary

This chapter has introduced some key concepts in ultrafast spectroscopy. The use of optical parametric amplifiers allows for frequency-resolved studies of ultrafast processes. Determining the frequency of the light they generate is an important part of such experiments and can be achieved using a Michelson interferometer.

Pump-probe experiments use time-delayed pulses to excite a system and monitor its evolution. A number of different physical phenomena can manifest themselves through the time-domain traces obtained in this way. Principally, the different timescales elicit information on the relaxation pathways in the system. A further effect of relevance to this thesis is coherent phonon generation, which takes place via the displacive excitation mechanism.

All of these concepts will be important when describing the experimental work undertaken in later chapters of this thesis. Before discussing this, the topic of THz time-domain spectroscopy, mentioned briefly in section 3.3, will be expanded upon.

Chapter 4

Terahertz Time-Domain Spectroscopy

4.1 The Terahertz Domain

The terahertz (THz) region of the electromagnetic spectrum, defined as extending from 0.1 to 30 THz, is of great importance to the study of condensed matter systems, as it is in this region that many of the phenomena influencing the electronic properties of materials are to be found. Bound states such as excitons and Cooper pairs have energies in the THz range, as do phonons, and information may also be gained on scattering rates in semiconductors and superconductors and confinement in low-dimensional solids, all by investigating this region. However, the availability of suitable sources and detectors has hindered experimental progress in the past. Traditionally, forays into the far-infrared region relied on microwave sources and Fourier transform infrared (FTIR) spectrometers. Microwave sources are limited to a range below about 0.1 THz, making them ineffective for higher energy studies, and FTIR methods lack brightness in the THz range. Additionally, the optical constants, such as the dielectric function or complex conductivity, cannot be obtained directly but must be derived using Kramers-Kronig relations. Their reliance on extrapolations outside of the measured range makes them susceptible to phase errors, with different extrapolations providing slightly different results.

In the last two or three decades, optical technology has developed enormously, and the THz region has opened up through the advent of THz time-domain spectroscopy (THz-TDS). This technique has overcome the earlier problems of infrared spectroscopy by providing sources with broad bandwidth in an inaccessible spectral region and by enabling direct measurements of the dielectric function of materials without resorting to Kramers-Kronig methods. The principle is founded on the generation of THz transient waves using ultrafast laser pulses, which are then detected using optical gating. This allows for a direct measurement of the electric field of the pulse itself, which is used to reconstruct the real and imaginary parts of the optical constants without extrapolation or approximation. Gated detection also allows for highly sensitive frequency measurements. Furthermore, the pulsed nature of the THz source makes it ideal for use in pump-probe experiments, with THz transients having durations of typically 1 ps or less.

4.2 Generation and Detection

The two most common schemes for generating and detecting THz radiation are the photoconductive antenna [89–91] and optical rectification and free-space electro-optic sampling in nonlinear electro-optic media [92–94]. The development of THz-TDS began with photoconductive antennae, though their usage has some limitations. Principally, they are extremely sensitive to alignment, such that it is difficult to get accurate measurements of the THz fields [95] and they also have bandwidth limitations due to the natural timescale of carrier dynamics in the antenna [92, 95]. Free-space electro-optic sampling (EOS) is capable of measuring much higher frequencies [94, 96] and with less alignment sensitivity than the antenna approach, leading its more widespread use today. As such, it will be the focus in all that follows.

The generation of THz transients takes place via optical rectification of a femtosecond laser pulse in a nonlinear electro-optic medium. It may be understood in terms of a phase matched $\chi^{(2)}$ process involving different frequency components within the same pulse [97]. An incident laser pulse induces a nonlinear time-varying polarisation in the medium through difference frequency mixing of its Fourier components. This polarisation acts as a source of electromagnetic radiation with a spectrum extending from 0 up to several THz, if the driving pulse has sufficient bandwidth [96].

EOS essentially acts as the inverse of this process, mixing the THz pulse with an optical laser pulse in a nonlinear medium through the Pockels effect. In the Pockels effect, a nonlinear

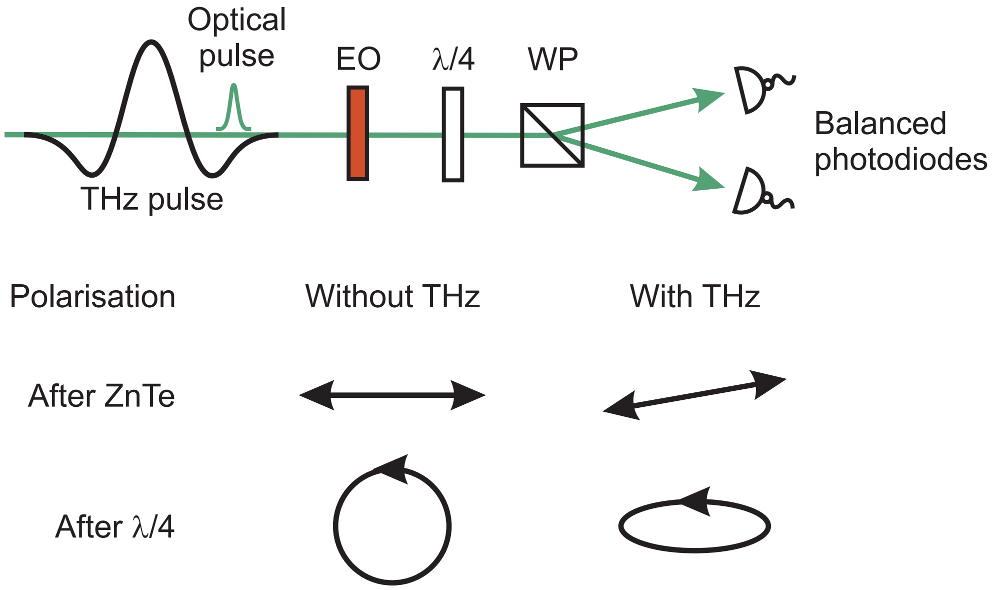

Figure 4.1: Schematic layout for free-space electro-optic sampling. EO – electro-optic medium. $\lambda/4$ – quarter-wave plate. WP – Wollaston prism. The effect of the THz field and electro-optic sampling optics on the polarisation of the detection pulse are illustrated beneath.

polarisation is induced in an electro-optic medium according to [74]

$$P_i(\omega) = 2\sum_{jk} \chi^{(2)}_{ijk}(\omega = \omega + 0)E_j(\omega)E_k(0). \tag{4.1}$$

Thus a static field induces a birefringence in the medium which is proportional to the applied field amplitude, and by measuring the degree of birefringence the applied field strength may be determined; this is the principle of free-space EOS.

The THz field and the optical pulse co-propagate through the medium; assuming the THz phase velocity and optical group velocity match, a short optical pulse feels a constant electric field due to the instantaneous THz field and its polarisation becomes rotated due to the field-induced birefringence. The degree of rotation is proportional to the THz field at the point the two pulses overlap, so a measurement of the polarisation rotation gives a measurement of the THz electric field. This is achieved by propagating the optical pulse through a quarter-wave ($\lambda/4$) plate and then a Wollaston prism. The $\lambda/4$ plate is aligned such that in the absence of the THz field, the linearly polarised sampling pulse becomes circularly polarised. The Wollaston prism then splits the pulse into two orthogonal components, which are detected by two photodiodes. The orthogonal components are equal in size so the difference between

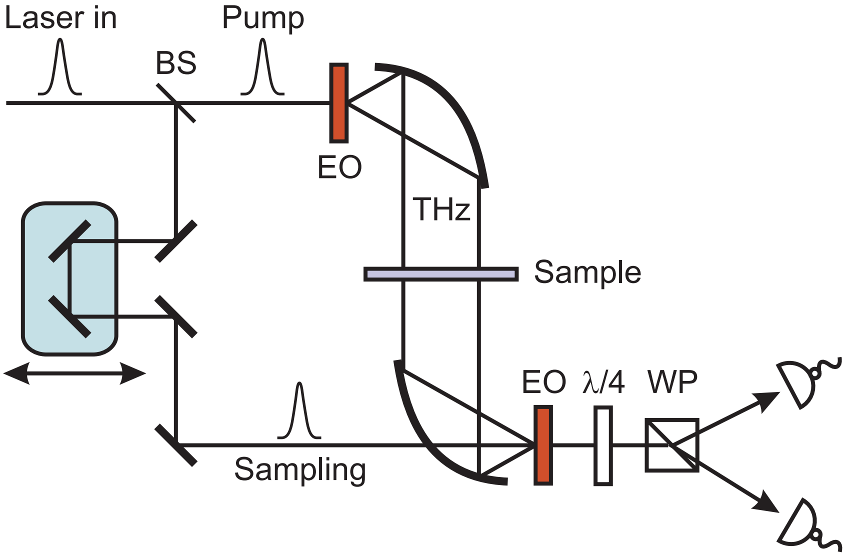

Figure 4.2: Schematic layout for a THz time-domain spectrometer. EO – electro-optic medium. $\lambda/4$ – quarter-wave plate. WP – Wollaston prism. BS – beam splitter.

the detectors is zero. When the THz field is present, the optical sampling pulse becomes slightly rotated and the polarisation is elliptical after the $\lambda/4$ plate. Now the two detectors are unbalanced and an intensity difference is measured between them which is proportional to the ellipticity of the sampling beam. Thus the intensity difference is a direct measurement of the instantaneous THz electric field. The whole process is shown schematically in figure 4.1. By scanning the relative delay of the optical and THz pulses and measuring the ensuing intensity differences, the electric field of the THz pulse may be mapped out in time.

A THz time-domain spectrometer based on optical rectification and free-space EOS was built as illustrated in figure 4.2. The electro-optically active medium used is $\langle 110 \rangle$ cut ZnTe, since it has good phase-matching properties between pulses at 800 nm and 0 to 5 THz. It also has a relatively large electro-optic coefficient, resulting in relatively large THz transients and correspondingly large EOS measurements. Its first TO phonon mode is at 5.3 THz, which restricts its detectable bandwidth to about 5 THz. For higher frequency investigations, crystals such as GaP, with its higher TO phonon frequency [94], or GaSe, which can be angle tuned to provide broad phase matching [98, 99], should be used.

The driving laser was a Ti:sapphire amplified laser centred at 800 nm with a pulse duration of approximately 50 fs. Typical THz transients obtained with this system are shown in figure 4.3. The top left panel shows a trace obtained with the spectrometer in air, while the

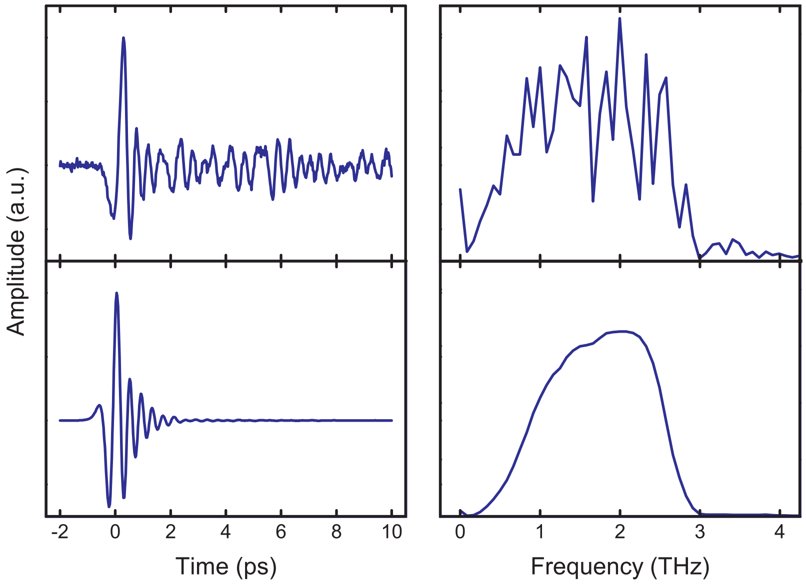

Figure 4.3: THz time-domain traces and associated spectra. Top: THz trace obtained in air. Bottom: THz trace under vacuum.

top right panel gives its Fourier transform spectrum. The ringing at long times is caused by absorption and re-radiation from molecules in air, which have resonances in the THz region. The result is a confusing time-domain trace with many absorption lines in its spectrum. This complicates any spectral analysis since the contribution from the atmosphere must be taken into account. It also reduces the overall amplitude of the THz electric field and introduces noise. To clean up the spectrum, the whole apparatus was placed inside a vacuum chamber, excluding the $\lambda/4$ plate, Wollaston prism, and balanced detectors. The resulting THz transient and its spectrum can be seen in the bottom panels of figure 4.3. The ringing after the THz pulse is removed, leaving only the rectified THz field, and the spectrum is significantly cleaner. The vacuum chamber also allows for cryogenically-cooled samples to be used without worrying about windows and their associated losses, by mounting the cryostat cold finger within the spectrometer chamber. This is important due to the lack of windows with suitable transparency in the THz region and becomes even more important when dealing with time-resolved pump-probe studies, when it would become necessary to find window materials which are transparent in diverse regions of the spectrum. This will be covered in more detail later.

4.3 Determining the Optical Properties

The power of THz-TDS is its ability to record both amplitude *and* phase information by direct measurement of the electric field. This provides amplitude and phase information on the transmission or reflection coefficients of the sample of interest, which in turn yields both real and imaginary parts of the complex dielectric function, within the spectrum of the THz pulse. As discussed above, this is a major advantage over FTIR methods, which only provide power spectra and rely on Kramers-Kronig methods to determine the optical constants.

This section will now outline the basic procedure for obtaining the complex dielectric constant and complex optical conductivity of a medium from measurements of the THz transient. Since the samples of interest in this thesis are all opaque, all experiments are carried out using reflection measurements only; the opacity and sample thickness are such that there is no detectable signal in transmission. Therefore, only the reflectivity will be considered in all that follows, though the analysis may also be applied to the transmission coefficients to find the appropriate relations in that case.

4.3.1 The complex optical constants

The optical properties of a medium are described by the dielectric constant $\tilde{\varepsilon}$, the optical conductivity $\tilde{\sigma}$, and the complex refractive index $\tilde{n}$, all of which are, in general, complex quantities:

$$\tilde{\varepsilon}(\omega) = \varepsilon_1(\omega) + i\varepsilon_2(\omega), \tag{4.2}$$

$$\tilde{\sigma}(\omega) = \sigma_1(\omega) + i\sigma_2(\omega), \tag{4.3}$$

$$\tilde{n}(\omega) = n(\omega) + i\kappa(\omega), \tag{4.4}$$

where n is the refractive index and κ is the absorption coefficient [100]. The complex refractive index is related to the complex dielectric constant by [101]

$$\tilde{n}^2(\omega) = \tilde{\varepsilon}(\omega). \tag{4.5}$$

The general relation between the dielectric constant and complex conductivity may be shown to be [101]

$$\tilde{\varepsilon}(\omega) = \varepsilon(\omega) + i\frac{\sigma(\omega)}{\omega\varepsilon_0}, \tag{4.6}$$

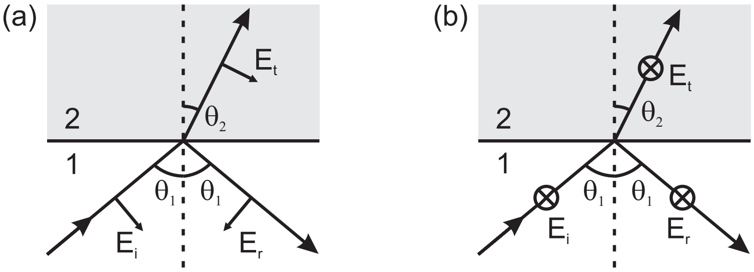

Figure 4.4: Reflection and refraction of electromagnetic waves at the interface between two media for **E** parallel to (a) and perpendicular to (b) the plane of incidence.

where ε_0 is the permittivity of free space, $\varepsilon(\omega)$ describes the motion of bound charges, and $\sigma(\omega)$ describes that of free charges, in the limit of a very low frequency or DC field. However, at higher frequencies, especially optical frequencies, the response of free and bound charges to the rapidly varying field changes dramatically from the low frequency case, and the distinction between bound and free charges becomes one of convention [82]. As such, it is possible to redefine $\varepsilon(\omega)$ using an arbitrary function of frequency, so long as $\sigma(\omega)$ is correspondingly redefined, satisfying the relation (4.6). The relation between the dielectric constant and complex conductivity is redefined here to place the response of all electrons into the conductivity term [102]:

$$\tilde{\varepsilon}(\omega) = 1 + i\frac{\tilde{\sigma}(\omega)}{\omega\varepsilon_0} \ . \tag{4.7}$$

This definition holds well so long as the conductivity remains greater than unity. It also allows for clarity in converting back and forth between $\tilde{\varepsilon}$ and $\tilde{\sigma}$, since the real and imaginary parts of $\tilde{\sigma}$ and $\tilde{\varepsilon}$ may now be expressed in terms of each other as:

$$\sigma_1 = \omega\varepsilon_0\varepsilon_2, \tag{4.8a}$$

$$\sigma_2 = \omega\varepsilon_0(1 - \varepsilon_1). \tag{4.8b}$$

Thus with relation (4.7) it can be seen that the real part of the conductivity connects to the imaginary part of the dielectric constant, while the imaginary part of the conductivity relates to the real part of the dielectric constant.

4.3.2 Fresnel's relations

The optical constants as outlined in the previous section determine the response of a medium to an external electromagnetic wave. The wave will be partially transmitted and partially reflected, with different frequencies of light being affected by different amounts. Figure 4.4 shows a wave, E_i, travelling from medium 1 into medium 2 at an angle θ_1 to the surface normal. A fraction E_r is reflected at an angle θ_1 and a fraction E_t is transmitted at an angle θ_2, both relative to the surface normal. In figure 4.4(a) E_i is parallel to the plane of incidence, denoting p-polarisation, whilst in figure 4.4(b) E_i is perpendicular to the plane of incidence, denoting s-polarisation. The ratio of reflected to incident electric fields is the reflection coefficient, $r = E_r/E_i$. Satisfying the boundary conditions for electric and magnetic fields at an interface yields the Fresnel relations [103]:

$$r_s = \frac{\tilde{n}_1 \cos\theta_1 - \tilde{n}_2 \cos\theta_2}{\tilde{n}_1 \cos\theta_1 + \tilde{n}_2 \cos\theta_2}, \tag{4.9}$$

$$r_p = \frac{\tilde{n}_2 \cos\theta_1 - \tilde{n}_1 \cos\theta_2}{\tilde{n}_2 \cos\theta_1 + \tilde{n}_1 \cos\theta_2}, \tag{4.10}$$

which describe the reflection coefficient r in terms of the complex refractive indices $\tilde{n}_1$, $\tilde{n}_2$ and angles θ_1, θ_2. These relations are crucial in analysing the THz-TDS data, where the objective is to convert the fields E_i, E_r into the refractive index $\tilde{n}$, or the conductivity $\tilde{\sigma}$.

4.3.3 Analysis of THz-TDS measurements

Having established the definitions of the optical constants and their relations to one another, it is necessary to see how to recover them from measurements of the THz transients. The experimental procedure of THz-TDS involves the measurement of electric fields reflected from the samples under investigation. The Fresnel relations (4.9)–(4.10) suggest that the refractive index can be obtained from the measured fields, and then the expressions in section 4.3.1 can be used to convert that into a dielectric constant or complex conductivity. However, the reflection coefficient depends on the incident electric field, which is generally not known in a reflection experiment. It is also insufficient to simply remove the sample and measure the freely propagating THz field, as this does not preserve any phase differences which arise between reflected and incident pulses. These differences carry information about the complex constants and so it is crucial to preserve them. To overcome this problem, a THz-TDS reflection experiment requires a measurement of the THz field reflected from the sample and from a reference reflector whose reflection coefficient is known. Since the incident field is common to both scenarios, it disappears in a ratio of the two reflectivities, and the reflectivity of the sample can be found from

$$r_{\text{sample}}(\omega) = \frac{\int_{-\infty}^{\infty} E_{\text{sample}}(t)e^{i\omega t}dt}{\int_{-\infty}^{\infty} E_{\text{ref}}(t)e^{i\omega t}dt}\, r_{\text{ref}}(\omega), \tag{4.11}$$

where $E(t)$ refers to the electric field measured in the time domain [102]. Expressing this in a slightly clearer way, the complex reflectivity of the sample may given by

$$r(\omega) = \frac{\widetilde{E}(\omega)}{\widetilde{E}_0(\omega)}\, r_0(\omega), \tag{4.12}$$

where now $r(\omega)$ and $\widetilde{E}(\omega)$ refer to the reflectivity and field from the sample, $r_0(\omega)$ and $\widetilde{E}_0(\omega)$ refer to the reflectivity and field from the reference reflector, and $\widetilde{E}(\omega)$, $\widetilde{E}_0(\omega)$ are the Fourier transforms of $E(t)$, $E_0(t)$.

Now, $E(t)$ and $E_0(t)$ are measured directly using electro-optic sampling, $\widetilde{E}(\omega)$ and $\widetilde{E}_0(\omega)$ are calculated from them, and $r_0(\omega)$ is already known, so $r(\omega)$ can now be calculated using equation (4.12).

The Fresnel relation for s-polarisation given by equation (4.9) describes the reflection coefficient in terms of the complex refractive index of media 1 and 2. Henceforth, a subscript 2 will denote the sample whilst a subscript 1 refers to the incident medium (normally air or vacuum). Equation (4.9) can be inverted to give an expression for the sample refractive index n_2 in terms of the sample reflectivity r (calculated from the THz transients) and the incident medium properties:

$$\tilde{n}_2 \cos\theta_2 = \left(\frac{1-r}{1+r}\right) \tilde{n}_1 \cos\theta_1. \tag{4.13}$$

This can be converted into a dielectric constant using equation (4.5):

$$\tilde{\varepsilon}_2 \cos^2\theta_2 = \tilde{n}_1^2 \cos^2\theta_1 \left(\frac{1-r}{1+r}\right)^2. \tag{4.14}$$

The only concern now is the unknown angle θ_2. It can be removed entirely without assumption using Snell's Law [101] and equation (4.5), to leave the following expression for the dielectric constant in the medium:

$$\tilde{\varepsilon}_2(\omega) = \tilde{n}_1^2 \sin^2\theta_1 + \tilde{n}_1^2 \cos^2\theta_1 \left(\frac{1-r}{1+r}\right)^2. \tag{4.15}$$

It is assumed hereafter that medium 1 is vacuum, so that $\tilde{n}_1 = 1$. The subscript 2 may now be dropped since it is clear that only the sample is being discussed. The subscript 1 on θ_1

may also be dropped assuming that θ now only refers to the angle of incidence. Finally, the dielectric constant of the sample is given by

$$\tilde{\varepsilon}(\omega) = \sin^2\theta + \cos^2\theta \left(\frac{1-r}{1+r}\right)^2, \tag{4.16}$$

and the complex conductivity is given by

$$\tilde{\sigma}(\omega) = i\omega\varepsilon_0 \cos^2\theta \left(1 - \left(\frac{1-r}{1+r}\right)^2\right), \tag{4.17}$$

where equation (4.7) has been used to convert $\tilde{\varepsilon}(\omega)$ to $\tilde{\sigma}(\omega)$. It should be remembered that $r = r(\omega)$ always refers to s-polarised THz radiation.

4.3.4 The phase problem

This section has outlined the procedure for determining the optical constants of a material using measurements of reflected THz transients. The technique has had some success [104–107], though difficulties with phase shifts when changing between sample and reference [106, 107] have meant that it is not as widely applied as transmission THz-TDS, where such problems can be more easily countered.

The phase problem arises due to uncertainty in the position of the sample relative to the reference reflector [106–108]. For a misalignment of the sample relative to the reference of size Δx, a phase shift $\frac{2\Delta x\omega}{c}$ is introduced into the complex electric field. As such, the measured field is $\widetilde{E}_{\text{meas.}}(\omega) = \widetilde{E}(\omega)e^{-i\frac{2\Delta x\omega}{c}}$, where $\widetilde{E}(\omega)$ represents the complex field when the sample is in the correct position. This feeds into the complex reflectivity of equation (4.12) and can lead to errors in the determined optical constants.

It is possible to account for this phase shift numerically by applying a correction to equation (4.12) to counter the misalignment phase [105, 108]. This correction takes the form of an opposing phase shift $-\frac{2\Delta x\omega}{c}$. Since Δx may not be known, the phase must be iteratively adjusted to retrieve the correct optical constants. In general this may require some foreknowledge of the sample properties. In the case of $\mathrm{TaS_2}$ discussed in this thesis, existing FTIR measurements taken from reference [60] were used as a comparison to find the necessary phase shift and extract the optical constants.

It should be noted that determining the precise details of the static optical constants are not the goal of this thesis; instead, it is the time-dependent changes that are of interest.

To this end, it is sufficient to obtain a measurement of the optical constants in the ground state which recreates the salient features already unearthed by other methods. For the time-dependent properties, there is no issue of phase shifts due to sample movement, since the transient field changes $\Delta\widetilde{E}(\omega)$ are referenced to the unperturbed field $\widetilde{E}(\omega)$; by alternating between the two measurements there is no need for the sample to move. Hence the phase problem is only a concern when deriving the static properties.

4.4 Time-Resolved Terahertz Time-Domain Spectroscopy

While THz-TDS offers enormous gains over traditional IR spectroscopy techniques, its ultrafast pulsed nature offers access to a whole new field of time-resolved THz spectroscopy (TRTS). Combining the THz generation and detection schemes with an additional pump pulse enables both the frequency and temporal responses of a material to photoexcitation to be determined. Figure 4.5 demonstrates a typical setup for such an experiment using transmission geometry. By appropriate use of delay lines, the pump-induced changes to the optical constants may be retrieved as a function of time. The field of TRTS has had great success in understanding the dynamics of semiconductors [15, 104, 105, 107, 109, 110], Mott insulators [111], and superconductors [112–114] in response to an optical pump. Using high intensity THz generation schemes, it has also been possible to perform THz-pump–THz-probe measurements [115–117].

4.4.1 Acquisition complications

As intimated above, the delay lines used in TRTS are important as they allow for the acquisition of various types of pump-probe trace. Figure 4.6(a) shows a schematic of the three delay lines used in a TRTS experiment: line 1 is the pump beam, line 2 is the THz transient beam, and line 3 is the THz sampling beam. The most useful information is extracted by obtaining a series of THz scans at different pump-probe delays in a two-dimensional (2D) dataset [15]. It is possible to achieve this by performing a series of one-dimensional (1D) scans and putting them together to form a full dataset. This is done by acquiring 1D probe scans and then 1D pump scans. A probe scan fixes the pump line (1) relative to the THz line (2), thereby determining the pump-probe delay, then scans the THz field with the sampling beam (3). In this

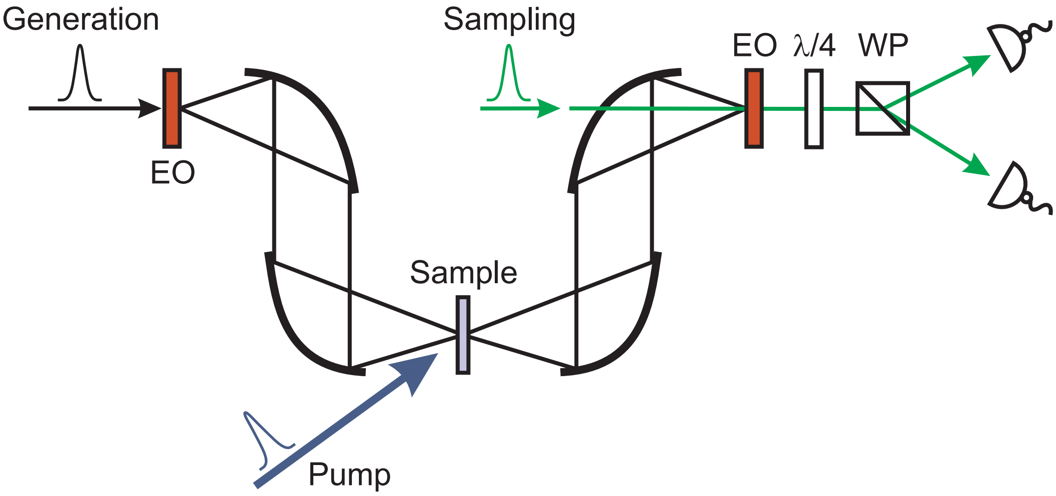

Figure 4.5: Schematic setup for a time resolved THz time-domain spectrometer operating in transmission. EO – electro-optic medium. $\lambda/4$ – quarter-wave plate. WP – Wollaston prism.

manner, changes to the THz field after photoexcitation are recorded; a typical 1D probe scan can be seen in figure 4.6(b). A pump scan fixes the sampling beam (3) at a point in the THz field, usually the peak, and scans them both relative to the pump (1). This then describes the average THz response to photoexcitation and provides no real frequency information. An example of a 1D pump scan is shown in figure 4.6(c). One dimensional scans cannot provide the full temporal and frequency response, which is why they must be combined to provide the full dynamics [15].

There are two problems with the collection of data in TRTS which need to be addressed. The first occurs at early times, as the excitation pulse arrives at the sample. Since the THz pulse duration is typically longer than the pump pulse, only parts of the THz pulse arriving after the pump will be affected by it. Therefore, different parts of the pulse will experience different optical constants in the sample and the 1D probe scans will contain mixed information on the temporal behaviour of the frequency components. This creates problems with defining when the pump pulse should arrive, and produces datasets which have different effective time zeroes [15]. The second problem is that the optical constants will evolve after photoexcitation as the THz pulse propagates, so the full dynamics may not be captured.

These problems are exacerbated when the response of the sample is comparable to or faster

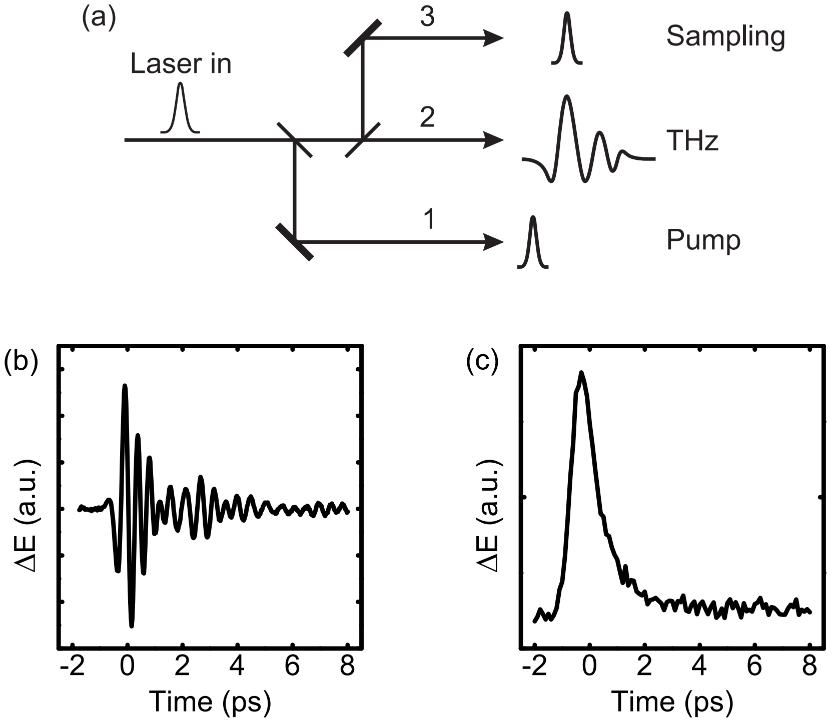

Figure 4.6: Effect of delay lines in TRTS. (a) Schematic of the delay lines explained in section 4.4.1. (b) Measuring pump-induced changes to the whole THz field. (c) Measuring pump-induced changes to the peak of the field.

than the THz pulse duration, as is the case in figures 4.6(b) and 4.6(c). There, 1D probe scans adequately show what is happening at times greater than $\sim 2\,\mathrm{ps}$, where the response in figure 4.6(c) has settled into a constant value (on the timescales investigated). However, the interesting part of the response is clearly happening in the first couple of picoseconds. Figure 4.6(b) shows that the THz field has a duration of a couple of picoseconds, so that different parts of the pulse experience slightly different refractive indices.

The solution to these problems is to obtain a full 2D scan by synchronous scanning of the delay lines. The objective then is to fix the pump-probe delay between pump and THz sampling beams, so between lines (1) and (3) in figure 4.6(a), and to scan the THz field (2). In this way, every part of the THz field experiences the same pump delay, there is no ambiguity as to the position of time zero for a given pump delay, and the full frequency response as a function of time can be extracted for all times, even during the THz pulse [15, 118]. Cuts through the 2D dataset will produce either 1D probe or 1D pump scans, like those of figures

4.6(b) or 4.6(c), respectively, but only the full 2D scan can be used to determine the complete temporal and frequency response of the sample under scrutiny.

4.5 Determining the Transient Optical Properties

Time-resolved THz spectroscopy maps changes in the electric field of a THz transient in time in response to an excitation laser pulse. A 2D dataset of $\Delta E(t,\tau)$ is produced, as outlined in section 4.4.1, where t describes the EOS time delay and τ describes the pump-sampling probe delay. Fourier transformation then yields frequency information via $\Delta\widetilde{E}(\omega,\tau)$. The transient changes in the field need to be processed as in the static case of section 4.3 in order to provide information on the evolving optical properties of the sample. However, due to the nature of photoexcitation there are complications which prevent the straightforward analysis already presented from being universally applied to time-resolved measurements.

As it propagates through a medium, light is absorbed and the intensity of a laser pulse decreases exponentially according to Beer's Law

$$I(z) = I_0 e^{-\alpha z}, \tag{4.18}$$

where α is the absorption coefficient and $1/\alpha$ gives the penetration depth [101]. This results in a spatially-varying distribution of photoexcited carriers, so that the optical properties tend to vary not only in time but in space as well. In transmission measurements, for thin films with a thickness less than the penetration depth of the pump, this spatial variation can be largely ignored and the sample may be treated as though it has been homogeneously excited [113, 119, 120].

For thicker samples where the pump beam penetration depth is not comparable to the sample thickness, the difference in penetration depths of THz and pump beams may be accounted for using transfer-matrix methods [111], though often the long-wavelength nature of THz radiation can be used to simplify these procedures. Such cases arise when the penetration depth of the THz pulse is considerably greater than the penetration depth of the pump pulse; the photoexcited region can then be considered as a homogeneous slab of finite thickness on the surface of an unexcited sample. For these thin film cases, the Tinkham formula [121] can be applied to find the conductivity of the layer for transmission measurements [122, 123].

With opaque samples, these approaches can also be applied, though the consideration now

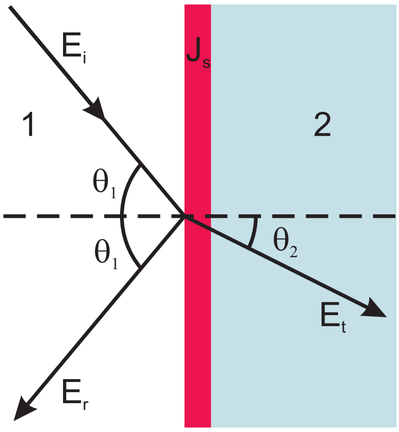

Figure 4.7: Approximating a photoexcited sample by a thin film (red) on an unexcited sample substrate (blue). E_i, E_r, and E_t represent the incident, reflected, and transmitted THz electric fields respectively. J_s is the current induced in the film.

is in terms of the reflectivity rather than the transmission. The THz penetration depth must be much larger than the pump penetration depth, $\delta \gg d$, for the thin film approximation to be valid; then the pump penetration depth d is taken to be the thickness of the film. Figure 4.7 illustrates this scenario, where the photoexcited thin film (red) sits on top of the unexcited sample volume (blue). The THz field is incident at an angle θ_1 relative to the surface normal.

A THz field induces a surface current density $j_s = \sigma E$ [101] and if the wavelength of the THz pulse is also larger than d then the electric field may be taken to be uniform across the film. The film separates media 1 and 2, and the THz fields must satisfy the boundary conditions

$$\mathbf{n} \times (\mathbf{H}_1 - \mathbf{H}_2) = \int_0^\infty j_s dz \,, \tag{4.19}$$

$$\mathbf{n} \times (\mathbf{E}_1 - \mathbf{E}_2) = 0 \,. \tag{4.20}$$

As the field is taken to be uniform throughout the film, the integral in equation (4.19) simplifies to J_s, where J_s is the current in the thin film. Looking at figure 4.7 and taking the THz pulses to be s-polarised, the boundary conditions yield

$$(H_i - H_r)\cos\theta_1 - H_t \cos\theta_2 = J_s \,, \tag{4.21}$$

$$E_i + E_r = E_t \,. \tag{4.22}$$

The ratio of magnetic to electric fields is given by the admittance, $Y = H/E$, which is the inverse of the impedance, $Z = 1/Y$. Making the definition

$$Y_{\pm} = Y_1 \cos\theta_1 \pm Y_2 \cos\theta_2 \tag{4.23}$$

and combining the boundary conditions (4.21) and (4.22), the reflected field for s-polarisation can be expressed as

$$E_r = \frac{1}{Y_+}\left(Y_- E_i - J_s\right) . \tag{4.24}$$

Now, the surface current density was given above as $j_s = \sigma E$, so for a uniform field over the film the surface current is given by $J_s = \sigma E d = (E_i + E_r)\sigma d$. This allows equation (4.24) to be rearranged to produce the reflection coefficient:

$$r = \frac{E_r}{E_i} = \frac{Y_- - \sigma d}{Y_+ + \sigma d} . \tag{4.25}$$

Finally, the admittance can be rewritten in terms of the impedance as $Y = 1/Z = n/Z_0$, where n is the refractive index of the medium and Z_0 is the impedance of free space ($Z_0 = 377\,\Omega$). The reflection coefficient then takes a form akin to the Fresnel form of (4.9):

$$r = \frac{n_1 \cos\theta_1 - n_2 \cos\theta_2 - Z_0 \sigma d}{n_2 \cos\theta_1 + n_2 \cos\theta_2 + Z_0 \sigma d} . \tag{4.26}$$

This equation expresses the reflectivity from the thin-film–substrate combination and is completely general. It may be used for static problems if the film is thinner than the THz penetration depth through both film and substrate, and for dynamic problems assuming the pump penetration depth is much smaller than that of the THz.

In the case of time-resolved measurements, the conductivity in equation (4.26) should be regarded as the change in conductivity of the sample rather than the conductivity of the film itself. This becomes clear by considering the behaviour before photoexcitation, when no film exists. Within the thin film approximation, the thickness of the layer is determined by the equilibrium optical properties. As such, the region of space which will become ‘occupied’ by the layer can be thought to always exist but with a conductivity given by the equilibrium conductivity. Thus the pump beam contributes to this conductivity and in time the film properties revert back to those of the bulk. Therefore, in equation (4.26) σ is rewritten as $\Delta\sigma$ to reflect this important point.

Since TRTS measures $\Delta E(t)$, $\Delta r(\omega)$ is an important quantity. By analogy with the static case in section 4.3.3, TRTS will rely heavily on a formula similar to equation (4.12). In the time-resolved situation, the reference quantities $\widetilde{E}_0(\omega)$ and $r_0(\omega)$ are now provided by the unperturbed sample, turning equation (4.12) into

$$\Delta r(\omega) = \frac{\Delta\widetilde{E}(\omega)}{\widetilde{E}(\omega)}\, r(\omega)\,, \tag{4.27}$$

which relates the changes in measured electric field and reflectivity ($\Delta\widetilde{E}(\omega)$ and $\Delta r(\omega)$) to the equilibrium measurements of the sample ($\widetilde{E}(\omega)$ and $r(\omega)$).

In all cases to be considered, medium 1 will be vacuum and medium 2 will be the sample, so that $n_1 = 1$ and $n_2 = n$. Then, using equations (4.27) and (4.12) for the perturbed and unperturbed reflectivities, respectively, together with the Fresnel relations (4.9) and (4.26), the ratio $\Delta r/r$ may be expressed as

$$\frac{\Delta r}{r} = \left(\frac{\cos\theta_1 - n\cos\theta_2 - Z_0\sigma d}{\cos\theta_1 + n\cos\theta_2 + Z_0\sigma d}\right)\left(\frac{\cos\theta_1 + n\cos\theta_2}{\cos\theta_1 - n\cos\theta_2}\right) - 1\,. \tag{4.28}$$

Snell's Law eliminates θ_2 via $\cos\theta_2 = \sqrt{1 - \frac{1}{n^2}\sin^2\theta_1}$, and equation (4.28) can be inverted to give the change in conductivity after photoexcitation:

$$\Delta\tilde{\sigma}(\omega) = \frac{1}{Z_0 d}\,\frac{\dfrac{\Delta\widetilde{E}(\omega)}{\widetilde{E}(\omega)}\left(\tilde{n}^2\sqrt{1 - \dfrac{1}{\tilde{n}^2}\sin^2\theta} - \cos^2\theta\right)}{\dfrac{\Delta\widetilde{E}(\omega)}{\widetilde{E}(\omega)}\left(\cos\theta - \tilde{n}\sqrt{1 - \dfrac{1}{\tilde{n}^2}\sin^2\theta}\right) + 2\cos\theta}\,, \tag{4.29}$$

where the subscript 1 has been dropped from θ since only the incident angle is now involved, and relation (4.27) has been used to replace the reflectivities with the measured THz field quantities. Tildes have been re-inserted to indicate those symbols that are complex quantities.

This treatment allows for the extraction of the complex optical conductivity of a photoexcited material at arbitrary delay times using measurements of the unperturbed THz field and the pump-induced changes to it. Aside from these experimental quantities, equation (4.29) also requires the complex refractive index of the sample in the range of the THz spectrum to be known, though this can be found using the THz-TDS technique described in section 4.3.

4.6 Summary

Summarising the procedures outlined in the preceding sections, reflection-based TRTS requires measurements of THz transients from the sample under study, $E(t)$, and from a known reference, $E_0(t)$, as well as measurements of the pump-induced changes to the THz field at a series of time delays, $\Delta E(t,\tau)$. Fourier transformation of these quantities yields the complex frequency-domain variables $\widetilde{E}(\omega)$, $\widetilde{E}_0(\omega)$, and $\Delta\widetilde{E}(\omega)$. By proper acquisition of these differential measurements, the optical properties of the sample may be deduced for all times before and after arrival of the pump pulse. This is achieved using the following relations:

$$r(\omega) = \frac{\widetilde{E}(\omega)}{\widetilde{E}_0(\omega)}\, r_0(\omega)\,, \tag{4.30}$$

$$\tilde{\sigma}(\omega) = i\omega\varepsilon_0 \cos^2\theta \left(1 - \left(\frac{1-r(\omega)}{1+r(\omega)}\right)^2\right), \tag{4.31}$$

$$\Delta\tilde{\sigma}(\omega) = \frac{1}{Z_0 d}\, \frac{\dfrac{\Delta\widetilde{E}(\omega)}{\widetilde{E}(\omega)}\left(\tilde{n}^2\sqrt{1-\dfrac{1}{\tilde{n}^2}\sin^2\theta} - \cos^2\theta\right)}{\dfrac{\Delta\widetilde{E}(\omega)}{\widetilde{E}(\omega)}\left(\cos\theta - \tilde{n}\sqrt{1-\dfrac{1}{\tilde{n}^2}\sin^2\theta}\right) + 2\cos\theta}\,. \tag{4.32}$$

The reflectivity $r_0(\omega)$ is known, since it is from a reference reflector; this should be a well-understood material with a flat THz response, such as gold. ε_0 and Z_0 are the permittivity and impedance of free space respectively, d is the penetration depth of the pump beam, θ is the THz beam angle of incidence, and $\tilde{n}$ is the complex refractive index of the unexcited sample.

The terahertz spectroscopic techniques discussed throughout this chapter provide a powerful set of tools for determining the low-frequency optical properties of both equilibrium and transient photoinduced phases. The encapsulation of both amplitude and phase information into the measurement removes the reliance on extrapolation and models inherent to pre-exisiting techniques. While time-domain spectroscopy only generates information in a relatively narrow spectral range, it does so in a single measurement and can be easily switched between time-resolved and static measurements in either reflection or transmission geometries and at any temperature. This versatility makes time-resolved THz spectroscopy an appealing prospect with a wealth of applications in ultrafast science.

Chapter 5

The Photoinduced Phase of 1*T*-TaS_2

5.1 Ultrafast Dynamics in 1*T*-TaS_2

As detailed in chapter 2, investigations into the curious behaviour of TaS_2 began in the middle of the twentieth century, where its two-dimensional characteristics made it, and other transition metal dichalcogenides, a rich test bed for charge density wave (CDW) phenomena [39]. However, due to the coexistence of a Mott state with the commensurate CDW, TaS_2 is unique among this class of materials.

The ultrafast dynamics of TaS_2 have been studied for almost a decade now, beginning with temperature-dependent measurements of the single particle and collective response to photoexcitation [35]. The formation of the photoinduced phase was monitored by Perfetti et al. using time-resolved photoemission [28]. They found that the Mott gap was melted within their experimental resolution ($\sim$ 50 fs) due to electronic temperature effects, with only a weak influence from CDW excitation. Femtosecond electron diffraction then helped substantiate this view somewhat more by showing that photoexcitation does not trigger a complete relaxation of the structural distortion caused by the CDW [71]. Further details can be found in chapter 2.

From these previous investigations, the emerging picture is one of a transient phase in which the Mott state is melted by light whilst the lattice symmetry is only weakly perturbed, such that the CDW state remains essentially unaltered. Such a state does not exist in the equilibrium phases of TaS_2, outlined in section 2.4; the Mott behaviour usually always appears alongside the low-temperature lattice symmetry.

However, whilst these investigations provide crucial pieces of information about the single-particle gap and the CDW order parameter, a more detailed understanding of the electrodynamics of the transient phase is lacking. Studying the transport properties of the transient phase is appealing because of the strong electron-electron and electron-phonon interactions which exist in this material. Disrupting the electron correlations and exciting the lattice leads to a novel phase which has potentially very interesting properties arising from the changes in interactions. Such a study requires a combination of optical probes spanning a broad range of frequencies, with each portion of the spectrum presenting its own set of technical challenges.

This chapter reports on ultrabroadband time-resolved measurements of photoexcited $\mathrm{TaS_2}$, covering nearly three decades in frequency from the terahertz (THz) ($\sim 1\,\mathrm{THz}$) to the visible ($\sim 500\,\mathrm{THz}$). These investigations characterise the photoinduced phase, shedding light on the interplay between electrons and the lattice in this system. $\mathrm{TaS_2}$ provides an interesting choice for the application of these broadband techniques, the development of which could in future be applied to a variety of complex materials. The experiments in the THz region (between 1 and around $3\,\mathrm{THz}$) will be discussed first, followed by the mid-infrared to visible pump-probe measurements, since the experimental techniques and interpretation of the data are markedly different in the two cases. Before discussing the experiments, however, a description of the Fano effect is given, which will be important for the study of the phonon modes in section 5.3.

5.2 Fano Resonances

The study of phonon resonances is important to understand the structural properties of a material. The approaches of Raman and IR spectroscopy provide a means to study phonons in equilibrium states, producing spectra containing resonance features which can be described by symmetric Lorentzian lineshapes. Phonon resonances can also be studied through THz time-domain spectroscopy, as shall be seen in section 5.3. These lineshapes reveal the phonon frequency and lifetime through their central position and linewidth, respectively. However, when the phonons interact strongly with other excitations in the system, these resonances can become asymmetric.

Asymmetric resonances have been observed for a long time, beginning with Beutler's asymmetric profiles in the Rydberg lines from some noble gases in 1935 [124]. Ugo Fano offered an explanation of this phenomenon based on quantum mechanical superposition principles [125]. He later expanded and elaborated on this theory in what was to become one of the most frequently cited papers in *Physical Review* [126].

Within the context of atomic spectra, Fano suggested that coupling via a 'configuration interaction' between a discrete state and an energetically degenerate continuum of states modifies the discrete state. More specifically, the discrete state contains an admixture of the continuum states, which alters the transition amplitude to the discrete state. He showed that, irrespective of the excitation mechanism, a transition via a suitable operator T between an initial state i and a state Ψ_E of the discrete–continuum configuration has the matrix element

$$\begin{aligned}\langle\Psi_E|T|i\rangle = {}& \frac{1}{\pi V_E^*}\langle\varphi_E|T|i\rangle\sin\Delta \\ & + \frac{1}{\pi V_E^*}P\int dE'\frac{V_{E'}^*\langle\psi_{E'}|T|i\rangle}{E-E'}\sin\Delta - \langle\psi_E|T|i\rangle\cos\Delta,\end{aligned} \tag{5.1}$$

where φ and ψ_E represent the discrete state and the continuum of states, respectively, V_E gives the strength of the configuration interaction ($\langle\psi_{E'}|H|\varphi\rangle = V_{E'}$), and Δ is the phase shift arising from it. P indicates 'the principal part of' [126]. The square of equation (5.1) gives the probability of transitions from the initial state to the state at energy E within the configuration.

Simplifying equation (5.1) to

$$\langle\Psi_E|T|i\rangle = \frac{1}{\pi V_E^*}\langle\Phi_E|T|i\rangle\sin\Delta - \langle\psi_E|T|i\rangle\cos\Delta, \tag{5.2}$$

where

$$\Phi = \varphi + P\int dE'\frac{V_{E'}\psi_{E'}}{E-E'}, \tag{5.3}$$

reveals the modification to the discrete state. The phase parameter Δ varies sharply as the energy crosses the resonance. As can be seen from equation (5.2), the sine and cosine terms mean that around the resonance there is interference with opposite phase due to contributions from transitions to the discrete state and to the continuum. Thus the transition probability vanishes on one side of the resonance and is enhanced on the other; this is the root of asymmetric profiles in resonance features.

A further consequence of the interaction is a shift in the resonance energy from the position of the unperturbed level. Experimentally, this means that spectroscopic measurements will

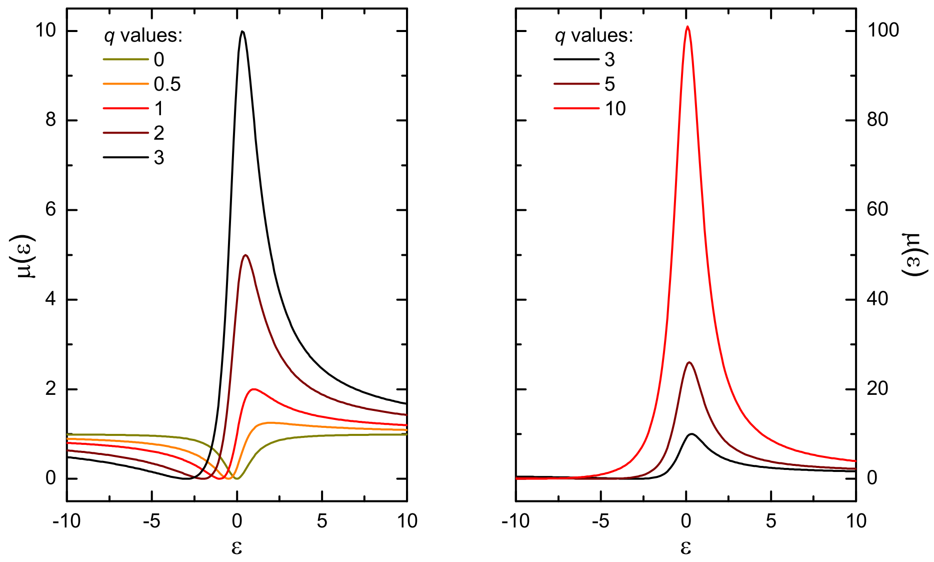

Figure 5.1: Fano lineshapes for different asymmetry parameters q.

determine the perturbed resonance energy $E_\varphi + \Delta E$ rather than the unperturbed energy E_φ. Similarly, information is provided on the modified state Φ and not φ.

Fano went on to give the lineshape for the resonance profile as[*]

$$\mu = \mu_0 \frac{(q+\epsilon)^2}{1+\epsilon^2}, \tag{5.4}$$

where $\epsilon = (E - E_\phi - \Delta E)/\frac{1}{2}\Gamma$ is the dimensionless reduced energy parameter, Γ is the spectral width of the state φ, μ_0 represents the background cross section, and q is the Fano asymmetry parameter [126]. The asymmetry parameter can be interpreted as the ratio of matrix elements for transitions between some initial state and two excited states [127]. One of these elements is the amplitude for transitions into the modified discrete state in the presence of the interaction, while the other is the amplitude to go first into the continuum and then into the discrete state via the discrete–continuum interaction. The presence of an asymmetric profile may then be thought of as arising from interference between two quantum pathways for a transition.

Figure 5.1 illustrates some example Fano lineshapes. In the limit $|q| \to \infty$, transitions to the continuum are weak and the lineshape returns to the symmetric Lorentzian form, $\mu \propto 1/(1+\epsilon^2)$. When $q = 1$, the amplitudes for the two transitions are equal and the profile becomes maximally asymmetric. The limit of $q = 0$ gives a symmetric Lorentzian dip known

---

[*] Note that the symbol μ is used here to represent the scattering cross section profile, rather than the more traditional σ. This is to avoid later confusion with the optical conductivity σ.

as an antiresonance. For $q < 0$, the shape flips about $\epsilon = 0$, with the sharp rise occurring for $\epsilon > 0$ and the slow fall for $\epsilon < 0$. In general, the asymmetry parameter is discussed in terms of $1/q$ rather than q, since $1/q$ is roughly proportional to the interaction strength. Thus larger $1/q$ denotes a more asymmetric shape.

The Fano effect is a completely general spectroscopic feature, which is not limited to its original context of photoionisation spectra. Whilst it has found a place in atomic, molecular, and orbital physics, it is also frequently applied to various condensed matter systems, such as quantum dots [128], nanoscale structures [129], and a variety of bulk solids [130–133], where it has proven useful in interpreting transport and optical properties. In condensed matter systems, the discrete state is usually a phonon mode, which interacts with an electronic continuum. Investigations of the Fano effect in this way have led to an understanding of the interaction between electrons and the lattice, and their combined role in the optical properties of correlated materials [132, 134]. More recently, photoinduced Fano effects have been observed in semiconductors and metals [135–137]. Such studies have led to a deeper understanding of the ultrafast dynamics between electrons and the lattice.

The Fano form of the dielectric function $\varepsilon(\omega)$ was first elaborated by Davis and Feldkamp [138]. Using their derivation, the conductivity close to a resonance feature due to the Fano effect is given by

$$\sigma_{\mathrm{Fano}}(\omega) = i\sigma_0 \frac{(q-i)^2}{\left(i + \frac{\omega^2 - \omega_0^2}{\gamma_0 \omega}\right)}, \tag{5.5}$$

with

$$\sigma_0 = \frac{\omega_p^2}{\gamma_0 q^2}, \tag{5.6}$$

where ω_0 and γ_0 are the resonance frequency and linewidth, respectively, and ω_p gives the strength of the resonance [131, 139].

Figure 5.2 shows some example conductivity profiles using equation (5.5). As can be seen, the Fano effect results in mixing of the real and imaginary parts of the complex conductivity as $1/q$ grows, i.e. as the interaction with the configuration increases. Measurements of the complex conductivity $\sigma(\omega)$ or dielectric constant $\varepsilon(\omega)$ in condensed matter systems can then reveal the existence of interactions between different degrees of freedom.

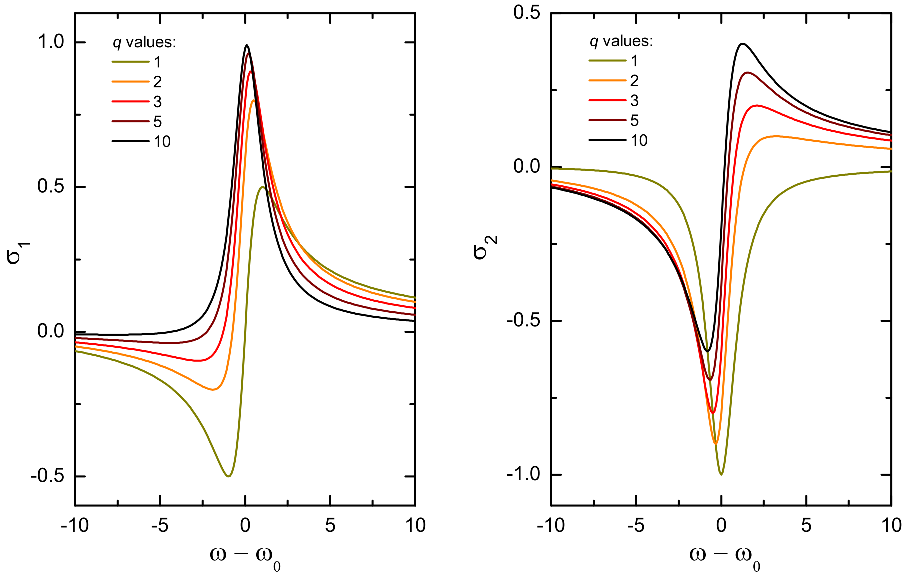

Figure 5.2: Fano conductivity profiles, showing real (left) and imaginary (right) parts of the conductivity.

5.3 Terahertz Experiments

5.3.1 Experimental setup

The time-resolved THz spectroscopy experiments were carried out using a 1.3 µm pump pulse and a broadband THz probe pulse. The pump pulse was created using an optical parametric amplifier (OPA), as outlined previously in section 3.2. The OPA was used to simplify the timing between pump and probe for the later experiments which would require a second OPA. The choice of 1.3 µm wavelength was made since this was a stable high-power wavelength for the OPA, but which was also close to that of the earlier pump-probe experiments performed at 800 nm [28, 35, 71]. This placed the pump energy (950 meV) well above the Mott gap energy (100 meV) and allowed for direct comparisons between these measurements and the results of previous experiments. The THz transients were generated using optical rectification and detected by electro-optic sampling (EOS), using ZnTe crystals as described in chapter 4. For both pump and probe generation, the source was Ti:sapphire amplified laser system operating at 1 kHz, with a central wavelength of 800 nm and pulse duration of 60 fs.

As also mentioned in chapter 4, it is desirable to perform the THz measurements under vacuum to produce cleaner signals. This led to the creation of a vacuum chamber which took the innovative step of placing all the THz generation and detection optics together with the cryostat cold finger and sample in one enclosure. This prevented losses of THz power due to transmission through cryostat windows, permitted cryogenic cooling of the sample, and allowed for arbitrary angles of incidence for both pump and probe beams, unencumbered by the geometry of the usual cryostat outer casing.

An additional benefit was the ability to use short focal length optics for the THz beam. Due to the long wavelength of the THz pulses, typically centred around 200 μm, it is difficult to achieve spot sizes of less than a few hundred micron without using very short focal length optics or expanding the beam before focussing. A reasonable spot size of 500 μm diameter could be achieved using a 50 mm focal-length 90° off-axis parabolic mirror, without crowding the cold finger with focussing and re-collimating elements. This also meant that the pump spot could be kept at around 1 mm diameter, so that intensities on the order of $1\,\mathrm{mJ\,cm^{-2}}$ could still be attained.

The experimental layout for the THz spectroscopy measurements is sketched in figure 5.3. Two mechanical chopper wheels were used on either the THz path or the pump path to allow for lock-in detection of THz transients or differential THz traces. The 800 nm beam was blocked after THz generation using black rubberised fabric, which is transparent in the THz region. A wire grid polariser was then used to clean up the THz polarisation, which was s-polarised. After reflection from the sample, the THz and electro-optic sampling beams were combined collinearly using a 90° off-axis parabolic mirror with a small hole drilled through it. For the pump beam, a silicon wafer was used to block parasitic light at visible wavelengths, while a pair of polarisers allowed for continuous control of the pump intensity without altering its polarisation.

Due to their inherently two-dimensional nature, samples of TaS$_2$ exist as thin slivers of a few millimetres in diameter. A portion of the surface was coated with a 200 nm layer of gold to provide a reference for the THz measurements. The sample was then mounted onto the tip of a helium-cooled closed-loop cryostat cold finger. The THz angle of incidence was 45° while the pump was focussed at normal incidence.

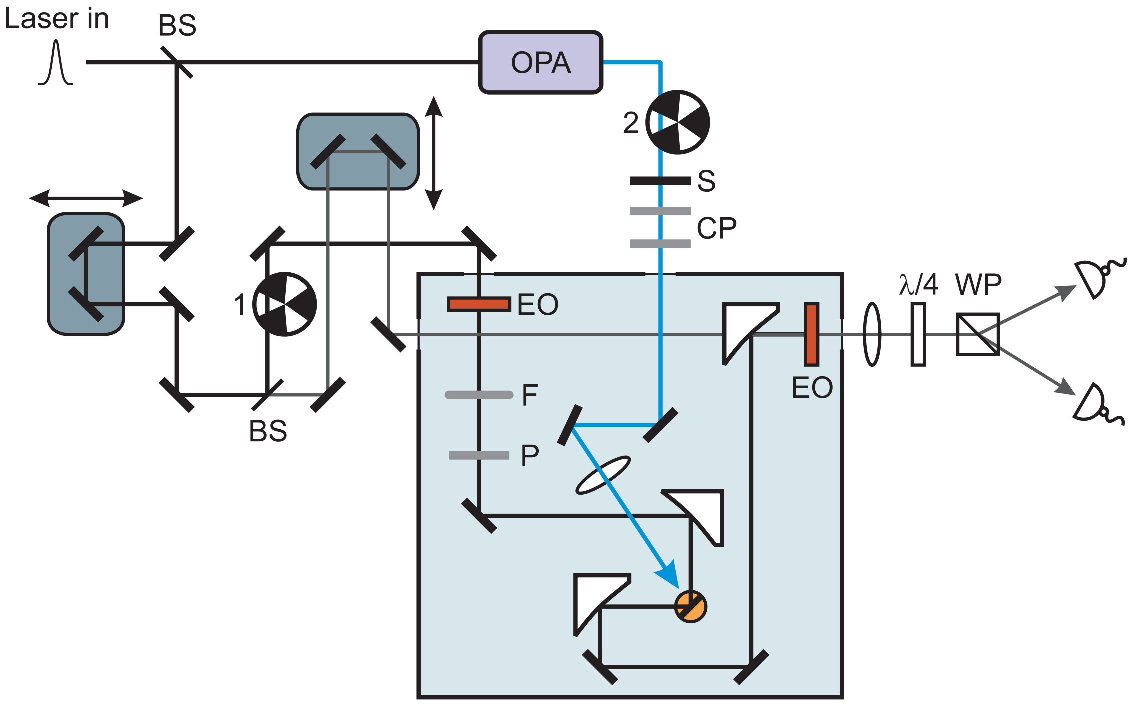

Figure 5.3: Experimental layout for the time-resolved THz spectroscopy measurements. BS – beam splitter. EO – electro-optic crystal. F – THz filter. P – THz polariser. $\lambda/4$ – quarter-wave plate. WP – Wollaston prism. S – silicon. CP – crossed polarisers. The orange circle represents the cryostat cold finger with the sample (black line) mounted on top. The light blue box represents the vacuum chamber and grey-blue boxes are delay stages. 1 and 2 label the two chopper wheels.

5.3.2 Static measurements

Before performing time-resolved measurements in the THz region, it was important to carry out static measurements to determine the low-frequency conductivity of TaS_2. These could be performed using the setup of figure 5.3 by blocking the pump beam and using chopper 1. Detection then proceeded as outlined in section 4.2.

A first experiment measured simply the electric field reflected from the sample as a function of temperature close to the lock-in phase transition at $T_c = 180\,\mathrm{K}$. Figure 5.4 shows the acquired electric fields and their associated fast Fourier transform (FFT) spectra. The time-domain data show that as the temperature is lowered there is a drop in the measured electric field strength. At 180 K there is also the sudden appearance of additional ripples for times

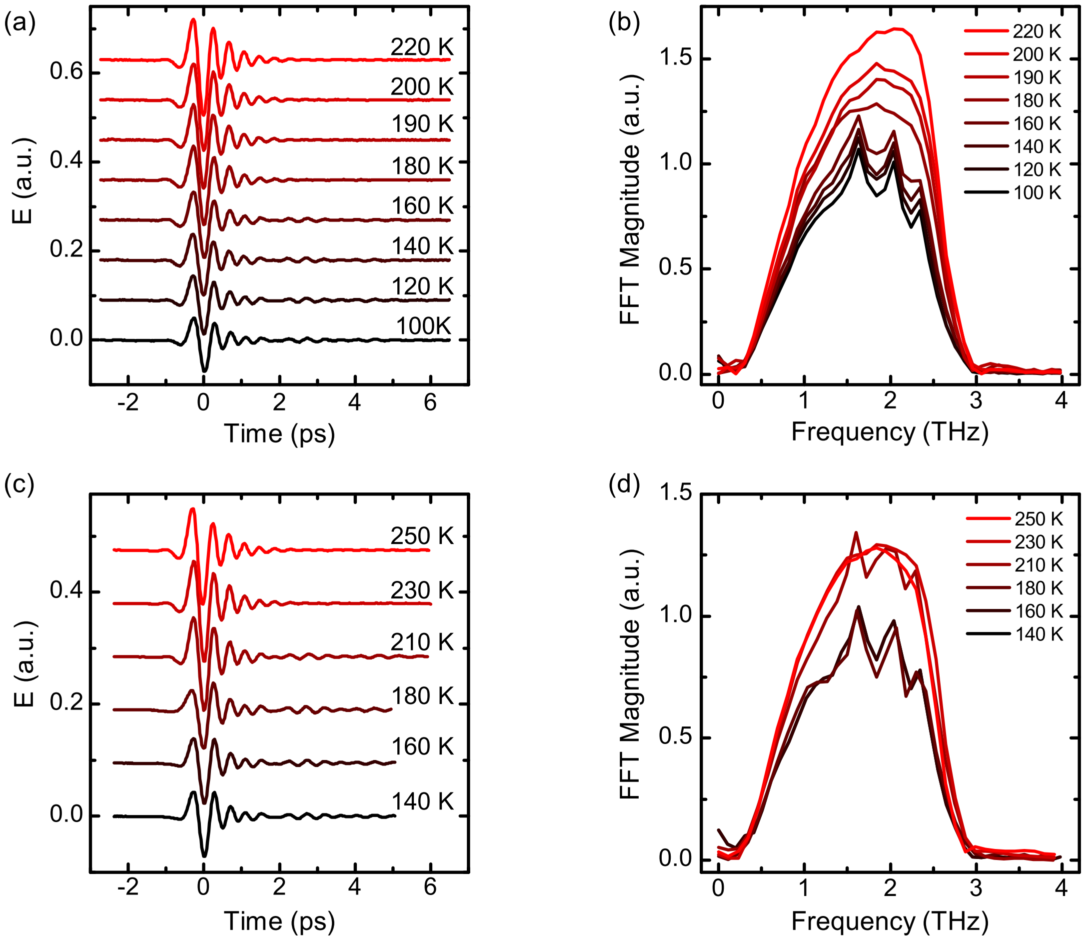

Figure 5.4: Temperature-resolved THz measurements on TaS$_2$ across the thermal phase transition at $T_c = 180\,\mathrm{K}$. (a) and (b) show cooling down through the transition; (c) and (d) are warming up through it.

$t > 2\,\mathrm{ps}$. In the frequency domain, these ripples correspond to the appearance of peaks in the spectrum centred at approximately 1.6, 2.0, and 2.3 THz. These findings correspond to the temperature-dependent drop in reflectivity and the appearance of IR active modes at the lock-in transition, as observed in previous studies [32, 60]. These modes can therefore act as a fingerprint to identify the onset of the transition. Furthermore, on heating the sample from below T_c, hysteresis effects are seen which are consistent with FTIR and resistivity measurements [53, 60].

What sets THz time-domain spectroscopy (THz-TDS) apart from more traditional IR spectroscopy methods is its ability to capture the complex optical constants directly, without reliance on Kramers-Kronig relations (as in FTIR techniques) or multiple angles of incidence (as in ellipsometry). The complex conductivity $\tilde{\sigma}(\omega) = \sigma_1(\omega) + i\sigma_2(\omega)$ of TaS_2 at 15 K was obtained using the method laid out in section 4.3.3. More details can be found there; here, only the important relations are given. The procedure requires a comparison of THz transients reflected from the sample and from a known reference reflector. In the present case, the reference is the gold-coated part of the sample. Equations (4.12) and (4.17) give the optical constants as

$$r(\omega) = \frac{\widetilde{E}(\omega)}{\widetilde{E}_0(\omega)}\, r_0(\omega), \tag{5.7}$$

$$\tilde{\sigma}(\omega) = i\omega\varepsilon_0 \cos^2\theta \left(1 - \left(\frac{1 - r(\omega)}{1 + r(\omega)}\right)^2\right), \tag{5.8}$$

where $\widetilde{E}(\omega)$ and $\widetilde{E}_0(\omega)$ come from the experimentally obtained electric fields from the sample and the reference, respectively, θ is the angle of incidence, ε_0 is the permittivity of free space, and $r_0(\omega)$ is the reflectivity of the reference.

The reflectivity of gold was calculated using the Drude model for conductivity,

$$\tilde{\sigma}(\omega) = \frac{\varepsilon_0 \omega_p^2 \tau}{1 - i\omega\tau}, \tag{5.9}$$

where $\tau = 24.5\,\mathrm{fs}$ and $\omega_p/2\pi = 2175\,\mathrm{THz}$ are the scattering time and plasma frequency, respectively, taken from literature values [122, 140]. The reflectivity can then be determined by using this in the Fresnel relation

$$r_0(\omega) = \frac{\cos\theta - \sqrt{n_g^2 - \sin^2\theta}}{\cos\theta + \sqrt{n_g^2 - \sin^2\theta}}, \tag{5.10}$$

where n_g is the refractive index of gold, given by $n_g^2(\omega) = \tilde{\varepsilon}_g(\omega) = 1 + i\tilde{\sigma}_g(\omega)/\omega\varepsilon_0$. Using this value for $r_0(\omega)$ in equation (5.7) produces the reflectivity of the sample $r(\omega)$, which in turn yields its conductivity $\tilde{\sigma}(\omega)$.

Figure 5.5 shows $\tilde{\sigma}(\omega)$ obtained in this way. In section 4.3.4 the problem of phase shifts in THz-TDS was discussed. To correct for phase differences appearing when raising and lowering the sample between gold-coated and uncoated regions, an additional phase term was introduced as outlined in section 4.3.4. The extracted conductivity was then compared with FTIR measurements from Gasparov et al. [60] to ensure that the general features were the

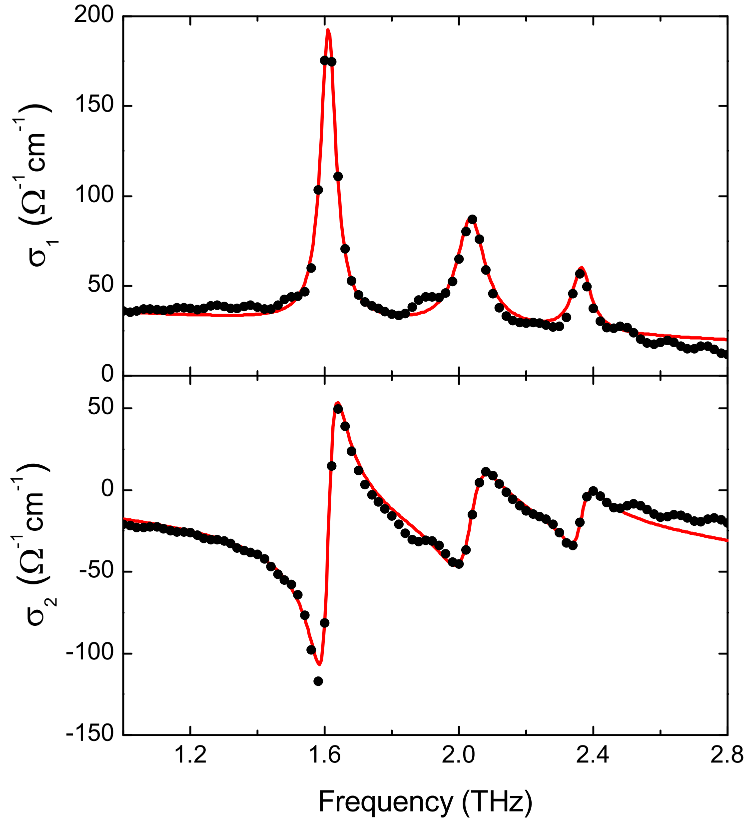

Figure 5.5: Complex conductivity $\tilde{\sigma}(\omega)$ of TaS$_2$ obtained at 15 K. Black dots are data for the real (σ_1, top) and imaginary (σ_2, bottom) parts of the conductivity. Red lines are the associated fits.

same, i.e. reasonable mode shapes and similar background $\sigma_1(\omega)$. A phase shift of $\omega\Delta t$, with $\Delta t = 5$ fs, was required to obtain the conductivity in figure 5.5. This introduces a phase shift of 0.03 rad at 1 THz. The three peaks apparent in the spectra of figure 5.4 become three pronounced resonances in the optical conductivity, corresponding to the three lowest-lying phonon modes also observed elsewhere [32, 60]. The general shape and size of $\tilde{\sigma}(\omega)$ in this region also closely resemble these earlier studies.

In THz-TDS, the frequency resolution is dictated by the duration of the THz pulses. In the experiments performed in this chapter, the measured THz transients were found to have usable non-zero content over some 12 ps. This provides a spectral resolution of approximately 0.08 THz. Zero-padding has been used to interpolate the experimental data and produce the conductivity shown in figure 5.5.

j	ω_{0j} (THz)	γ_j (THz)	S_j
1	1.61 (0.06)	0.05 (0.08)	6.0 (3.3)
2	2.03 (0.03)	0.10 (0.17)	2.7 (1.8)
3	2.36 (0.16)	0.05 (0.48)	0.7 (1.0)

σ_0 ($\Omega^{-1}\,\mathrm{cm}^{-1}$)	τ (fs)	ε_∞
39.9 (27.6)	56.1 (92.2)	40.7 (25.3)

Table 5.1: Drude-Lorentz fit parameters for $\mathrm{TaS_2}$ at 15 K using equation (5.11). Uncertainties in brackets are the 95% confidence intervals from the least-squares fit.

The optical conductivity may be analysed according to the Drude-Lorentz model, a phenomenological model using harmonic oscillators to describe the response of the system [139, 141]. Within this framework, the complex optical conductivity is given by

$$\sigma(\omega) = \frac{\sigma_0}{1 - i\omega\tau} + i\varepsilon_0\omega\left(1 - \varepsilon_\infty - \sum_{j=1}^{n} S_j \frac{\omega_{0j}^2}{\omega_{0j}^2 - \omega^2 - i\omega\gamma_j}\right). \tag{5.11}$$

The first term is simply the Drude conductivity from equation (5.9), with $\sigma_0 = \varepsilon_0\omega_p^2\tau$. The term ε_∞ represents the high-frequency response of the dielectric constant. The last term gives the contribution from the j^{th} Lorentzian harmonic oscillator, where S_j is the oscillator strength, ω_{0j} is the resonance frequency, and γ_j is its linewidth.

The red line in figure 5.5 is the least-squares fit to the data obtained using this model. Both real and imaginary parts are fit simultaneously, imposing additional constraints on the parameters. Table 5.1 lists the fit parameters for equation (5.11) applied to the unpadded THz conductivity, so with the experimental frequency resolution of 0.08 THz discussed above. The uncertainties in brackets are the 95% confidence intervals from the least-squares fit. The mode frequencies match the phonon frequencies already in the literature [32, 60] and the value of σ_0 found is a good measure of the low-frequency conductivity, in close agreement with other studies [53, 60]. However, the frequency window is a little too narrow to accurately determine the scattering time τ for the Drude component. Overall, the fit is good and accurately describes the data.

These initial findings confirm the validity of using THz-TDS to measure the optical properties of TaS$_2$. The technique is able to reliably reproduce the conductivity within the measurement bandwidth, in good agreement with existing studies. These equilibrium phase measurements can now be used in conjunction with the differential measurements of the time-resolved experiments to reconstruct the optical properties of the transient photoinduced phase.

5.3.3 Time-resolved measurements

The experimental setup for the time-resolved measurements was described in section 5.3.1 and is drawn in figure 5.3. Using a pair of crossed polarisers, the 1.3 µm pump intensity could be continuously varied up to $\approx 1\,\mathrm{mJ\,cm^{-2}}$, whilst the signals showed no dependence on the pump polarisation. As discussed in section 4.4, scanning different delay lines relative to one another results in different types of data acquisition. The two key data types are differential EOS traces, which provide information on the full frequency response, and THz peak differential traces, which describe the average THz response. The former trace is referred to as a probe scan, while the latter is called a pump scan. Both require the use of chopper 2 only; further details on their intricacies can be found in section 4.4. In the discussion to follow, t describes the THz–EOS-probe delay time and τ describes the pump–THz delay time.

Probe scans were acquired for a number of different pump intensities and pump–THz delay times τ. In addition, pump scans were collected to monitor the overall response to photoexcitation. Figure 5.6 shows typical pump and probe scans taken in the experiment. A static EOS trace, used to reference the differential data, is given in figure 5.6(a). From the pump scan of figure 5.6(c), the general photoinduced dynamics become clear: there is a prompt increase in the reflected electric field on arrival of the pump pulse, followed by decay back towards equilibrium. After the first few picoseconds, the response does not return to zero but remains at a small but finite value. On timescales of hundreds of picoseconds to nanoseconds, this value gradually decays to zero as the system relaxes back to its ground state.

The probe scans of figure 5.6(b) reveal significant modulations to the THz field. Comparing figures 5.6(a) and (b), the bulk of the THz field, for times $-1 < t < 1\,\mathrm{ps}$, is enhanced by the pump pulse. For $t \gtrsim 2\,\mathrm{ps}$, there are interesting additional features that appear in the wake of the THz pulse. The probe traces also have an unusual behaviour as a function of τ:

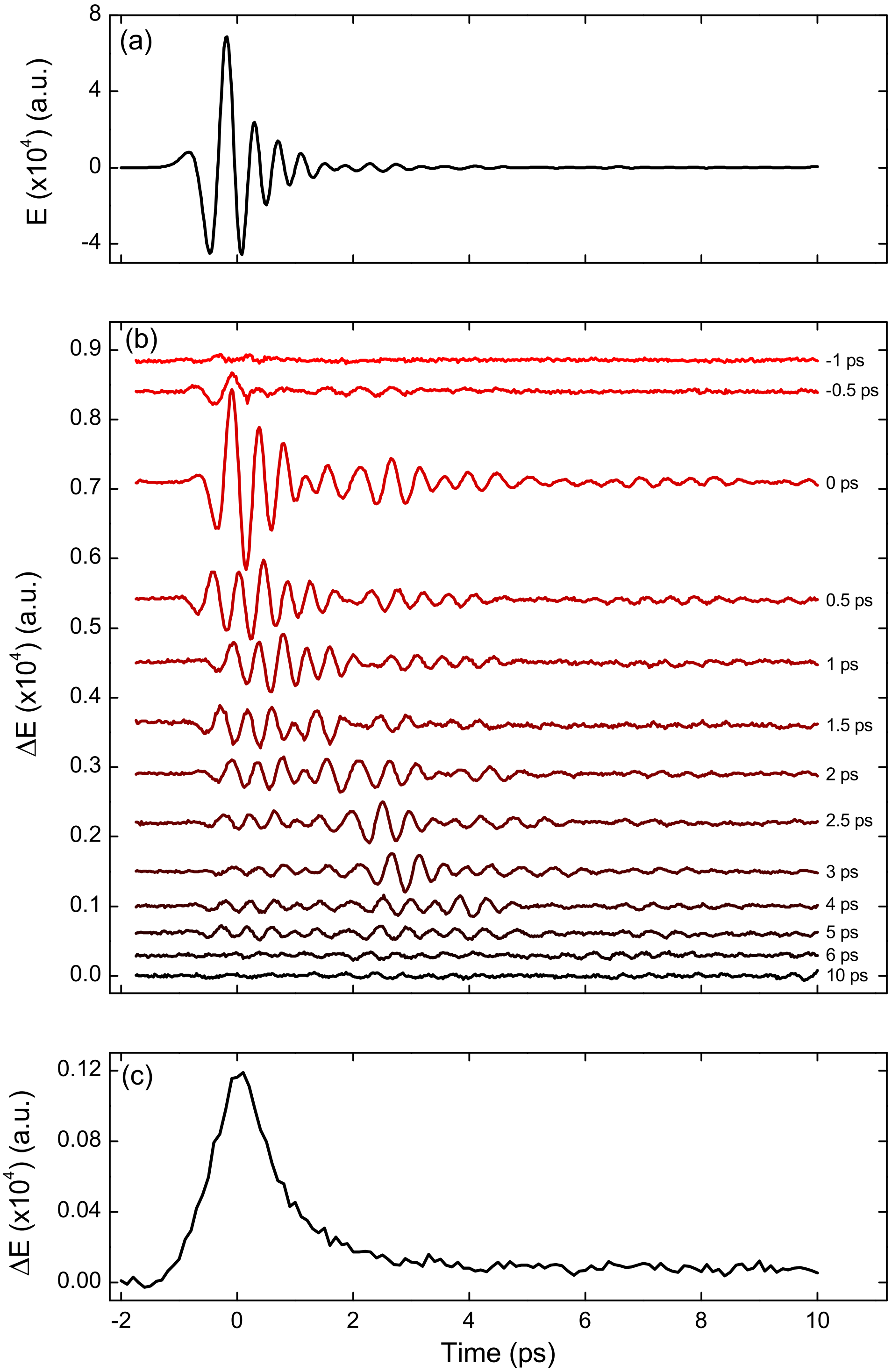

Figure 5.6: THz traces acquired from TaS_2 at the highest pump intensity. (a) Static EOS trace. (b) Differential probe traces for different pump delays. The time delay τ is indicated next to each trace. (c) Differential pump trace.

the main part of the THz field decreases in size, as indicated by the average THz response of figure 5.6(c), but in the tail there is no simple decay of ΔE. Instead, the signal drops then returns, shifting around in both t and τ.

The time-domain response itself cannot reveal the full behaviour of the system. Rather, the probe traces must be converted to the frequency domain if they are to provide any insight into what is going on. The pump traces cannot give specific information on the frequency-resolved dynamics. The full procedure for this transformation is given in section 4.5. In essence, it models the photoexcited sample as a two-layer system: one thin layer representing the excited region and one infinite layer representing the unperturbed bulk. The approximation requires the pump penetration depth d to be much smaller than that of the THz, δ; in the experiments here, $d = 45\,\mathrm{nm}$ and $\delta \approx 7\,\mu\mathrm{m}$, easily satisfying this condition. Then, from equation (4.29) with $\theta = 45°$, the conductivity change for a given pump–THz time delay τ in this thin-film limit is,

$$\Delta\tilde{\sigma}(\omega,\tau) = \frac{1}{Z_0 d}\,\frac{\dfrac{\Delta\widetilde{E}(\omega,\tau)}{\widetilde{E}(\omega)}\left(\tilde{n}^2\sqrt{1-\dfrac{1}{2\tilde{n}^2}}-\dfrac{1}{2}\right)}{\dfrac{\Delta\widetilde{E}(\omega,\tau)}{\widetilde{E}(\omega)}\left(\dfrac{1}{\sqrt{2}}-\tilde{n}\sqrt{1-\dfrac{1}{2\tilde{n}^2}}\right)+\sqrt{2}}\,, \tag{5.12}$$

where Z_0 is the impedance of free space, $\tilde{n}$ is the refractive index of the unperturbed sample, and $\Delta\widetilde{E}(\omega,\tau)$ and $\widetilde{E}(\omega)$ are the Fourier transforms of the probe traces $\Delta E(t,\tau)$ and the EOS trace $E(t)$, respectively. The refractive index of the sample can be calculated from the conductivity determined in section 5.3.2 using $\tilde{n}^2 = 1 + i\tilde{\sigma}(\omega)/\omega\varepsilon_0$.

The experimentally obtained probe traces for different time delays τ and different pump intensities were converted to conductivity changes $\Delta\tilde{\sigma}(\omega,\tau)$ using the above procedure. The full complex conductivity $\tilde{\sigma}(\omega,\tau)$ was recovered for all τ by adding $\Delta\tilde{\sigma}(\omega,\tau)$ to the previously obtained static conductivity. Figure 5.7(a) shows the real part of the conductivity σ_1 calculated for a pump intensity of $550\,\mu\mathrm{J\,cm^{-2}}$ for times $\tau \geqslant 0\,\mathrm{ps}$. Figure 5.7(b) shows selected σ_1 after photoexcitation. The equilibrium σ_1 at 15 K (from THz-TDS) and at 230 K (from FTIR measurements by Gasparov et al. [60]) are also plotted for comparison. The conductivity increases promptly at 0 ps and rapidly decreases back to equilibrium, as expected from the time domain traces of figure 5.6.

The dependence of the conductivity on time and pump intensity may be further investigated by examining the mean THz response, given by $\sigma_1(1\,\mathrm{THz})$; these behaviours are plotted

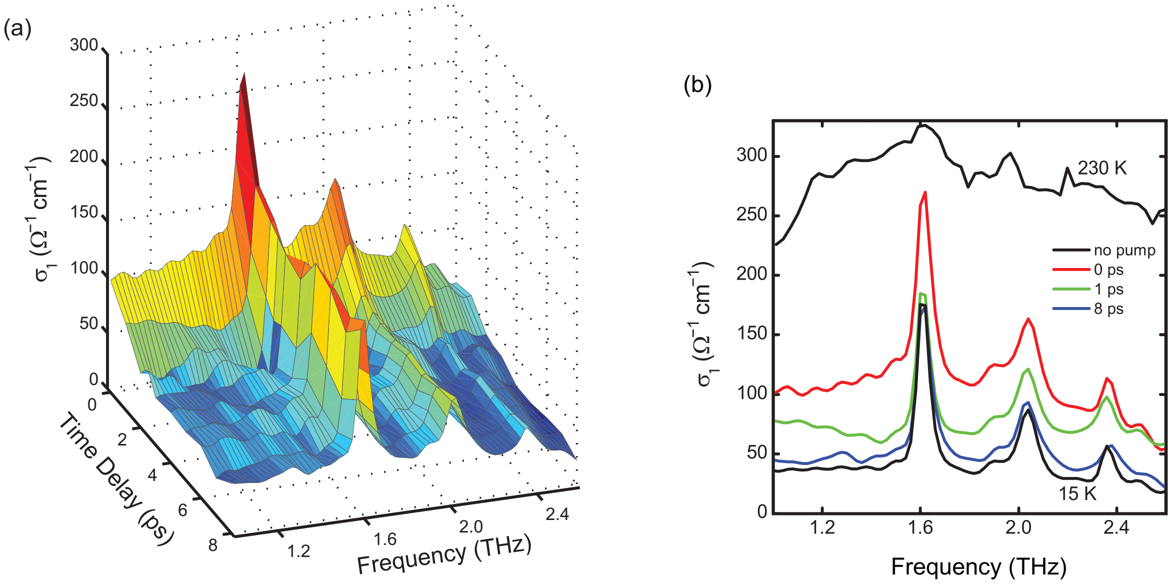

Figure 5.7: (a) Photoinduced conductivity $\sigma_1(\omega, \tau)$ for different pump-probe delays τ after excitation with a $550\,\mu\text{J}\,\text{cm}^{-2}$ pump pulse. (b) Comparison of the photoinduced phase conductivity (coloured lines) with the thermal phase conductivity (black lines). High temperature data are courtesy of [60]

in 5.8. Figure 5.8(a) shows the temporal evolution of $\sigma_1(1\,\text{THz})$, which matches the pump trace of figure 5.6(c). The prompt increase and exponential decay reflect the loss and recovery of the Mott gap observed in photoemission experiments by Perfetti et al. [28]. The recovery time constant of 1.3 ± 0.2 ps is also close to the figure they reported. As the gap begins to melt, there is an increase in conductivity as insulating behaviour is lost and spectral weight shifts across the Fermi energy. However, the photoinduced change in σ_1 is significantly smaller than that observed upon heating. This can be seen clearly in figure 5.7(b), where the conductivity immediately above the thermal insulator–metal transition at 230 K can be compared to the conductivity after the photoinduced insulator–metal transition at 0 ps.

Figure 5.8(b) plots the intensity dependence of the photoinduced conductivity immediately after excitation, which increases continuously with pump fluence. Additionally, the phonon modes remain prominent, with little or no screening after excitation or as the fluence is increased.

These observations are all inconsistent with the temperature-dependent behaviour of TaS_2. As the temperature is raised, σ_1 is essentially unchanged until the transition at 220 K [53,

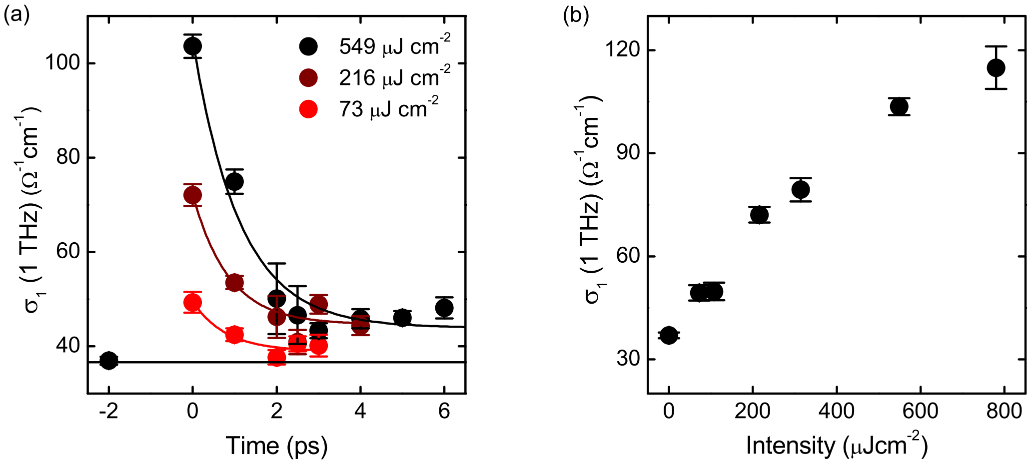

Figure 5.8: (a) Temporal behaviour of $\sigma_1(1\,\mathrm{THz})$ for different pump intensities. (b) Intensity dependence of $\sigma_1(1\,\mathrm{THz})$ at 0 ps time delay.

60]. After the thermal transition, there is also almost complete screening of the phonons. These discrepancies indicate that the photoinduced metallic state has qualitatively different transport properties to those observed in the thermal metallic state.

Further insight into the properties of the photoinduced phase can be gained by a closer examination of the phonon lineshapes. Figure 5.9 shows the complex conductivity around the 1.6 THz phonon resonance at various time delays. The lineshapes of the equilibrium insulating phase can be accurately represented by symmetric Lorentzian profiles, as described in section 5.3.2. However, those of the photoinduced metallic phase develop a pronounced asymmetry, which varies in time. The real part σ_1 exhibits a clear shift of spectral weight from the low- to the high-energy side of the mode, with a dip developing below the central frequency. Simultaneously, the imaginary part σ_2 flattens on the high-energy side. A similar effect, though of smaller magnitude, is seen in the other two modes within the measurement bandwidth.

These asymmetries are an example of the Fano effect, a general spectroscopic feature which arises from coupling between a discrete resonance and a continuum of excitations [126]. This effect was discussed in more detail in section 5.2. There, it was shown that the coupling produces interference around the resonance, leading to a complex conductivity characterised by an asymmetry parameter q. The optical conductivity is then modified from the Drude-

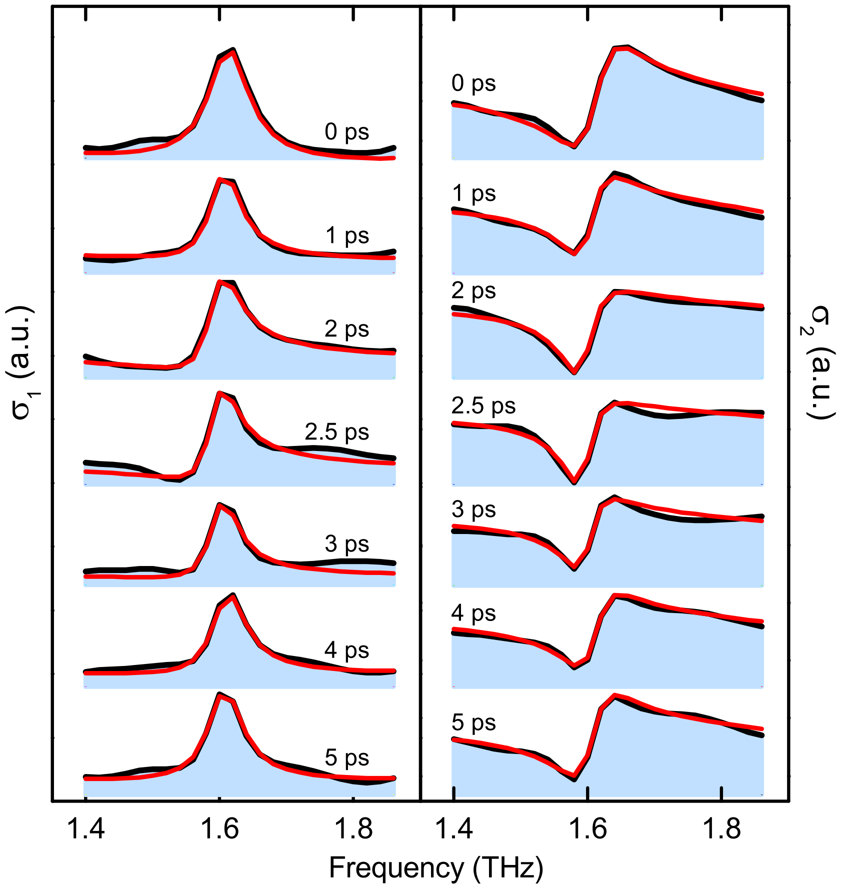

Figure 5.9: Temporal evolution of the 1.6 THz mode after excitation with a 550 µJ cm^{-2} pump pulse, showing both real (left) and imaginary (right) parts of the conductivity (black lines). Red lines are fits to the data using a Fano lineshape.

Lorentz model of equation (5.11) to become

$$\sigma(\omega) = \frac{\sigma_0}{1 - i\omega\tau} + i\varepsilon_0\omega\,(1 - \varepsilon_\infty) + \sum_{j=1}^{n} i\sigma_{0,j}\frac{(q_j - i)^2}{\left(i + \frac{\omega^2 - \omega_j^2}{\gamma_j \omega}\right)}\,. \tag{5.13}$$

The only change is to the final term, which replaces the Lorentzian shapes with Fano resonances. Here, j labels the phonon lineshapes, each of which has frequency and linewidth given by ω_j and γ_j, respectively, as well as an asymmetry parameter q_j (larger $1/q$ denotes a more asymmetric profile). The strength of the mode is given by $\sigma_{0,j} = \omega_{p,j}^2/(\gamma_j q_j^2)$.

Equation (5.13) was fit to the experimentally derived complex optical conductivity, using three terms in the summation to represent the three phonons at 1.61, 2.04, and 2.36 THz. The red lines in figure 5.9 show the fits obtained for the lowest frequency mode at 550 µJ cm^{-2} as

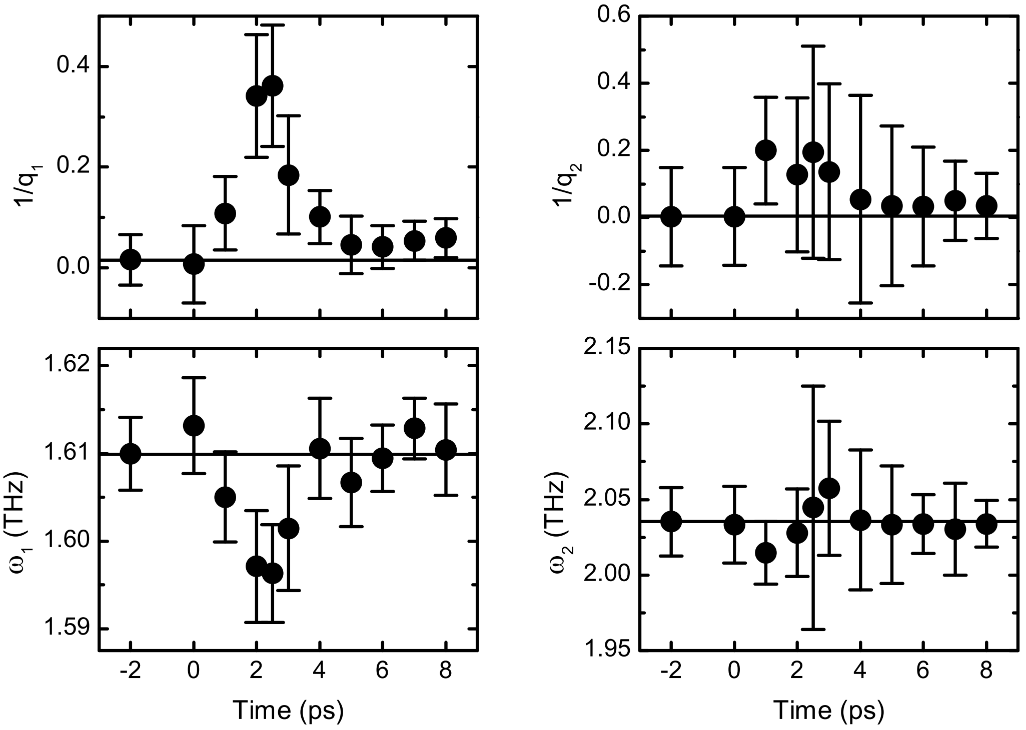

Figure 5.10: Time-dependent asymmetry parameter $1/q$ and renormalised mode frequency ω for the 1.61 THz (left) and 2.04 THz (right) phonon modes. Horizontal black lines mark the equilibrium parameters.

a function of pump-probe time delay. There is good agreement between the fit and the data.

The time-dependent asymmetry parameter $1/q_j$ and the renormalised mode frequency ω_j are plotted in figure 5.10 for the phonons at 1.61 and 2.04 THz. As expected from figure 5.9, there is a pronounced change in $1/q$ in the 1.61 THz mode after photoexcitation, as well as a shift in the phonon frequency. The delayed onset of the effect is expected to be due to anharmonic coupling from higher energy processes which are perturbed by the laser first, such as electron-electron scattering. The asymmetry parameter in this mode decays exponentially with a time constant of 0.9 ± 0.3 ps, which is similar to the temporal dependence of $\sigma_1(1\mathrm{THz})$ and to the recovery of the Mott gap. Furthermore, the positive sign of $1/q$ shows that the phonons are interacting with a continuum centred at higher energy [126, 132]. The most likely candidate for this is the new states appearing as the Mott gap begins to melt.

The existence of the transient Fano parameter suggests that the electron-phonon interaction is changing in time as the photoinduced insulator–metal transition takes place. The shift in the central frequency of the mode is further evidence of this, since measurements of the discrete state in presence of the Fano effect are modulated by the discrete–continuum coupling, shifting the apparent energy of the unperturbed state. The fit therefore suggests that the electron-phonon interaction is strongly altered in the photoexcited phase.

As a final comment on the fit parameters, it should be noted that the changes to the fit parameters for the second mode in figure 5.10, while noisier than for the lower frequency mode, still show similar behaviour, albeit on a smaller scale. It is difficult to resolve clear changes in the third mode at 2.36 THz, though there appears to be a shift in ω_3; this may be due to a combination of its position near the edge of the measurement bandwidth and its smaller strength, making it noisier than the other modes.

Summarising the results of the THz spectroscopy measurements, the low-energy transport properties of the photoinduced phase of TaS_2 begin to emerge. A prompt increase in conductivity is observed, which scales with pump intensity. This correlates well with the known collapse of the Mott gap from photoemission experiments. The phonon modes remain largely unscreened and acquire asymmetries which evolve in time, suggesting important changes to the electron-phonon interaction. The picture developing is one of a transient metallic state having markedly different properties to the thermal one. More insight into the electrodynamics of this phase can be gained by studying its properties at higher energy, which is where the discussion will shift to now.

5.4 Infrared Experiments

5.4.1 Experimental setup

The THz experiments are unique in their ability to record both amplitude and phase information, allowing for a reconstruction of the low-frequency optical properties of the sample. However, their bandwidth is limited to frequencies below 3 THz. While much useful information can be gained here, especially regarding the near-DC conductivity, it is also constructive to look at higher frequencies to see how other features are changing. This must be done using more standard reflectance measurements, which only record intensity changes. Nonetheless, they can provide invaluable information on the dynamics of the system.

To this end, a second series of measurements was carried out on TaS_2 to probe the response

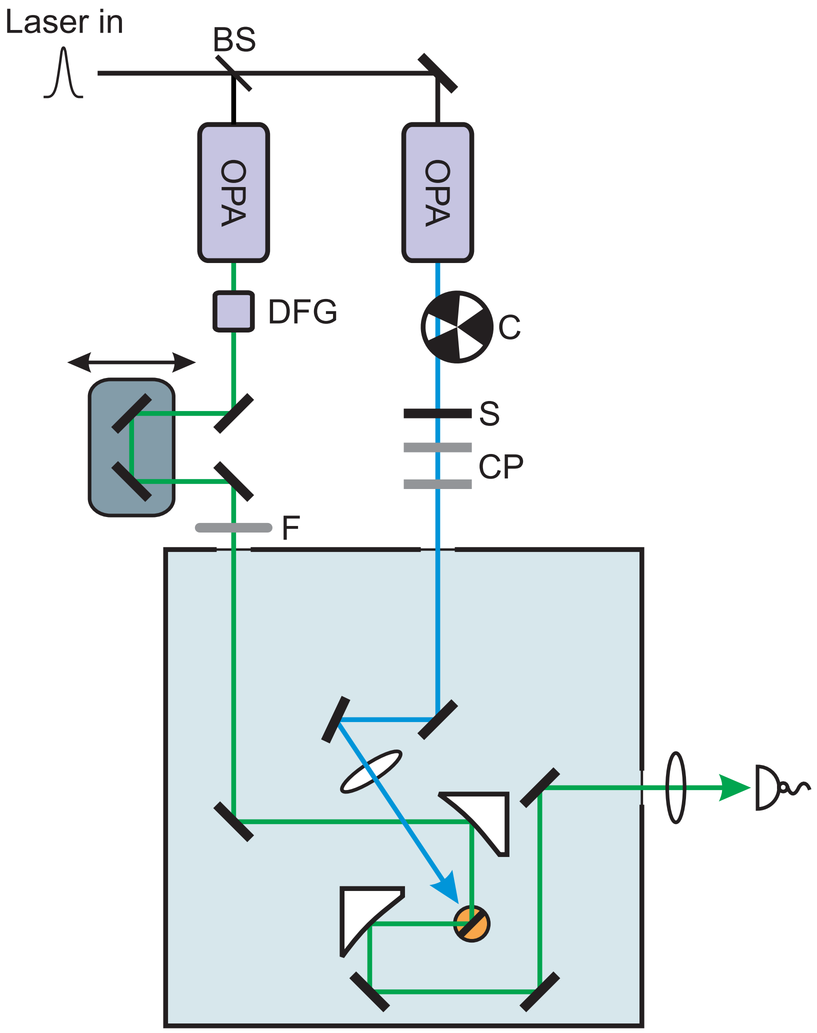

Figure 5.11: Experimental layout for the infrared pump-probe measurements. BS – beam splitter. DFG – difference frequency generation stage. F – filter. S – silicon. CP – crossed polarisers. C – chopper wheel. The orange circle represents the cryostat cold finger with the sample (black line) mounted on top. The light blue box represents the vacuum chamber and the grey-blue box is a delay stage.

to photo-doping from the mid-IR to the visible regions of the spectrum. The experimental setup, which shares much of the apparatus of the THz experiments, is sketched in figure 5.11. The laser was the same 1 kHz 800 nm amplified source as before. Also as in the previous set of experiments, an OPA was used to generate pump light at 1.3 µm (0.95 eV), whose intensity was controlled with a pair of crossed polarisers. Silicon was used to filter out the parasitic visible light. Again, the signals obtained showed no dependence on the pump polarisation. The vacuum chamber/cryostat combination from the THz measurements was used again here in order to maintain the same sample conditions as before, as well as to prevent any potential problems with cryostat window materials and apertures when using different probing wavelengths.

This time, the probe source came from a second OPA, identical to the first although with a lower output power. A difference frequency generation (DFG) stage, consisting of an angle-tunable GaSe crystal, could be mounted to the output of the OPA to extend its range from the near-IR down to $\approx$ 20 µm. A Michelson interferometer could be inserted into the beam path to verify the infrared wavelength, as described in section 3.2.4. A 50 µm thick polypropylene film was used as a window for the probe beam, as it is transparent over a broad spectral range and thin enough to cause only minimal dispersion and distortion of the beam.

In order to detect the correct probe wavelengths, a variety of detectors and filters (labelled F in figure 5.11) were employed with sensitivity in different spectral regions. In order to block out stray pump light at 1.3 µm, a germanium wafer was placed in front of all the detector types. In the near-IR around 2 µm, silicon and germanium wafers were used as filters to remove undesirable shorter wavelengths produced in the OPA, and an amplified InGaAs diode was used to detect them after the sample.

For wavelengths longer than 2.7 µm, the DFG stage needed to be used. This generated longer wavelengths through collinear mixing of the signal and idler outputs of the OPA. As such, it was necessary to remove the more intense near-IR components co-propagating with the weaker mid-IR light. In addition to the silicon and germanium wafers, a 2.5-mm-thick plate of indium arsenide was used as a long-pass filter for wavelengths longer than 3.6 µm. For wavelengths longer than 10 µm, an additional interference filter, consisting of stacks of lead telluride and zinc selenide on a germanium substrate, was used. The mid-IR wavelengths were detected using liquid-nitrogen-cooled HgCdTe detectors. Their sensitivity could be adjusted

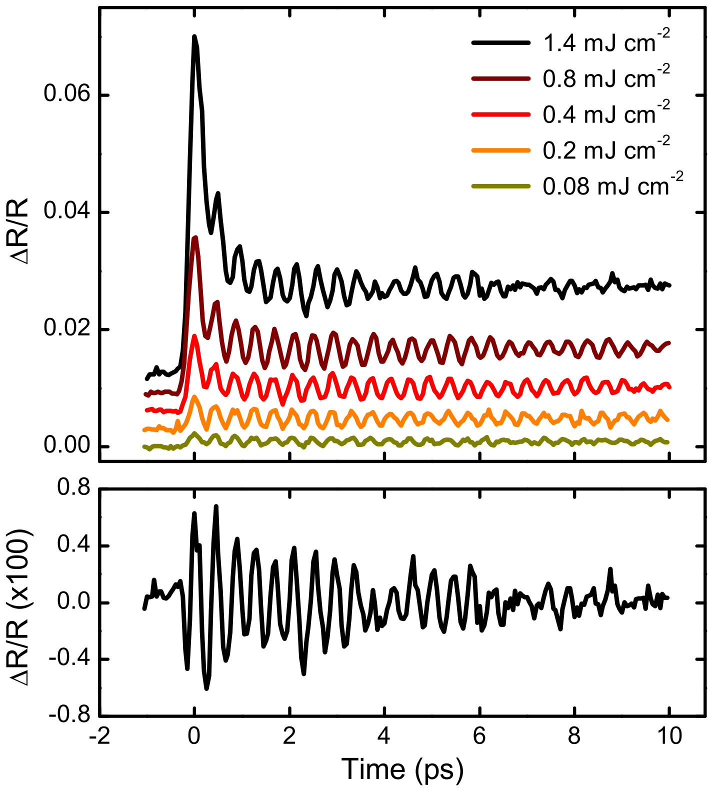

Figure 5.12: Top: pump-induced changes in reflectance for TaS$_2$ at 15 K for different pump intensities. Bottom: coherent oscillations after subtraction of the incoherent background.

between 5 and 18 µm by replacing the sapphire window with zinc selenide.

Visible wavelengths were generated from the OPA output by second-harmonic generation in a BBO crystal. Blue coloured glass was then used to filter out the infrared light, and a silicon diode was used as a detector.

The pump was chopped with a mechanical copper wheel (C in figure 5.11) and changes to the probe at the chopper frequency were measured by lock-in detection. The reflectance was measured as a function of time from 84 meV, just below the 100 meV Mott gap, up to 1.9 eV. The pump intensity was varied to coincide with the THz measurements.

5.4.2 Near-infrared response

The reflectance changes at 2 µm wavelength (0.62 eV photon energy) were measured as a function of pump-probe time delay. The results for different pump intensities are shown in figure 5.12. All the signals show a sharp increase in the conductivity on arrival of the pump,

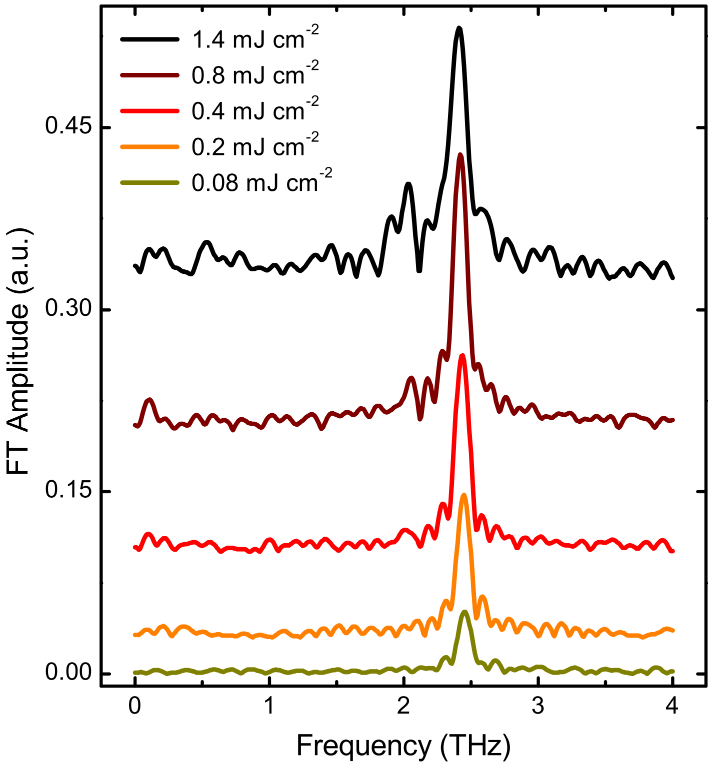

Figure 5.13: Fourier transforms of the coherent oscillations in $\Delta R(t)/R$ for different pump intensities.

followed by decay to a long-lived quasi-equilibrium. Superimposed on this are large-amplitude coherent oscillations. As the pump intensity increases, the peak and offset of the signal grow in size. The amplitude of the coherent oscillations also increases, though they appear to dampen faster. Additionally, at high intensities there is a beating, indicative of the appearance of a second frequency close to the first. This is more apparent after subtracting the incoherent background, as shown in the bottom panel of figure 5.12.

The Fourier transforms of these oscillations are given in figure 5.13. The dominant frequency is at approximately 2.4 THz. This corresponds to the A_g mode reported by Sugai et al. [33] and attributed to the charge density wave (CDW) amplitude mode [33, 61]. Their appearance in pump-probe experiments was first observed by Demsar et al. [35], and they are thought to arise from coherent excitation of the amplitude mode [35, 69]. As the pump intensity is increased this mode grows in population and a slight red-shift in frequency can be observed. At an intensity of around $1\,\mathrm{mJ\,cm^{-2}}$, a second frequency component emerges close to 2 THz. This mode was assigned as an E_g mode [33] and has been observed in time-resolved

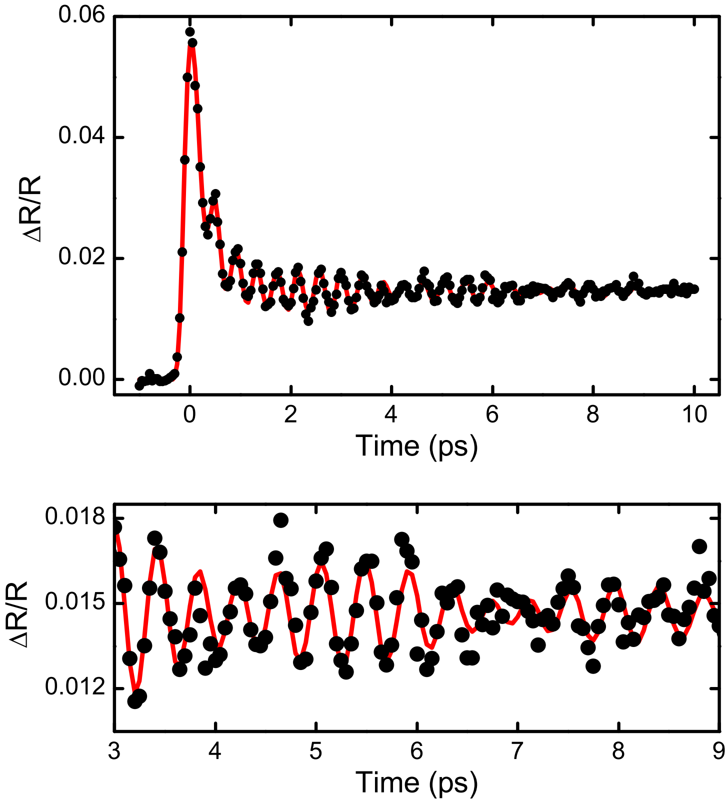

Figure 5.14: Fit (red line) to the data (black dots) at 0.62 eV after excitation with a pump intensity of 1.4 mJ cm^{-2}. The bottom panel shows a close up of later times.

studies by Toda et al. [69].

In order to analyse the data in more detail, the reflectance changes for different intensities were fitted with the following function:

$$\frac{\Delta R(t)}{R} = \mathrm{erf}(t)\left\{\sum_{j=1,2} A_j e^{-t/\tau_j}\cos\left(\omega_j t + \phi_j\right) + S e^{-t/\tau_S} + D\right\}. \tag{5.14}$$

Here, $\mathrm{erf}(t) = \frac{1}{2} - \frac{1}{\sqrt{\pi}}\int_0^{t'} \exp(-t^2/\Delta t^2)dt'$ represents the error function, which describes the rising edge of the signal as the integral of a Gaussian function of width Δt. The oscillatory response is modelled by a cosine of frequency ω_j and initial amplitude A_j, which decays exponentially with time constant τ_j. The next term describes the single-particle incoherent contribution, which has amplitude S and decays with a time constant τ_S. The final term D gives the background signal due to processes with lifetimes longer than measured here.

The fit for the pump-probe trace at 1.4 mJ cm^{-2} is shown in figure 5.14. On the whole, the fit is good and is able to reproduce the data well. The inclusion of a second frequency component at $\approx 2.05\,\mathrm{THz}$ accurately recreates the beating effect seen at later times, as highlighted in the bottom panel of figure 5.14. The salient features from the fits to the $0.62\,\mathrm{eV}$ data are shown in figure 5.15. The information pertaining to the second mode, with a frequency of $2.05\,\mathrm{THz}$, has been omitted since this mode is only apparent at high intensities and so is hard to fit across the full intensity range.

The data are all well represented by a cosine function, with no additional phase shift required. This confirms the displacive excitation mechanism as the origin for the oscillations (see section 3.4.2 for more details). At all intensities, the rise time corresponds to the pump-probe cross-correlation time of $\approx 300\,\mathrm{fs}$ FWHM, which was independently measured at the sample position by sum-frequency generation between the pump and probe in BBO (as described in section 3.2.5). This means that the onset of the transition is prompt compared to the pump-probe cross-correlation, as expected; indeed, the Mott gap collapse was measured by Perfetti et al. to occur on a timescale faster than $50\,\mathrm{fs}$ [28].

The decay time of the single particle response τ_S, given in figure 5.15(b), shows a linear dependence on the intensity, as does the background D in figure 5.15(d). This simply suggests that as more electrons are excited, they take longer to thermalise and this depends only on the number of electrons or photons.

Interestingly, the peak of the response S in figure 5.15(d) behaves super-linearly, though over the investigated intensity range no saturation is seen. At higher intensities it may be possible to observe such effects, which would suggest that the photoinduced Mott-insulator–metal phase transition is becoming saturated as more of the pumped volume is excited. Increasing the number of pump photons excites more electrons and the Mott gap begins to melt more fully. Eventually, the gap should collapse completely, in which case increasing the photon number cannot change the response any further.

Finally, the coherent oscillations also show interesting nonlinear behaviour in the photoinduced phase. Figures 5.15(a) to (c) give the frequency, decay time, and amplitude of the CDW amplitude mode oscillations, respectively. The mode is found to show a pronounced red-shift and is increasingly damped as the intensity rises. This damping can arise simply due to screening effects from the hot electrons. The background D indicates a linear increase in photoexcited carriers, which could then be the cause of the screening and subsequent damping of the phonon modes.

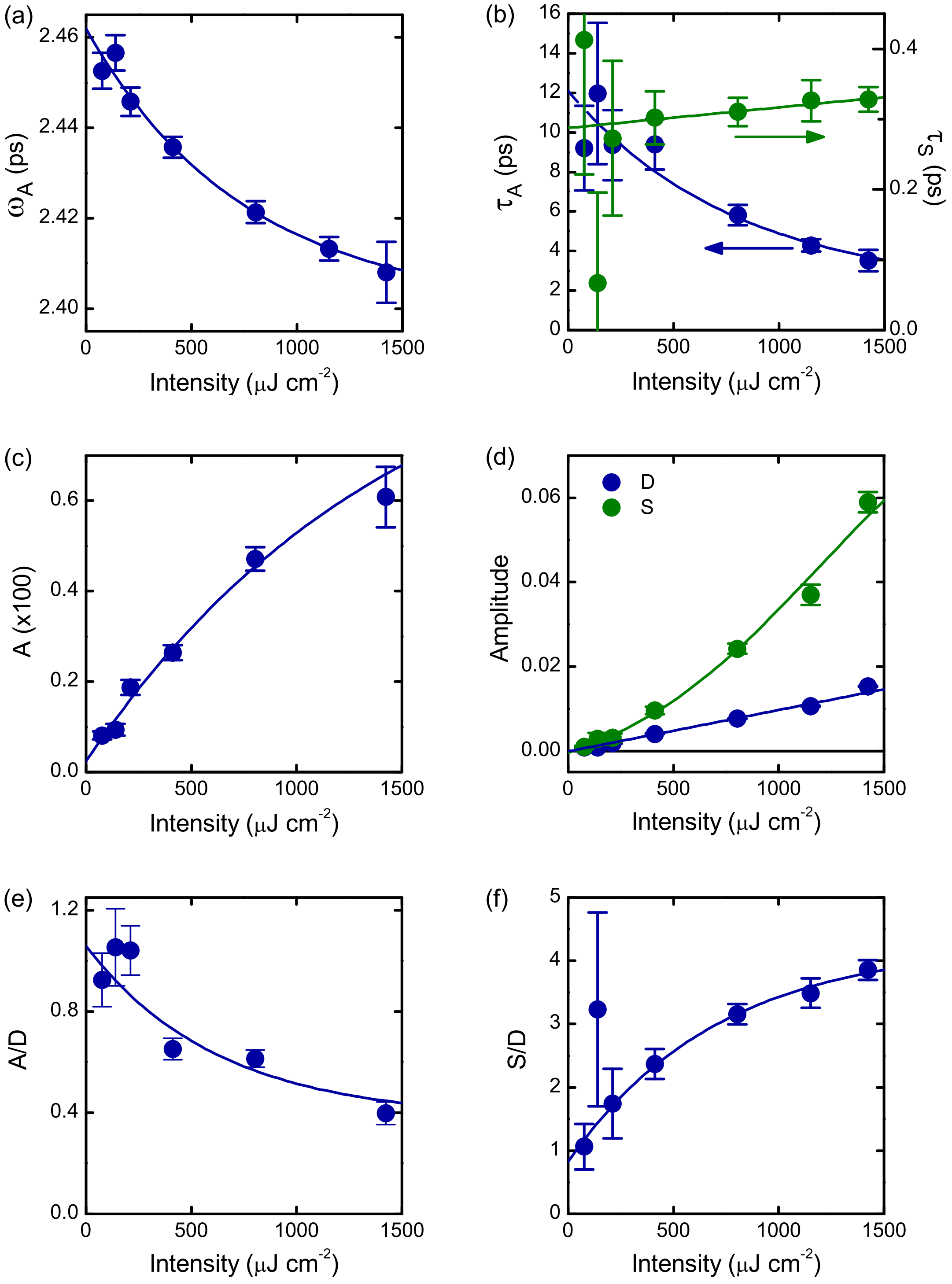

Figure 5.15: Intensity dependence of the fit coefficients at 0.62 eV probe energy. (a) Frequency, (b) decay time (blue dots), and (c) amplitude of the CDW amplitude mode oscillations; (b) also shows the decay time for the incoherent response (green dots). (d) Amplitude of incoherent response (S) and background (D). The ratio of amplitude mode and incoherent response to the background are shown in (e) and (f), respectively. Lines are guides to the eye.

Additionally, phonons can become damped through inelastic phonon scattering, which arises from anharmonic crystal field effects. Such effects give rise to red-shifting of the mode frequency as the amplitude of oscillation increases; both the frequency shift and increase in amplitude may be observed here in figures 5.15(a) and (c). The Mott gap has recovered within around 1 ps, and this prevents electronic excitations of energy less than the gap size, so less than 100 meV. Therefore, the only damping mechanism for the amplitude mode is expected to be anharmonic decay through other phonon modes.

The thermal behaviour of the collective excitations in TaS_2 was studied by Demsar et al. [35]. Using pump-probe techniques, they studied the response of the CDW amplitude mode as the temperature was raised through the insulator–metal phase transition at T_c. By comparing the measurements of this section with those of Demsar et al., further differences between the photo- and thermally-induced phases become apparent.

Firstly, it was found that the amplitude mode frequency red-shifted with lattice temperature until it reached T_c, at which point a sharp drop occurred. Concomitantly, the damping Γ shows a sudden increase at the same temperature, with the oscillations dying out within the first two or three picoseconds just above the transition temperature. Equivalent behaviour was reported in photoemission experiments [37]. These features occur as TaS_2 undergoes a first-order phase transition from the commensurate to quasi-commensurate phases. The quasi-commensurate phase is characterised by domains of commensurate CDW interspersed by incommensurate regions, resulting in a lack of long-range ordering and an incomplete lock-in of the CDW to the lattice. The rapid dephasing of coherent oscillations in the thermal metallic phase may then be thought of as arising from this lack of distinct CDW commensuration, which prevents the amplitude mode frequency from being clearly defined.

In the case of the photoinduced transition, as the pump intensity is increased there are only continuous changes to ω and Γ, with no sharp features. This recalls the change in conductivity found in section 5.3.3, which also showed only continuous growth. The existence of long-lived oscillations even at intensities as high as $1.4\,\mathrm{mJ\,cm^{-2}}$ implies that the transient phase retains the symmetry of the low-temperature phase and does not lose the commensuration of the CDW exhibited by the high-temperature phase. Thus photoexcitation relaxes the structural distortion, softening the modes as in the thermal case, but it is not capable of removing the CDW ordering or its commensuration. This further substantiates the view that the Mott gap

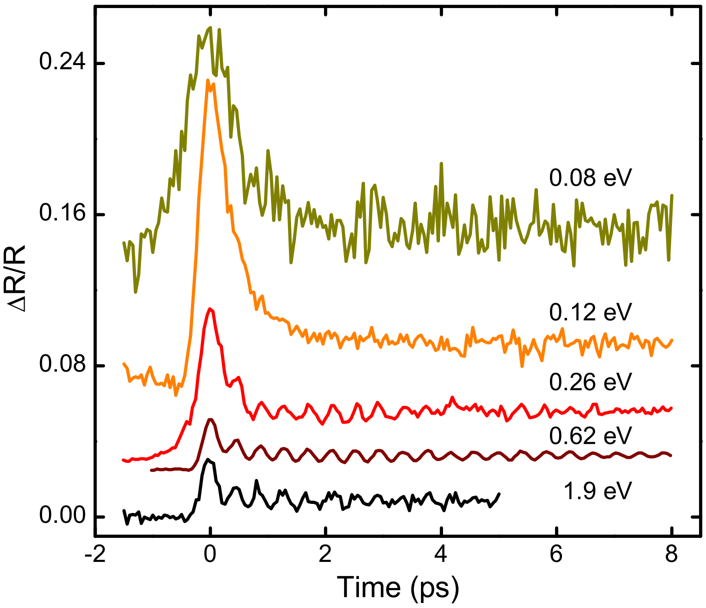

Figure 5.16: Pump-probe traces for different probe photon energies, all for pump intensities of approximately 750 µJ cm^{-2}.

approaches melting independently of the CDW distortions, which are only weakly perturbed, as proposed in other measurements [28, 71].

5.4.3 Broadband infrared response

The reflectance changes at 0.62 eV reveal a lot about the collective and single particle dynamics at high energies. However, as mentioned in section 5.4.1, the reflectance was not just measured at a single probe energy, but from the visible to the mid-IR regions of the spectrum, providing a broad energy range to further characterise the photoinduced dynamics of TaS$_2$.

The reflectance changes in time $\Delta R(t)/R$ after excitation with a pump centred at 0.95 meV (1.3 µm) were thus measured as a function of probe energy and pump intensity. Figure 5.16 shows example traces for similar pump intensities but for each of the probing wavelengths. Qualitatively similar behaviour to that at 0.62 eV is observed. As such, the changes at all probe energies and intensities were fitted with equation (5.14); the resulting fit coefficients are summarised in figure 5.17. Crucially, the reflectance changes show a dependence on probe energy as well as pump intensity. As is clear from both figures 5.16 and 5.17, the oscillations begin to disappear and their lifetime apparently decreases as the probe energy is lowered.

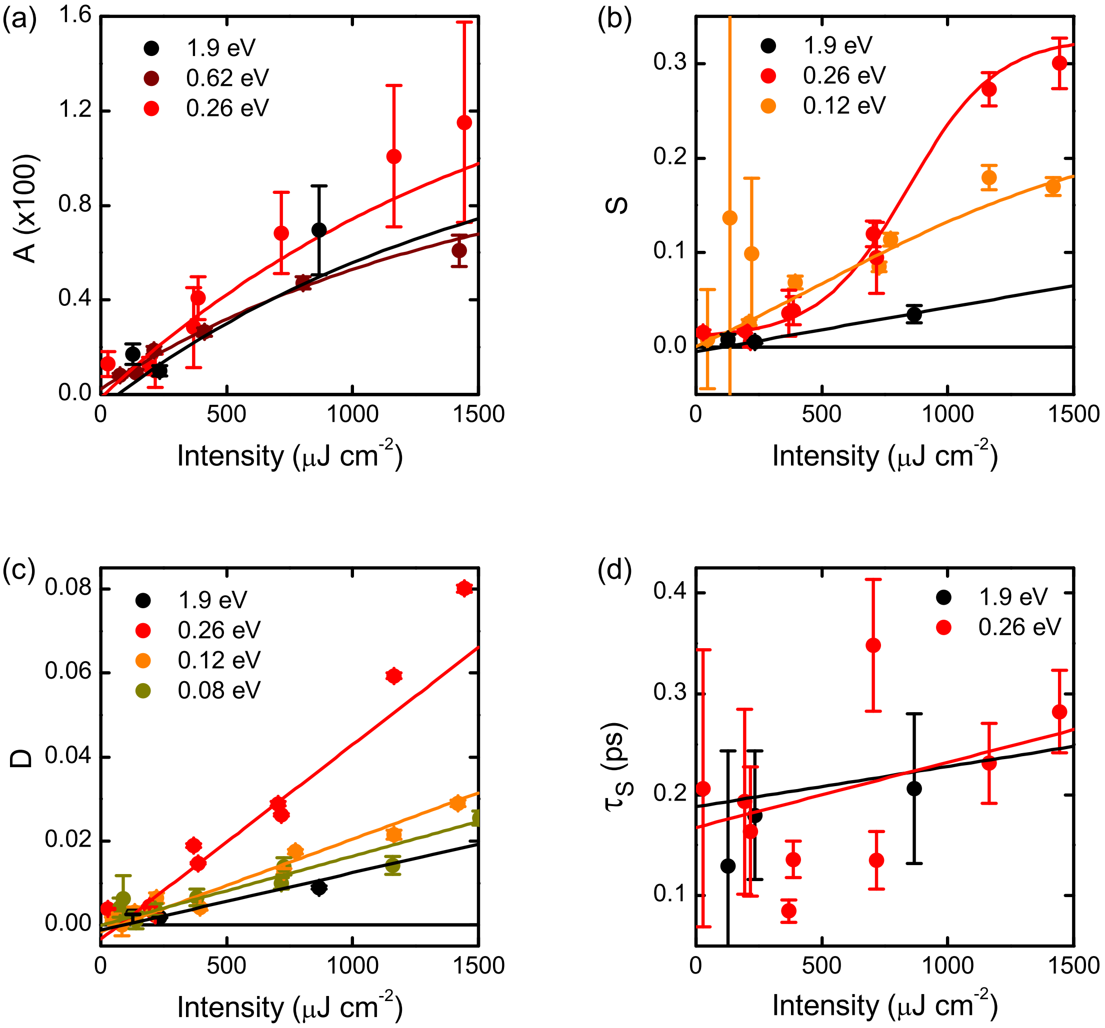

Figure 5.17: Intensity dependence of the fit coefficients at all probe energies. (a) Amplitude of the CDW amplitude mode oscillations A. (b) Amplitude of the incoherent response S. (c) Amplitude of the background D. (d) Decay time of the incoherent response τ_S. Lines are guides to the eye.

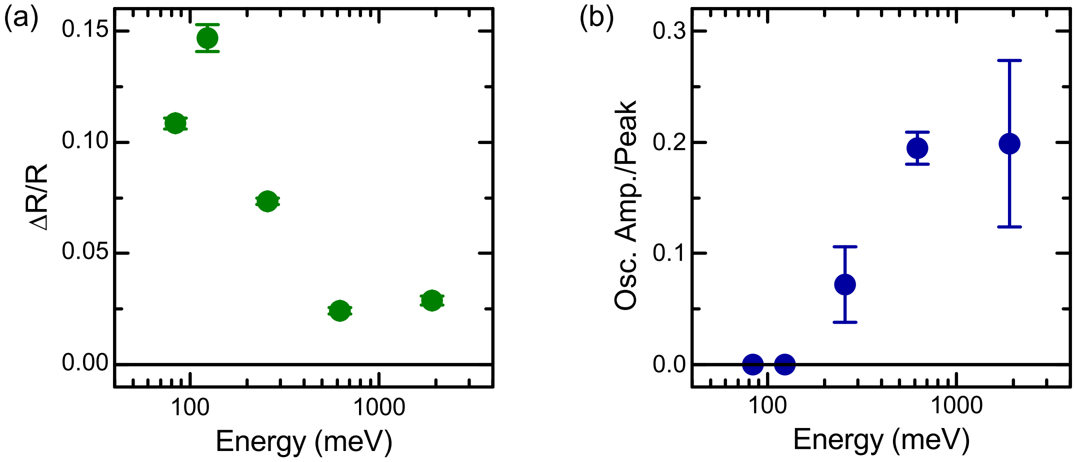

Figure 5.18: Peak reflectance changes at 0 ps as a function of probe energy for a pump intensity of approximately 750 µJ cm^{-2}. (a) Peak reflectance changes $\Delta R(0\,\mathrm{ps})/R$. (b) Ratio of oscillation amplitude to $\Delta R(0\,\mathrm{ps})/R$.

Additionally, the magnitude of the peak and long-lived reflectance changes varies with the probe energy, as shown in figures 5.17(b) and (c).

One explanation for the changes in the amplitude mode behaviour could be that the probe pulses are getting progressively longer, and subsequently the effect of the coherent phonons is averaged out over successive periods of oscillation. However, the pump-probe cross-correlation remains at about the same width for all probing energies, and is always less than the period of the amplitude mode ($1/\omega_A = 1/2.44\,\mathrm{THz} \approx 410\,\mathrm{fs}$). Hence any variation in the oscillations is expected to be connected to material properties at different energies. The absorption coefficient changes over the probed region, with the probe penetration depth becoming longer than that of the pump as the energy gets lower. As a result, the probe sensitivity to the coherently excited phonons in the photoexcited surface layer decreases with photon energy, shortening their apparent lifetime.

The dependence of reflectance on probe energy is illustrated more clearly in figure 5.18, where the peak reflectance changes, $\Delta R/R$ at $t = 0\,\mathrm{ps}$, and the ratio of the oscillation amplitude to peak $\Delta R/R$ are plotted for a single pump intensity as a function of probe energy. As the probe energy is lowered towards the gap (of size $\Delta = 100\,\mathrm{meV}$), $\Delta R/R$ increases dramatically due to the shift of spectral weight across the Fermi energy into the previously gapped region [28]. There is a peak in the changes close to and just above the gap energy.

Conversely, the coherent lattice vibrations influence the optical response progressively less. This suggests that the structural distortions are only weakly connected to the low-frequency electrodynamics. As discussed when looking at the response at 0.62 eV in section 5.4.2, the loss of the Mott gap appears to be independent from the coherent CDW distortions. The evidence from the rest of the infrared region supports this proposition.

Furthermore, there is the emergence of a large feature in the reflectance changes of figure 5.18(a) upon collapse of the gap. This feature plays a potentially important role in the transport properties of the photoinduced phase, which will be discussed in the next section of this chapter.

5.5 Evidence for Polaronic Conductivity

5.5.1 Polarons

An electron moving in the conduction band of a polar crystal is continuously influenced by the lattice polarisation field; at the same time, the presence of the electron influences the polarisation of the lattice. The Coulomb force of the electron attracts and repels nearby ions, producing a localised distortion of the lattice, as indicated in figure 5.19. This distorted polarisation then acts on the electron to lower its energy. As the electron moves through the lattice, it carries the distortion along with it, and this combination of an electron and its self-induced polarisation field, in the form of a phonon ‘cloud’, can be considered as a new quasiparticle called a polaron [142, 143]. The effective mass of the polaron is larger than that of the bare electron, since the electron must drag the distortion around with it, whilst at the same time the energy of the combined state is lowered by their mutual interaction.

The idea for the polaron first arose when Landau discussed self-trapping of electrons in NaCl [144]. The concept was later solidified by Pekar, who calculated polaron eigenstates in the limit of strong electron-lattice coupling, wherein a stationary polaron may be described by a localised electron moving in its own polarisation field [145]. In its simplest form, the polaron exists as a model for the interaction between a particle (here an electron) and a quantum field (the polarisation field of the lattice in the present case); as such, it enabled the first application of quantum field theory to solid state physics, initially approached by Frölich et al. [146].

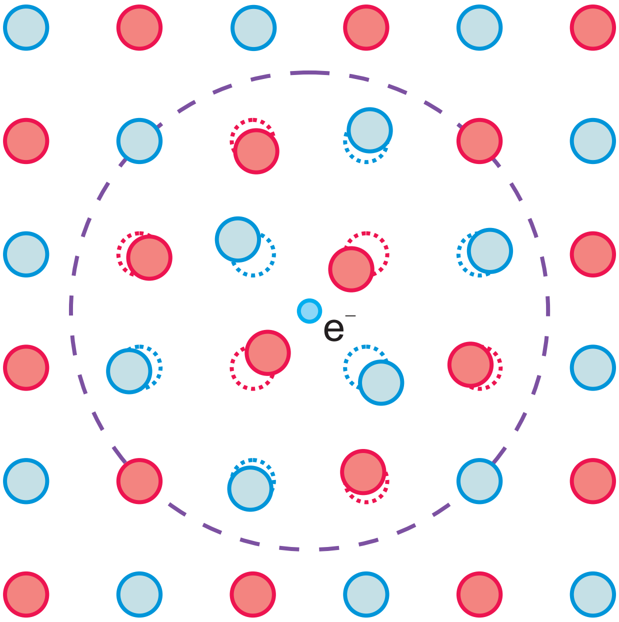

Figure 5.19: Diagrammatic representation of a polaron. A free electron (in the centre of the figure) moves through a lattice, producing a local distortion around it. Positive (red) ions are attracted, whilst negative (blue) ones are repelled. The polaron radius is indicated by the dashed line.

A polaron has a size determined by the extent of the lattice distortion created by the electron, as indicated schematically by the dashed line in figure 5.19. When the polaron radius is larger than the unit cell, it is called a large, or Frölich, polaron [146, 147]. In this case, the lattice can be treated as a continuum. When the polaron radius becomes comparable to the lattice constant, so that the distortion is limited to the immediate vicinity of the electron, the quasiparticle is called a small, or Holstein, polaron [148, 149]. Here, the discrete nature of the lattice must be considered. The effect of small polarons leads to self-trapping of electrons and their transport becomes characterised by hopping between lattice sites.

The properties of polarons depend heavily on the strength of the electron-lattice interaction, and the two types of polaron present two limiting cases of this coupling. Small polarons are expected when strong, short-range interactions dominate, whilst large polarons represent the case of weaker, more long-range interactions. Due to the inherent confinement properties of low-dimensional materials, polarons are frequently important in understanding the transport properties of quasi-one- or two-dimensional systems [150–152]. Furthermore, polarons have been observed in low-dimensional charge-density-wave systems, where the strong electron-phonon coupling makes electrons susceptible to small polaron formation [153, 154].

In TaS_2, angle-resolved photoemission spectroscopy of the quasi-commensurate phase by Clerc et al. [36, 57] revealed anomalous spectral properties, including broadened lineshapes and the absence of an expected quasiparticle peak crossing the Fermi level. Polaronic effects were proposed as a possible mechanism to explain these properties. The static deformation occurring upon star formation in the quasi-commensurate phase leads to enhanced electron-phonon coupling, with the stars acting as small molecules favouring short-range interaction. Clerc et al. invoked these molecules as centres for small polarons and considered an interplay between long- and short-range electron-phonon interactions, leading to enhancement of the coupling. However, their methods could not directly confirm the existence of polarons, and no additional information is available to confirm or reject this view in the equilibrium phases of TaS_2.

5.5.2 Polaronic conductivity in the photoinduced phase of TaS_2

The photoinduced phase in TaS_2 explored in this chapter has provided a broadband view of the changes to the optical properties occurring after photoexcitation. Figure 5.20(a) summarises the photoinduced reflectance changes across the full frequency range investigated. Also shown in this figure is the equilibrium reflectance below and immediately above the thermal phase transition at $T_c = 220\,\mathrm{K}$.

In the THz range the raw ΔR signal is small ($\ll 1\%$) due to the large difference between the pump and probe penetration depths. As outlined in section 5.3.3, this mismatch allowed for the use of a thin-film model to extract the optical conductivity from the measured changes in the THz electric field. Conversely, in the mid-IR region, where the extinction coefficients are somewhat better matched, a pronounced increase in reflectance is clearly visible already in the unprocessed data.

At high photon energies, only the intensity of the pulses could be measured, contrary to the THz region where the field could be directly recorded. Therefore, in order to extract the broadband time-dependent optical conductivity in absence of phase information at high photon energies, the following procedure was applied to the acquired data. First, the static broadband reflectance at 30 K (provided by Gasparov et al. [60]) was fitted by modelling the

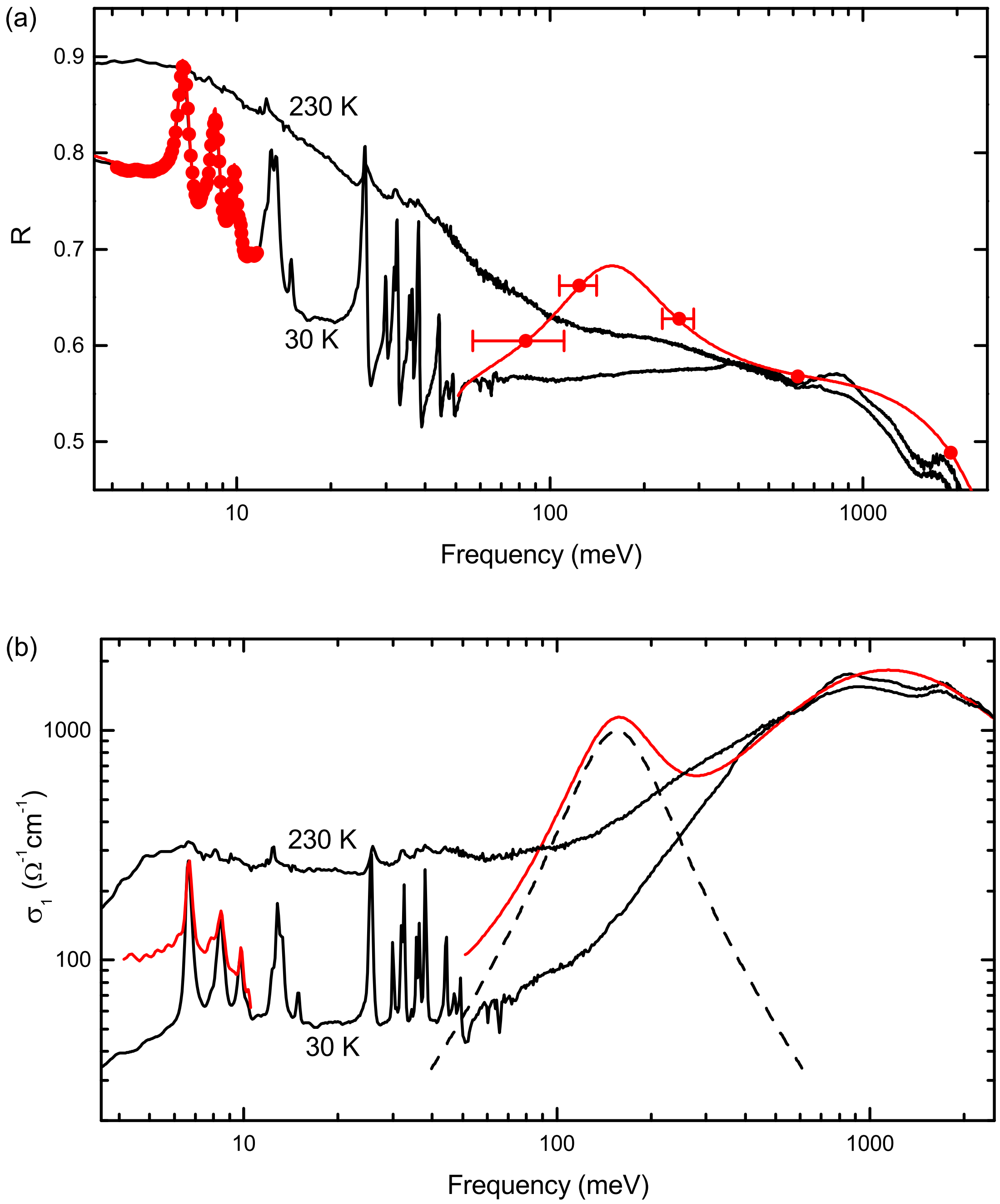

Figure 5.20: Comparison of the phases of TaS$_2$ at all measured frequencies. (a) Reflectance change immediately after photoexcitation (red dots). Horizontal errors bars give the FWHM of the probe pulse spectrum. The red line gives a fit to the data, as explained in the text. (b) Calculated conductivity immediately after photoexcitation (red line). The dashed line is the Lorentzian representing a polaron band. In both (a) and (b) the continuous black lines are the reflectance and conductivity, respectively, of the thermal phases, provided by [60].

equilibrium optical conductivity as a series of Lorentzian harmonic oscillators. This leads to a conductivity of the form of equation (5.11), namely

$$\sigma(\omega) = i\varepsilon_0\omega\left(1 - \varepsilon_\infty - \sum_{j=1}^{n} S_j \frac{\omega_{0j}^2}{\omega_{0j}^2 - \omega^2 - i\omega\gamma_j}\right), \tag{5.15}$$

where each Lorentzian oscillator accounts for a phonon or electronic transition band of frequency ω_{0j} and linewidth γ_j.

The fit procedure was carried out using the Asf for Windows (WAsf) program developed by Steffen Schultz at the University of Stuttgart [155]. This program calculates the dielectric function based on a number of different models, including the Drude or Lorentzian models, using user-defined inputs, such as plasma frequency and oscillator strength. It then generates other optical response functions, e.g. conductivity and reflectivity, from this using relations similar to those in section 4.3. This can be done for single or multiple layer systems. The models can be fit to different measurements of optical properties (reflectance, conductivity, etc.) simultaneously and all the output functions are Kramers-Kronig consistent.

For the data on TaS_2, the model chosen was a series of Lorentzian oscillators, as described above. One oscillator was chosen for each phonon mode. Additional Lorentzians were used to model the electronic transitions for the low-temperature conductivity around 1 eV and a Drude term was added for the background conductivity in the THz region. Fitting was carried out by adjusting the parameters for each oscillator to be consistent with the conductivity and reflectance data simultaneously.

The photoinduced changes in reflectance were then analysed by extending the two-layer model of section 5.3.3 across all frequencies. Thus the photoexcited region was treated as a uniform layer of 45 nm thickness, representing the pump penetration depth, sitting on top of an unperturbed bulk. Starting with the thin layer in the same state as the bulk, the reflectance changes could be modelled by applying shifts of spectral weight among the oscillators of the perturbed layer in the WAsf program. This reproduced the optical conductivity already obtained in the THz region and accounted for the near-IR reflectance changes. However, the mid-IR response required the addition of a new resonance centred at 155 ± 25 meV; it was not sufficient to use only the oscillators from the unperturbed state. This feature has no analogue in any of the thermal phases. Its position and uncertainty were obtained by adjusting its parameters by eye within the spectral resolution of the mid-IR points (indicated by the horizontal error bars in figure 5.20(a)) so that it still appeared acceptable with the sparse data available.

The broadband conductivity and reflectance of the photoinduced phase at 0 ps time delay, as determined by this procedure, are indicated by the red lines in figure 5.20. From all the data now discussed in this chapter, three features emerge as especially meaningful: reduced low-frequency conductivity compared to the high-temperature phase; Fano lineshapes for the phonons, indicative of strong electron-lattice coupling; and a transient mid-IR resonance, highlighted by the dashed line in figure 5.20(b). The appearance of mid-IR bands is characteristic of polaron formation, as observed in other strongly correlated materials [156–159], and the asymmetric reshaping in the phonon resonances emphasises strong coupling between electrons and the lattice coinciding with the emergence of this new feature.

From these combined observations, then, the key conclusion of this work is that transport in the photoinduced phase is polaronic. Microscopically, charges that in the ground state were localized by electron correlations are made mobile after photo-doping. However, electron-lattice coupling is still strong due to the presence of the CDW, and this imposes a dominant energy scale on their transport. These features belong to an exotic state of TaS$_2$ that is only accessible with photoexcitation.

5.6 Summary

This chapter has attempted to characterise the photoinduced metallic phase of TaS$_2$, using optical spectroscopy over a broad frequency range to measure its transport properties. Time-resolved THz time-domain spectroscopy is employed to directly retrieve the low-energy complex conductivity, while the high-energy reflectance is measured using time-resolved reflection spectroscopy techniques. These different frequency probes reveal much about different energy scales: long-range transport is revealed at low frequencies and the CDW behaviour may be elucidated at high frequencies.

The photoinduced phase is found to be qualitatively different from the thermal phase in a number of ways, and it is the combination of probes which allows for a full characterisation. Crucially, the transient metallic phase is one in which the Mott gap begins to melt, leading to an increase in conductivity at low frequencies, but the lattice retains its low-temperature symmetry, with the CDW distortion being only partially relaxed. The strong electron-lattice coupling, highlighted by the continued presence of the CDW after photoexcitation and the appearance of transient Fano effects, dominates the transport properties of the photoinduced phase. The data presented indicate the importance of polaronic transport in photo-doped TaS_2, descending directly from the separate influence that light has on electron correlations and on the lattice response.

A more detailed study of the properties of the polaron band could be achieved by acquiring pump-probe data at more frequencies across the infrared region. This would allow for a better spectral profile of the band to be built up, and would provide an understanding of its temporal evolution as the system relaxes back to equilibrium.

Broadband time-resolved optical spectroscopy has been employed with great success to study photoinduced effects in other complex materials [21, 160, 161]. It is proving to be an indispensable tool to understand the role of many interacting degrees of freedom in transient states of complex matter. By expanding the spectrum down into the THz and up into the ultraviolet and X-rays, the breadth of information about these competing elements will only increase. In the case of TaS_2 presented here, this dissection of the relative importance of electron and lattice contributions may point towards a better understanding of the formation of the Mott–CDW ground state in this intriguing material.

Chapter 6

Time- and Angle-Resolved Photoemission Spectroscopy of 1*T*-TaS$_2$

6.1 Angle-Resolved Photoemission Spectroscopy

Over the last few decades, angle-resolved photoemission spectroscopy (ARPES) has proven to be one of the most direct methods of studying the electronic structure of solids, with recent developments enabling for extremely high precision measurements of the energy and angular distribution of electrons. By providing detailed information on the shape and size of Fermi surfaces and electronic band structures, ARPES has afforded great insight into the behaviour of many strongly correlated materials, including Mott insulators [37, 162], low-dimensional materials [36, 163], and high-temperature superconductors [164, 165]. In essence, the spectrum measured by ARPES gives the one-electron spectral function of the material, offering a veritable smorgasbord of information on the single-particle excitations.

The term photoemission spectroscopy is applied to the myriad experimental techniques based on the photoelectric effect. Electrons in a solid may absorb photons and, if the photon energy is sufficiently high, escape from the surface with a kinetic energy

$$E_{\text{kin}} = h\nu - \Phi - |E_B|, \tag{6.1}$$

where $h\nu$ is the photon energy, Φ is the work function of the material, and E_B is the electron binding energy. Since the photon energy is known, the measured kinetic energy distribution of the electrons will reflect the energy distribution of the initial states they occupied in the

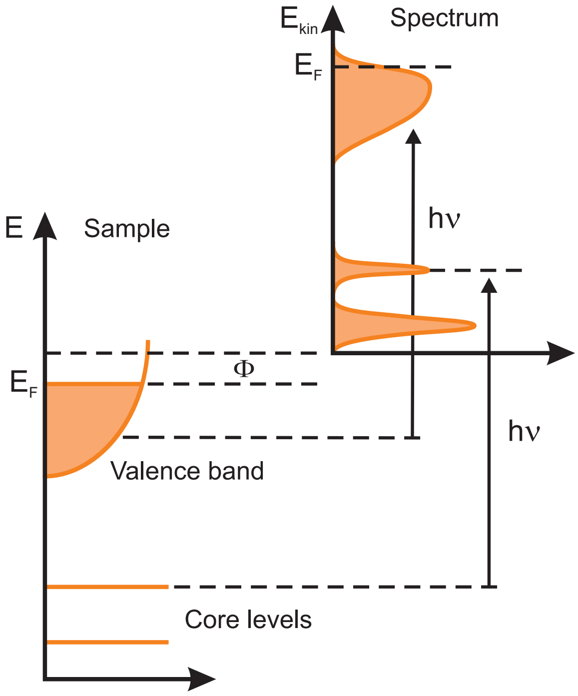

Figure 6.1: The relationship between the energy levels in a solid (left) and the photoemission spectrum (right) produced by photons with energy $h\nu$.

solid; this relationship is illustrated in figure 6.1.

ARPES builds on the principle of photoemission spectroscopy by revealing the momentum of the electrons as well as their energy, allowing for the momentum-dependent band structure to be studied. A sketch of the ARPES process is given in figure 6.2. A monochromatic beam of radiation incident on the sample surface emits electrons with a spread of kinetic energies and over a range of angles. An electron energy analyser with a finite acceptance angle collects these photoelectrons and measures their energy and emission angle. The electron momentum has modulus $p = \sqrt{2mE_{\text{kin}}}$, and its component parallel to the surface is given by

$$p_{\parallel} = \hbar k_{\parallel} = \sqrt{2mE_{\text{kin}}}\sin\theta. \tag{6.2}$$

In considering photoelectron spectra, it is important to make some simplifying assumptions to reduce the complexity of the actual physical process. Ordinarily, this requires invoking the independent-particle picture and the sudden approximation, which means that many-body interactions are ignored and any changes the system undergoes during the photoemission process are neglected. The process is further simplified by the so-called one-step

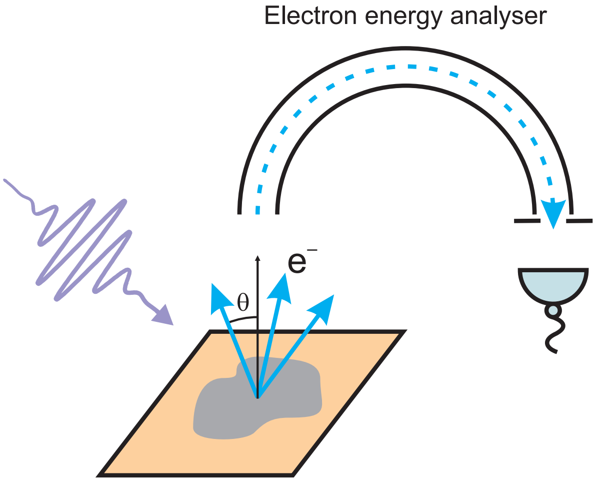

Figure 6.2: Schematic representation of an ARPES experiment. High energy photons emit electrons from the sample surface (grey area) at a variety of angles. They are captured by an analyser, which records their kinetic energy and emission angle based on the path they travel through the system.

process, in which the electron is regarded as undergoing an optical transition from some initial state in the solid to some final ionised state, which also has finite overlap with the initial state [165, 166].

Within these simplifications, momentum conservation relates the initial and final states by

$$\mathbf{k}_f - \mathbf{k}_i = \mathbf{k}_{h\nu}. \tag{6.3}$$

Generally speaking, the photon momentum $\mathbf{k}_{h\nu}$ can be neglected compared to that of the electron, and the transition between states can be considered as vertical. Due to the lack of translational symmetry on crossing the sample surface, the perpendicular component of momentum $\mathbf{k}_{\perp}$ is not conserved in the photoemission process, which means that a complete mapping of $E(\mathbf{k})$ is not always straightforward or achievable. However, translational symmetry is preserved in the plane of the sample, so that $\mathbf{k}_{\|}$ is conserved and the photoelectron momentum $k_{\|}$ in equation (6.2) can be regarded as the crystal momentum.

In the case of low-dimensional materials, the dispersion of $\mathbf{k}_{\perp}$ is negligible and its contribution to the overall electronic dispersion can be dropped. The dispersion is then dependent almost entirely on $\mathbf{k}_{\|}$, and $E(\mathbf{k}_{\|})$ can be mapped by simply measuring photoelectron energy as a function of $\mathbf{p}_{\|}$. This makes one- or two-dimensional materials particularly well-suited for

ARPES studies. In particular, for such materials lacking dispersion along the surface normal, the width of photoemission peaks directly gives the photohole lifetime, which provides information on correlation effects [167].

6.2 Time- and Angle-Resolved Photoemission Spectroscopy

From the preceding section, it can be seen that ARPES is a powerful tool for mapping out band structures in materials. By varying the temperature or chemical composition of the materials of interest, changes in band structure can be followed as phase transitions take place, providing information on the opening or closing of gaps and the restructuring of electronic bands. Early ARPES experiments used photons from helium lamps or synchrotron sources, which offered high-quality data from monochromatic sources.

However, there are many questions concerning the interplay of electrons and phonons which cannot be studied with these equilibrium techniques. By combining photoelectron spectroscopy with ultrafast laser sources, it becomes possible to directly monitor the evolution of electronic states after excitation, shedding light on the correlations between different degrees in the system [28, 168, 169]. The rapid development of femtosecond laser technology in recent years has made pulsed ultrafast sources of high-energy photons more readily available, leading to the burgeoning field of time- and angle-resolved photoemission spectroscopy (TARPES).

Fundamentally, TARPES uses the same principles as optical pump-probe spectroscopy described in chapters 3, 4, and 5, except the probe laser beam is replaced by photoelectrons. An intense pump beam is used to excite the system into a non-equilibrium state, which gradually relaxes back to the ground state. A second laser pulse is used to generate ultraviolet photons, usually by either high harmonic generation in gas jets [170] or by frequency quadrupling of the laser fundamental frequency in successive BBO crystals [29, 37]. The ultraviolet photons are then focussed onto the sample, where they eject photoelectrons whose angle of emission and kinetic energy map out the band structure, as described in section 6.1. By varying the time delay between the two beams, as in any pump-probe experiment, a complete picture of the electronic structure can be built up in time as the electronic structure evolves.

6.3 Photoemission spectroscopy of TaS$_2$

Due to its quasi-two-dimensional properties, TaS$_2$ has become the subject of numerous photoemission studies, where the presence of CDW and Mott effects creates unusual band structures with many interesting features [56, 57, 67, 171–174]. This wealth of experimental data also allows for the testing of many theoretical band structure calculations [65, 175–178]. More details on the properties of TaS$_2$ are provided in chapter 2, but the main points of the band structure will be repeated here for convenience.

In TaS$_2$ the formation of the CDW causes a clustering of groups of thirteen tantalum atoms into star shapes, with two rings of six atoms each centred around the thirteenth atom. When the CDW becomes commensurate with the lattice below $T_c = 180\,\mathrm{K}$, a superlattice forms and the Brillouin zone folds, reflecting the new symmetry of this low-temperature commensurate phase. The original bands become Umklapp, or shadow, bands after translation through the reconstructed Brillouin zone, while the clustering of atoms collapses the electronic structure into submanifolds [64, 172]. Finally, spin-orbit coupling splits off a narrow band from the uppermost submanifold into a gap [65]. This narrow band is then susceptible to electron localisation and a correlation gap is seen to open at the Fermi energy [34, 67].

This gap was widely assumed to be a Mott gap, which explained the observed behaviour of the commensurate phase [54]. However, the CDW plays an important role in the formation of this state and its full contribution to the ground state remained experimentally unverified. Using TARPES, the role of lattice and electronic effects can be separated. After photoexcitation, the transient photoemission spectra revealed a collapse of the lower Hubbard band, with spectral weight shifting across the Fermi energy, resulting in the formation of a metallic state. This was found to take place within the temporal resolution of the experiment ($\approx 50\,\mathrm{fs}$), confirming the Mott insulating nature of the ground state [28, 37]. Conversely, in the case of a gap arising purely from CDW formation, gap melting has been found to proceed on a timescale comparable to the motion of the CDW lattice deformations, i.e. on the order of hundreds of femtoseconds [29]. By clocking the changes to the electronic structure, it has proven possible to separate structural and electronic effects in complex materials, separately monitoring their contributions to the band structure.

To date, TARPES experiments have been limited to photon energies of 6 eV, generated by quadrupling the output of a 1.5 eV laser. From equations (6.1) and (6.2), it is clear that the maximum photoelectron momentum $k_{\|}$ possible occurs for electrons at the Fermi energy, when $E_{\mathrm{kin}} = h\nu - \Phi$. This means that the amount of Fermi surface which can be investigated using TARPES is fundamentally limited by the photon energy used; going to higher photon energies would allow for higher electron momenta, revealing more of the Brillouin zone.

In TaS_2, which has a work function $\Phi = 5.5\,\mathrm{eV}$, the use of 6 eV photons limits photoemission measurements to the centre of the Brillouin zone. However, due to the complicated interplay between the CDW and Mott physics in determining the ground state properties, it is desirable to look at different regions of momentum space to get a complete picture of the electronic band structure. In particular, due to the incomplete CDW relaxation described in chapter 5, it would be prudent to investigate effects at the edges of the folded Brillouin zone, which arises from the CDW distortions. At the same time, it is necessary to maintain a high-degree of temporal resolution in order to differentiate structural and electronic effects.

The rest of this chapter will outline experiments undertaken using ultrafast high-harmonic sources to map changes across large portions of momentum space in TaS_2 in response to photoexcitation. In combination with the results of chapter 5, an even more comprehensive view of the photoinduced phase of this fascinating material is obtained.

6.4 TARPES Experiments in TaS_2

6.4.1 Experimental setup

Time- and angle-resolved photoemission spectroscopy was carried out on the Artemis beamline at the Central Laser Facility of the Rutherford Appleton Laboratory. This facility is based around a high-average-power laser source producing 30 fs pulses at 785 nm, which is used to generate short pulses of tuneable ultraviolet radiation. A schematic of the layout of the facility is shown in figure 6.3.

The laser is a 1-kHz Ti:sapphire amplified system, capable of producing up to 14 mJ pulse energies. 600 μJ of this is sent into the high harmonic generation vacuum chamber, where it is focussed down into a pulsed jet of argon gas. For sufficiently high gas pressures and laser intensities, high harmonic generation takes place via above-threshold ionisation [179, 180]. This process can be considered using a simple semi-classical approach [181, 182]. When a

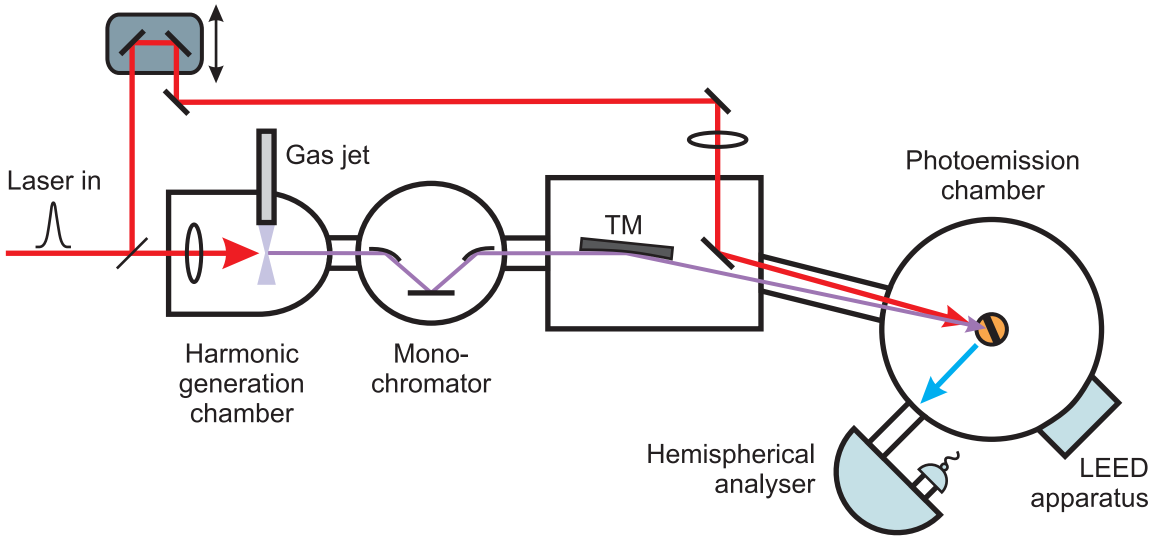

Figure 6.3: Schematic of the TARPES layout at the Artemis beamline. TM is the toroidal mirror. The sample (black rectangle) sits at the centre of the photoemission chamber on a cryogenically cooled sample mount (orange circle). Photoelectrons (blue arrow) are detected by a hemispherical analyser attached to the chamber. A LEED apparatus allows for sample surface characterisation and orientation.

strong electric field is applied across an atom, the potential experienced by an electron can be lowered sufficiently to allow it to escape by tunneling ionisation. Half an optical cycle later, the field direction changes and the electron finds itself accelerated back towards the atom, picking up kinetic energy as it travels. It can then recombine with the core, emitting high energy harmonic photons as it does so. The frequency of the harmonic depends on the electron trajectory, so on the point at which it is 'born' during the laser field, which then determines the kinetic energy it has upon recombination [183].

The harmonic generation scheme at Artemis is capable of producing harmonics in the extreme ultraviolet (XUV) range between 10 and 100 eV [170]. Single harmonics can be selected from the spectrum produced by the gas jet using a specially designed monochromator, consisting of a pair of toroidal mirrors and a plane diffraction grating, as shown schematically in figure 6.3. The first mirror collimates the XUV light and directs it onto the grating, whilst the second one refocusses it onto an exit slit. The grating is positioned in an off-plane mounting, such that the wave vectors of the incident and diffracted light are nearly parallel to the grooves. This provides higher efficiency from the monochromator and also reduces its effect on the temporal profile, so that short pulses may be maintained [184, 185]. There is, of course, a trade-off between pulse duration and frequency resolution, but this trade-off is minimised using this design. The monochromatic XUV beam is focussed into the photoemission chamber by a final toroidal mirror.

The photoemission chamber contains a cryogenically-cooled sample mount and a helium lamp for static high-resolution ARPES measurements at $21.2\,\mathrm{eV}$. Photoelectrons emitted from the sample are collected by a hemispherical analyser, which adjusts the trajectories of incident electrons according to their kinetic energy. A multichannel plate, phosphor screen, and CCD camera arrangement is used to detect the photoelectrons, producing momentum- and energy-resolved images.

In addition, the sample mount can be rotated to make use of the low energy electron diffraction (LEED) apparatus fitted to the photoemission chamber, as shown in figure 6.3. The LEED apparatus allows the sample surface to be checked for cleanliness through the quality of the observed diffraction pattern. It also enables the Brillouin zone orientation to be determined. The sample may then be rotated about its surface normal to fix the cuts through the Brillouin zone that will be made during ARPES measurements.

Due to the large energies achievable, the high harmonic photons allow for static band structure measurements to be taken over large portions of the Brillouin zone. However, the real power of this source lies in its pulsed nature, which means it can be combined with a second laser pulse to produce time-resolved band structure images, as described in section 6.2.

As shown in figure 6.3, this second pulse comes from the remaining beam not used for high harmonic generation. A delay stage allows for the time delay between the two beams to be adjusted. The pump beam is then brought in alongside the XUV beam in the toroidal mirror chamber, so that pump and probe are close to collinear, and is focussed down by a long focal length lens to an intensity of $\approx 1\,\mathrm{mJ\,cm^{-2}}$.

The TaS_2 sample was held at $20\,\mathrm{K}$, so that it was in the Mott insulating commensurate phase. From the generated harmonic spectrum, the thirteenth harmonic was selected, providing XUV photons of $20.8\,\mathrm{eV}$ energy. The energy resolution of the system is $180\,\mathrm{meV}$, which is limited by the linewidth of the harmonic source. While better resolution is in principle possible, it comes at the sacrifice of temporal resolution, which is paramount for this

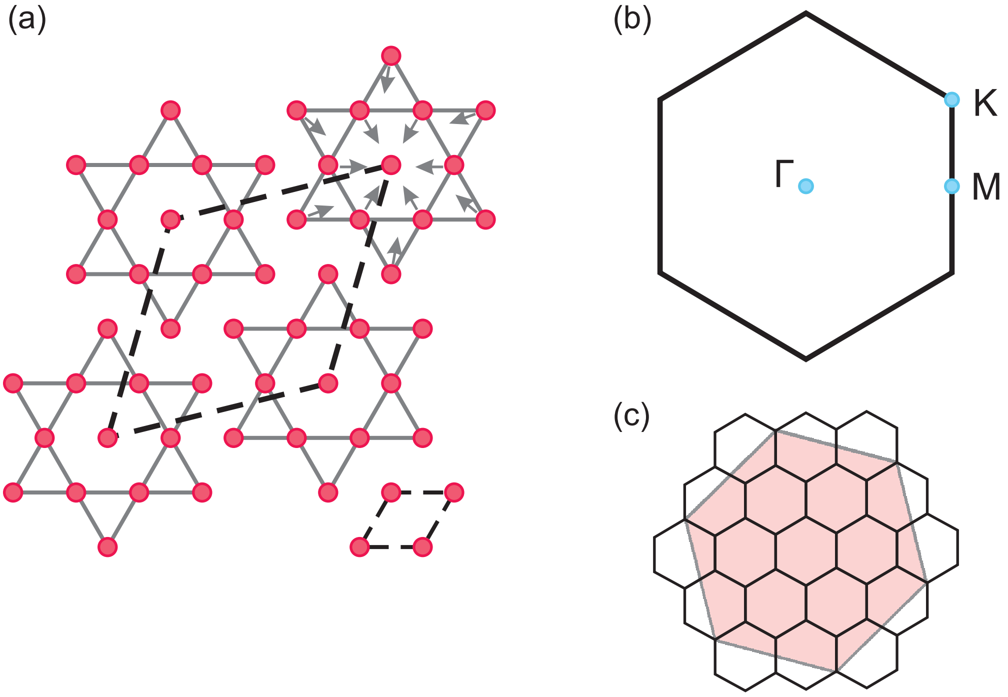

Figure 6.4: (a) Tantalum plane of TaS$_2$, after figure 2.3. Solid grey lines are the star clusters while arrows show the atomic displacements upon cooling. Dashed lines indicate the low-temperature commensurate CDW phase unit cell (centre) and the unit cell in absence of the CDW at high temperatures (bottom right). (b) Brillouin zone for the low-temperature commensurate structure. The high-symmetry points are labelled by blue dots: Γ – zone centre, M – centre of a zone face, and K – middle of an edge joining two faces. (c) Relationship between the high-temperature undistorted phase Brillouin zone (pink with grey lines) and that of the low-temperature commensurate phase (black lines).

experiment.

With the high photon energies presented by this apparatus, it is possible to study the momentum-dependent behaviour of the electronic structure of TaS$_2$ as it undergoes the photoinduced insulator–metal phase transition. In particular, areas of the Brillouin zone can be explored away from the zone centre, so that effects near the zone edges may be studied.

6.4.2 Static measurements

As a first test of the apparatus, the laser harmonic source was used to generate static photoemission spectra from TaS$_2$ as a function of energy and momentum. These were then compared

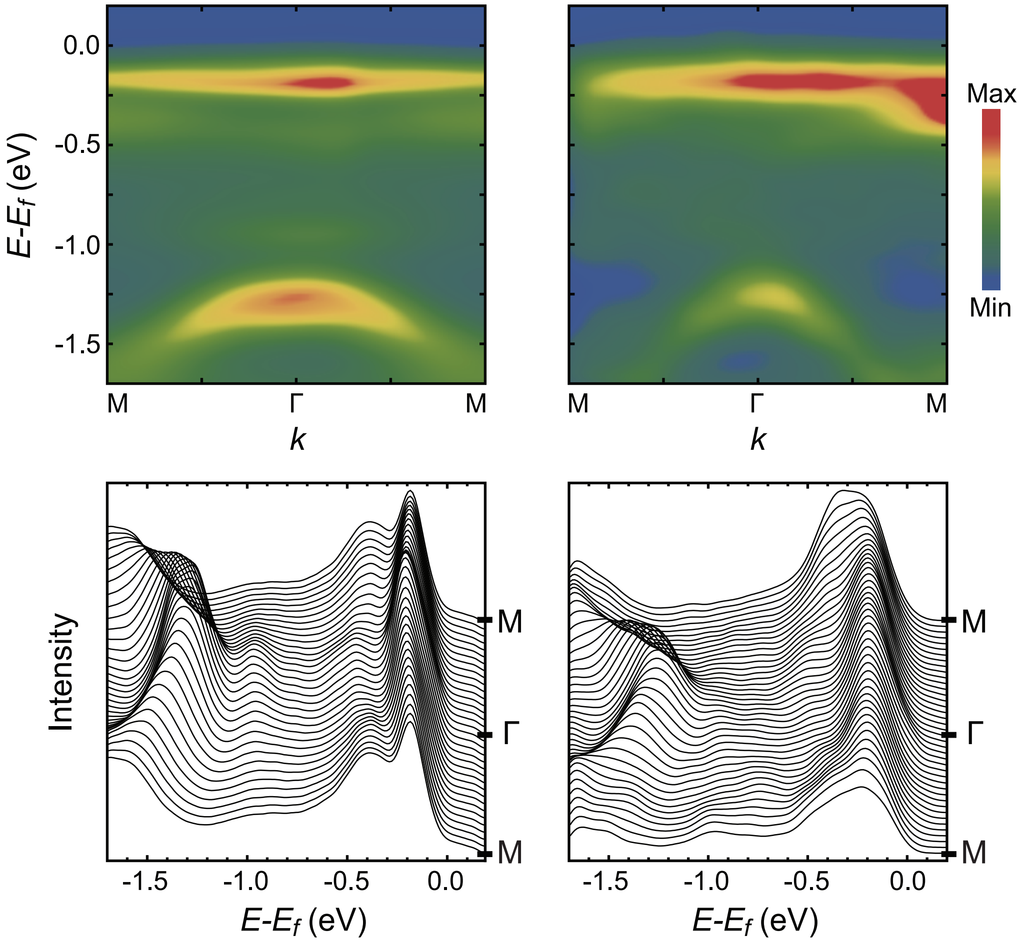

Figure 6.5: Static photoemission intensity maps (top) and energy distribution curves (bottom) for the low-temperature phase of TaS_2. Left panels show the helium lamp source data; right panels show the laser-harmonic source data.

to similar spectra taken with the helium gas discharge lamp. The structure of TaS_2 shown in chapter 2 is given again for reference in figure 6.4(a). Figure 6.4(b) shows the Brillouin zone for the low-temperature commensurate phase. Throughout this chapter, the points Γ and M in the Brillouin zone always refer to the points in the low-temperature phase as labelled in figure 6.4(b). The connection between the low- and high-temperature Brillouin zones is illustrated in figure 6.4(c): the zone rotates with the CDW wave vector and contracts upon appearance of the superlattice.

Photoemission measurements obtained with the two sources are shown in figure 6.5. Some asymmetry is present in the spectra, particularly for the laser source (right-hand panels of figure 6.5). These asymmetries are caused by two effects. First of all, as is clear from figure 6.3, the experimental geometry means that photons from either source are incident at large angles to the sample surface when looking at photoelectrons emitted near normal incidence, so around the centre of the Brillouin zone. As the sample is rotated to look from one side of the zone to the other, the angle of incidence of the XUV photons is not symmetric about the surface normal. The optical constants can change rapidly, such that the absorption is not symmetric about the zone centre. This angular variation is also polarisation dependent, which is the second cause of the asymmetric spectra. The helium lamp is unpolarised, whereas the laser source is p-polarised, leading to the differences in symmetry between the two spectra.

Despite the asymmetry, the laser source is able to reproduce the salient features of the spectrum. The appearance of the Mott gap is indicated by the limited spectral weight at the Fermi energy and the formation of the lower Hubbard band at around $-0.2\,\mathrm{eV}$. The sub-manifolds associated with the structural distortions can be resolved, with the shadow bands appearing at $k = 0$ (the Γ point). These bands are separated by a gap at the reconstructed Brillouin zone boundary (the M point). All these features are in agreement with existing photoemission data on TaS_2 [28, 34, 172]. In light of this, the time-resolved measurements are expected to produce reliable representations of the changes in band structure after photoexcitation.

6.4.3 Time-resolved measurements

Time-resolved measurements of the photoemission spectrum were made as the phase transition occurs and the system evolves in response to excitation of TaS_2 with a pump laser pulse. The time-dependent energy distribution of photoelectrons is shown in figure 6.6, where the response has been integrated across the entire Brillouin zone. The collapse of the Mott gap is indicated by a loss of intensity below the Fermi energy, especially in the lower Hubbard band, along with an increase of spectral weight above it. Following this prompt change, there are oscillations in the intensity due to a rigid shift back and forth of the entire spectrum, as shown in figure 6.6(b). These oscillations occur at the frequency of the CDW amplitude mode and are connected to its coherent excitation. These features are all in agreement with the earlier time-resolved studies [28, 37].

What separates this study from the previous ones is the ability to have momentum reso-

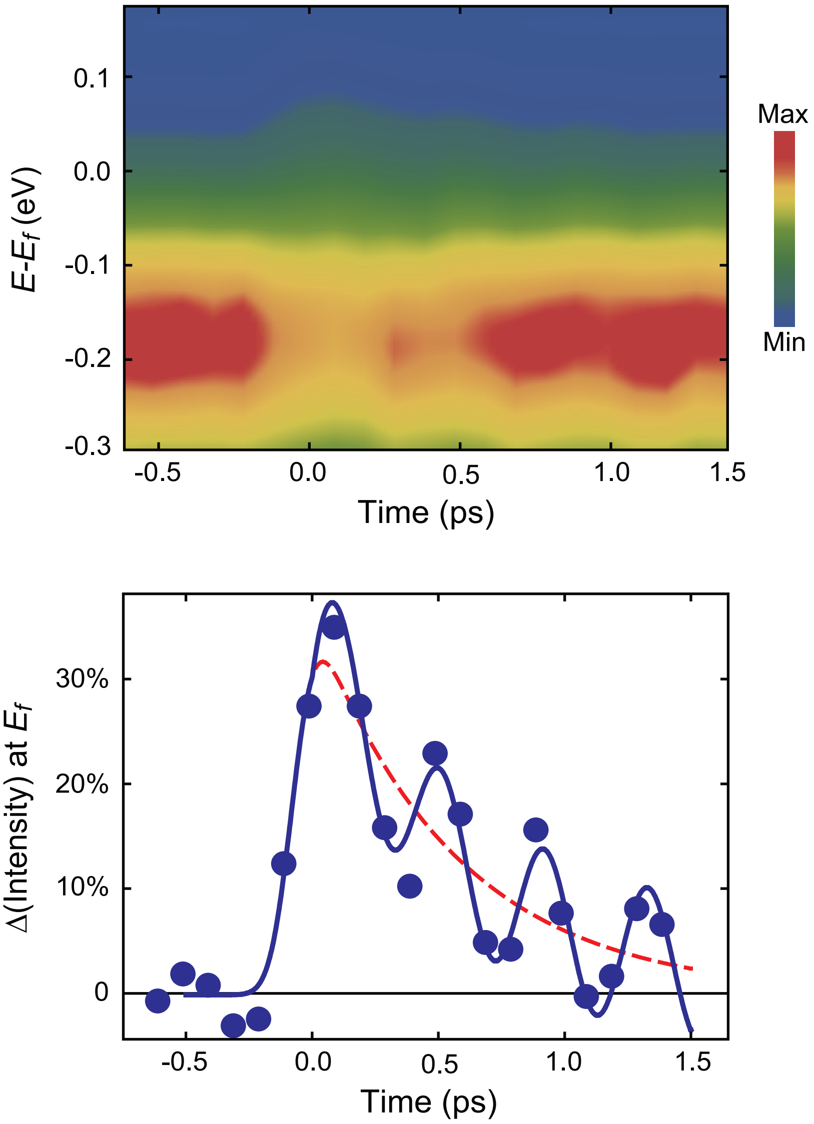

Figure 6.6: Temporal behaviour of the electronic structure. (a) Map of photoelectron intensity, integrated over the entire Brillouin zone, as a function of time before and after photoexcitation. (b) Intensity changes at the Fermi level. Dots are experimental data, while the blue line is a fit accounting for the onset and oscillatory decay of the electronic response. The red dashed line is the non-oscillatory component of the fit.

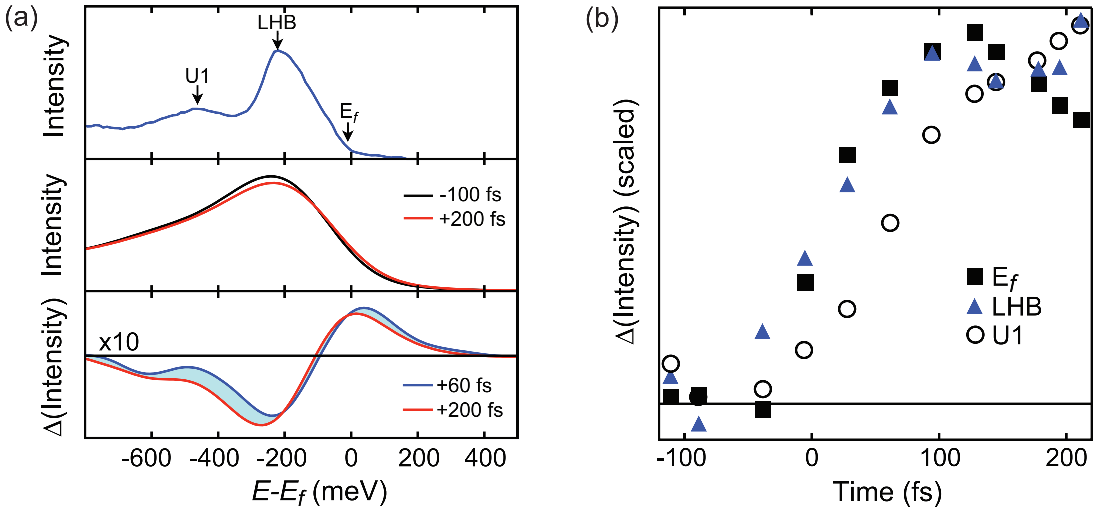

Figure 6.7: Evolution of the bands through the photoinduced phase transition. (a) The top panel shows a high-resolution energy distribution curve (EDC) at the Γ point. U1 – uppermost Umklapp band. LHB – lower Hubbard band. E$_f$ – Fermi energy. The middle panel gives EDCs before and after photoexcitation. The bottom panel shows differential EDCs at 60 and 200 fs after photoexcitation. (b) Temporal evolution of changes at the Γ point for three key energies.

lution and observe a large portion of the Brillouin zone. Of particular interest is the response of the lower Hubbard band and the uppermost Umklapp band, where effects are found to occur at different rates. Changes taking place at the Γ point are summarised in figure 6.7. As shown in figure 6.7(a), spectral weight at the Fermi level and just above it appears promptly and has begun to decay by 200 fs. On the other hand, around the uppermost Umklapp band the intensity is suppressed, and this suppression is still growing 200 fs later. This difference in behaviour can be seen more clearly in figure 6.7(b). Here, the intensity changes are plotted as a function of time for the three key areas of the photoemission spectrum: at the Fermi energy, at the lower Hubbard band, and at the uppermost Umklapp band.

From figure 6.7, then, there are clearly different timescales associated with the changes at different positions in momentum and energy, which can be attributed to different physical mechanisms. At the Fermi energy there is an increase in intensity brought about by the melting of the Mott gap. This change is expected to be prompt, as it is connected to the electronic phase transition. Indeed, its response time is equal to the pump-probe cross-correlation time of 45 fs. The gap collapse also causes the loss of intensity at the lower Hubbard band, and the same temporal response is seen there. At lower energies, in the shadow bands, the response is slower. This is consistent with a reduction in spectral weight brought about by unfolding of the band structure due to incipient relaxation of the coupled CDW and lattice distortion. Such changes occur on structural rather than electronic timescales, hence the slower response time.

Whilst one timescale dominates over the other at these three key regions, at different energies and momenta the spectral changes are characterised by a mixture of the two. Figure 6.8 illustrates the temporal evolution of the differential photoelectron intensity at both the zone centre and the zone boundary for a number of different energies. To separate the contributions of electronic and structural processes, the data at earliest times were fitted in the time domain using two timescales. The first is that of the prompt electronic response of the system, limited by the instrumental response time; the second slower timescale is associated with the onset of structural relaxation. The fit then takes the form

$$\Delta I(t) = A\,\mathrm{erf}(t/w) + \left(e^{-t^2/w^2}\right) * \left(Be^{(t-t_0)/\tau}\right). \tag{6.4}$$

The first term represents the electronic response as an error function of width w, derived from a step function convolved with the Gaussian pump-probe cross-correlation function, which has a full width at half maximum of $w = 45\,\mathrm{fs}$. The second term represents the structural response, where this time the cross-correlation is convolved with an exponential increase that only begins to turn on at $t = 0$. The time constant τ for this exponential growth is equal to half of the CDW amplitude mode period ($\omega_{\mathrm{AM}} \approx 2.5\,\mathrm{THz}$). The resulting fits are given by the solid lines in figure 6.8.

The relative contribution of the two components varies as the momentum is increased from Γ to M, as can be seen by comparing the two panels of figure 6.8. This becomes more apparent in figure 6.9(a), where the amplitudes of the electronic and structural fit components across the Brillouin zone are displayed separately.

On electronic timescales, spectral intensity is lost at the peak of the lower Hubbard band and transferred across the Fermi level. This corresponds to the creation of hot electrons and the loss of the Mott gap. As seen in figure 6.9(a), this process is momentum independent, indicating that the effects of the electron-electron interaction pervade the Brillouin zone.

Conversely, the structural response exhibits dispersion, with some important features

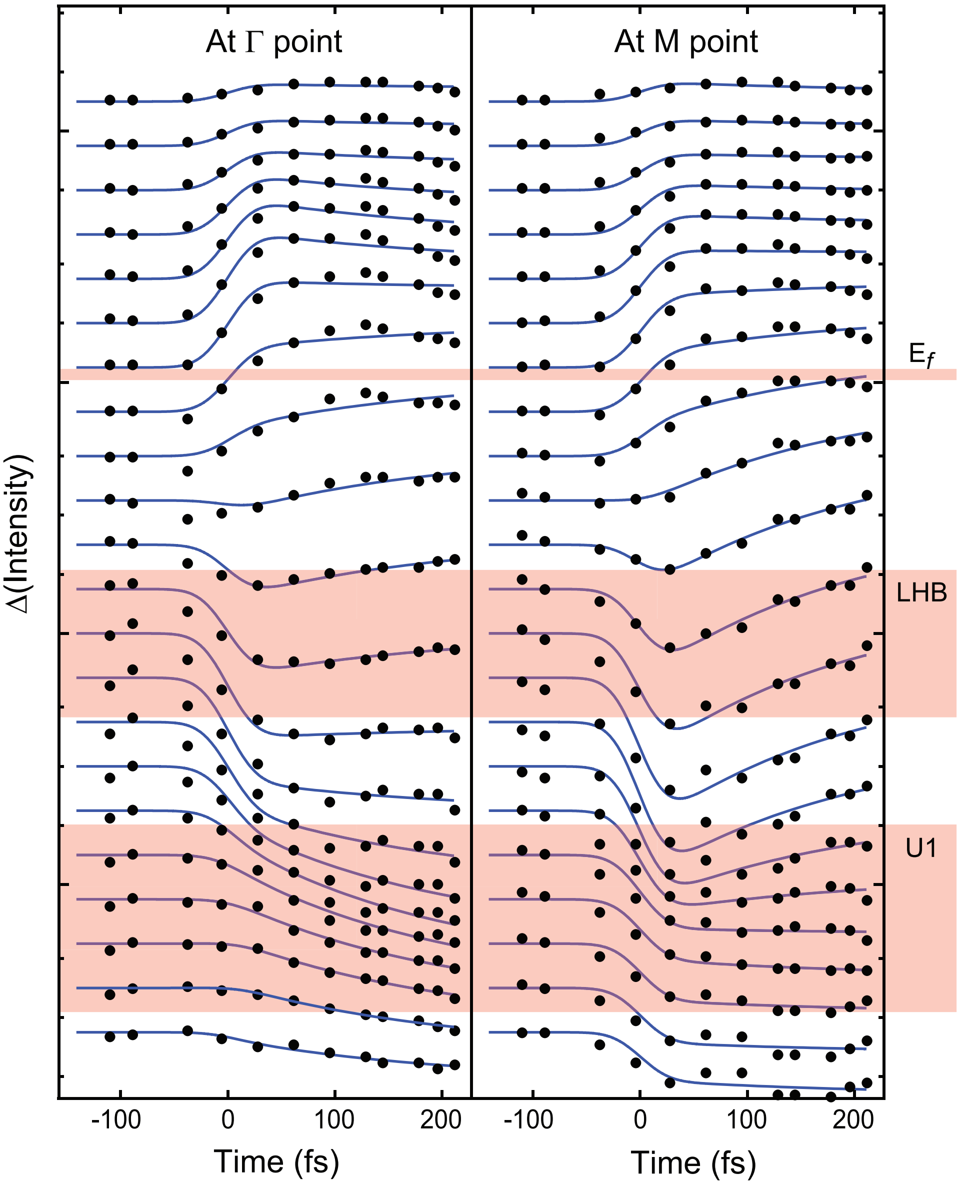

Figure 6.8: Variation of dynamics over the full range of energies at the Γ (left panel) and M points (right panel). Each trace represents the intensity change at a particular energy. Dots are experimental data and curves are fits to a two-component model (see text). Key spectral features are indicated by the shaded regions, where U1 is the uppermost Umklapp band, LHB is the lower Hubbard band, and E$_f$ is the Fermi energy.

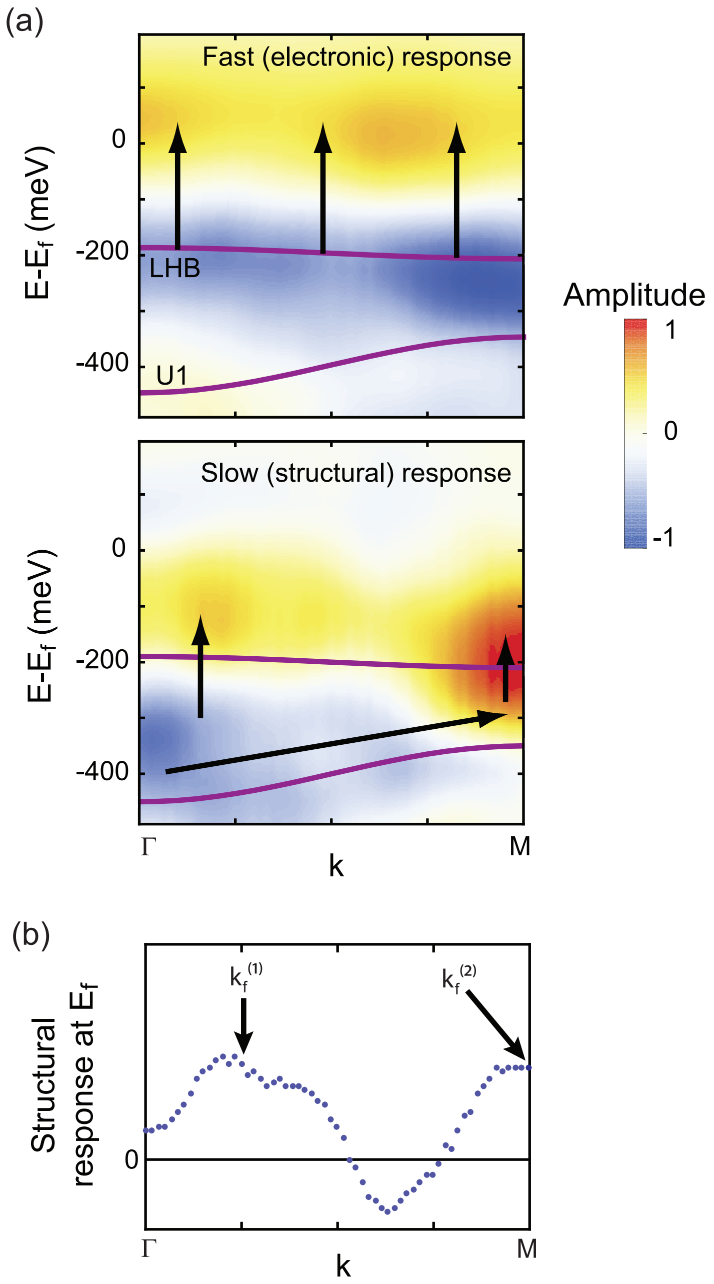

Figure 6.9: (a) Spectral distribution of changes to band structure on electronic (top) and structural (bottom) timescales. The purple lines indicate the lower Hubbarb band (LHB) and uppermost Umklapp band (U1) peak positions in the low-temperature insulating phase. The arrows indicate transfer of electronic spectral weight. (b) Amplitude of slow changes in spectral intensity at the Fermi level. The arrows indicate the two Fermi wave vectors in the high-temperature incommensurate phase.

emerging from the lower panel of figure 6.9(a). Around $k = 0$, a negative amplitude for the structural fit component in the Umklapp band indicates a partial loss of this band as the CDW distortion relaxes and the zone unfolds. Furthermore, there is positive amplitude between the low-temperature bands at the M point, signifying a softening of the CDW gap in this region. Across the Brillouin zone, positive amplitude is concentrated above the lower Hubbard band peak, implying that the band edge is shifting upwards in energy as the structure relaxes. Figure 6.9(b) plots the amplitude of the structural fit component near the Fermi energy. From this, it can be seen that the energy shift due to the relaxation is concentrated at the Fermi wave vectors of the high-temperature incommensurate phase. So, photo-doping not only melts the Mott gap, creating a transient metallic phase, but it also partially undoes the low-temperature structural distortions, driving the system back towards the undistorted high-temperature phase.

6.5 Summary

This chapter has built on the characterisation of the photoinduced phase of TaS$_2$ undertaken in chapter 5 by monitoring the temporal evolution of the electronic band structure in response to excitation with light. This has been done using time- and angle-resolved photoelectron spectroscopy with sub-50-fs time-resolution to separate the effects of electrons and lattice. Additionally, the high photon energy used enabled a full investigation of the Brillouin zone to be undertaken, expanding upon previous photoemission measurements [28].

At the earliest times of the phase transition, TaS$_2$ is seen to become metallic through the collapse of the Mott gap. At the same time, structural relaxation begins to occur, though its slower onset shows that it is not the driving force behind the transient metallic state. Long-range CDW order is retained in this phase, as shown by femtosecond electron diffraction measurements [71] and as suggested by the results of chapter 5. However, the TARPES study indicates that the effects of CDW-related backfolding of the Brillouin zone are at least partially undone by photoexcitation, shifting the band edge up in energy towards the high-temperature phase.

The ability to separate time and energy scales across momentum space afforded by TARPES experiments is a crucial step in understanding the dynamics of strongly correlated materials. In future, it should allow for the testing of theories of the electronic spectrum in complex systems, as well as unveiling the interplay between their different degrees of freedom. When combined with other spectroscopic techniques, such as those presented elsewhere in this thesis, a more detailed and richer understanding of the physics of correlated materials begins to emerge.

Chapter 7

Vibrational Excitation of Complex Materials

7.1 A New Approach

The photoexcitation technique used in the preceding chapters and, indeed, in the majority of previous pump-probe experiments, relies on pumping the system with photons on the eV energy scale. This energy couples directly to the electrons, creating hot carriers which then interact with the other degrees of freedom, re-distributing the energy throughout the system. It has also frequently been mentioned that the ground state of a complex material is determined by strong competition between many parameters, including phonons, electrons, and magnetic interactions. Furthermore, many photoinduced phase transitions are accompanied by structural changes, making the role of electrons and phonons in the transition somewhat unclear. A natural question then arises: can a phase transition be initiated by driving phonon excitations, without exciting the electronic structure? If light can be coupled to a lattice vibration by making its frequency resonant with that of the phonon mode, this could help elucidate the role of structural distortions in the phase transition.

This chapter will present some preliminary work on this approach. These ‘vibrational control’ experiments were initially carried out in the manganites, although the technique is now being extended to other materials, including organic Mott insulators and cuprates. Tabletop techniques allow for investigations into the mid-infrared range, whilst free electron lasers offer the opportunity to explore the role of much lower-energy excitations.

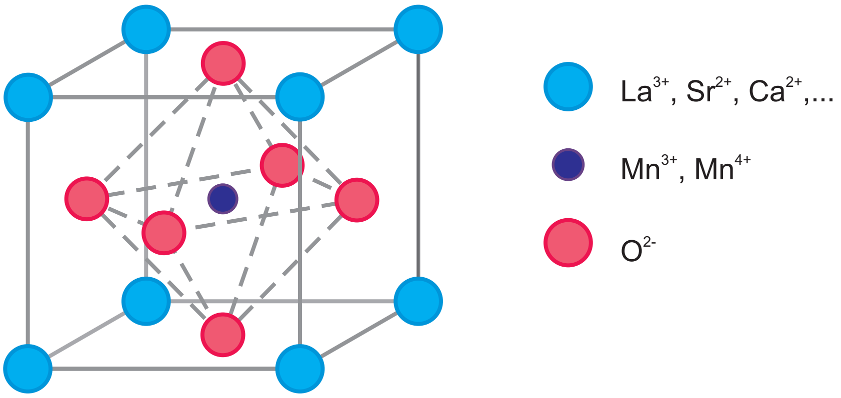

Figure 7.1: The ideal unit cell of an ABO_3 perovskite. The A-sites are occupied by rare earth ions at the corners of the cell. The B-sites are occupied by manganese ions. Oxygen ions form an octahedral cage around the manganese ion.

7.2 Manganites

7.2.1 Basic properties

The manganites are a family of materials containing trivalent or tetravalent manganese ions [186]. Many of them form in the ABO_3 perovskite structure, illustrated in figure 7.1. In this type of structure, the A-sites contain large ions, typically rare earth or alkaline earth ions, such as Ca^{2+}, La^{3+}, or Sr^{2+}, whilst the B-sites have a smaller ion of Mn^{3+} or Mn^{4+}, or some other transition metal for different oxide families, such as cuprates or cobaltites. The O^{2-} ions sit on the faces of the A-site cube, forming an octahedral cage around the central manganese ion.

The manganese ions have an active d-shell, with five degenerate levels in the uppermost $3d$ manifold. When placed into the perovskite crystal structure, the crystal field lifts this degeneracy, creating a lower-energy three-fold-degenerate t_{2g} level and a higher-energy two-fold-degenerate e_g level. This crystal-field splitting, often referred to as the $10Dq$ splitting, is typically of the order of 1 or 2 eV in manganites [187]. A sketch of the splitting is given in figure 7.2.

There is a strong Hund coupling between the spins in manganites, which results in the four electrons of the Mn^{3+} ion being in a state of maximum spin [188]. This produces the configuration $t^3_{2g\uparrow}e_{g\uparrow}$, as shown in figure 7.2. This configuration is unstable to a Jahn-Teller

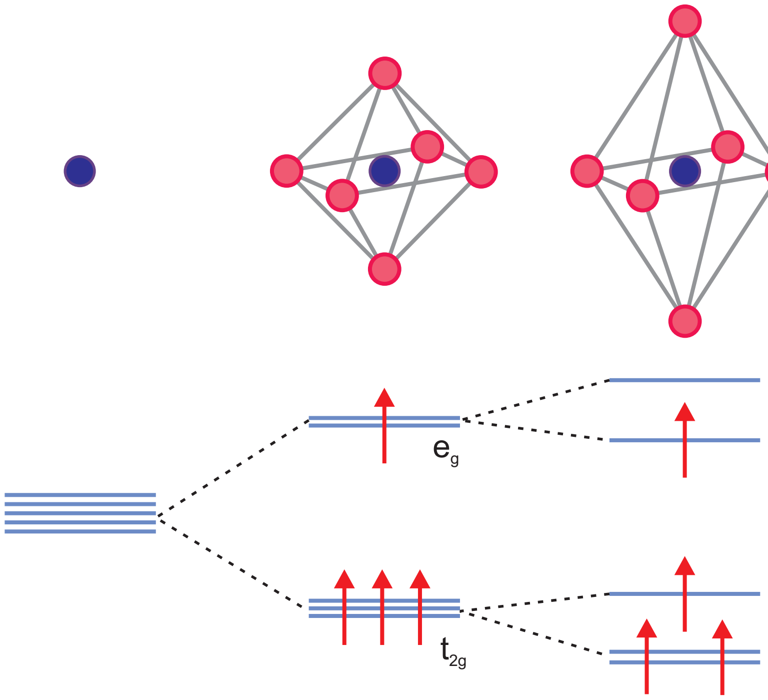

Figure 7.2: Schematic representation of the *d*-level electronic structure for a Mn ion in isolation (left) and in the presence of cubic (middle) and tetrahedral (middle) crystal fields. Arrows indicate spins.

distortion of the lattice [189], in which the degeneracy of the t_{2g} and e_g levels can be lifted and the overall energy of the system lowered. This can be viewed by considering the electron orbitals: the t_{2g} levels consist of d_{xy}, d_{yz}, and d_{zx} orbitals, which point between the oxygen anions, whilst the e_g levels consist of $d_{x^2-y^2}$ and $d_{3z^2-r^2}$ orbitals, pointing towards the oxygen anions. Then, for a distortion along the z-direction, the Coulomb energy of the $d_{3z^2-r^2}$ orbital is lowered due to the expansion along this axis. However, this increases the Coulomb energy between the $d_{x^2-y^2}$ orbital and the oxygen anions. For the Mn^{3+} cation, the $d_{x^2-y^2}$ orbital is unoccupied, so it becomes energetically favourable for the distortion to take place. This effect is illustrated on the right-hand side of figure 7.2. In Mn $^{4+}$ ions, the e_g levels are empty and there is no Jahn-Teller effect.

Additional deviations from perfect cubic perovskite structure occur in the form of tilting of the oxygen octahedra. The degree of tilting is dependent on the size of the A-site cation [190], and is an important parameter for the properties of the manganites, as shall be seen shortly.

Interest in manganites grew dramatically in the 1990s after they were found to display the colossal magnetoresistance effect [191–193]. Magnetoresistance describes the change in electrical resistivity of a material under the influence of an external magnetic field. Ordinarily, the resistivity increases when a magnetic field is applied, since the electron path is lengthened by the additional force of the field. However, manganites show the opposite behaviour, with the resistivity decreasing with increasing magnetic field. This negative magnetoresistance was dubbed colossal due to the enormous size of the effect; resistivity changes of some nine orders of magnitude have been recorded [193].

7.2.2 Phase transitions

From the preceding discussion, it is clear that the manganites are highly sensitive to the types of ion used, the number of electrons in the system, and the departure from cubic structure introduced by distortions. Indeed, the correlations between charge, lattice, spin, and orbital degrees of freedom are very strong, and subsequently manganites display a range of interesting phenomena. Moreover, they exhibit very rich phase diagrams as external parameters such as temperature, pressure, chemical doping, and magnetic field are varied, with subtle changes leading to dramatic alterations in the macroscopic properties.

Many different phases can be obtained by altering the chemical doping. By changing the A-site ions to some new composition of the form $\mathrm{A}_{1-x}\mathrm{A}'_x\mathrm{MnO}_3$, the ratio between trivalent and tetravalent manganese ions is shifted. This alters the magnetic state by changing the spin from site to site, which can have a large impact on the conducting properties. The ground state can include insulating and metallic ferromagnetic or insulating antiferromagnetic phases, and may show charge and/or orbital ordering behaviour [187]. As an example of the variation in behaviour, the phase diagram for $\mathrm{La}_{1-x}\mathrm{Sr}_x\mathrm{MnO}_3$ as a function of temperature and chemical doping x is shown on the left-hand side of figure 7.3, where an array of metallic and insulating phases may be observed.

In addition to altering the number of holes at the manganese sites, chemical substitution produces mismatch between the ionic radii at the A-sites, which can introduce strain. For smaller A-site cations, the oxygen anions are pulled away from their ideal positions, distorting the octahedra. This changes the Mn–O–Mn bond length and angle, and alters the electronic bandwidth.

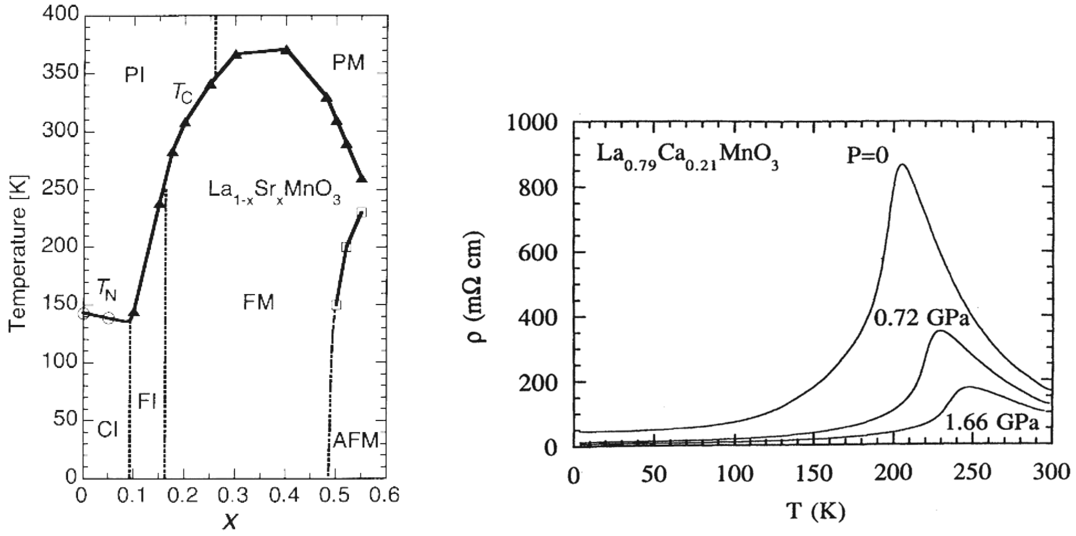

Figure 7.3: Properties of manganites. Left: phase diagram for $\mathrm{La}_{1-x}\mathrm{Sr}_x\mathrm{MnO}_3$, taken from [194]. PI, PM and CI denote paramagnetic insulating, paramagnetic metallic and spin-canted insulating states, respectively. FI, FM, and AFM denote ferromagnetic insulating, ferromagnetic metallic, and antiferromagnetic metallic states. Right: effect of pressure on resistivity as a function of temperature in $\mathrm{La}_{0.79}\mathrm{Ca}_{0.21}\mathrm{MnO}_3$, taken from [195].

In manganites, conduction takes place by hopping of electrons from manganese site to manganese site via intermediate oxygen sites in a ‘double-exchange’ mechanism [196, 197]. The effective hopping t between sites is proportional to $\cos\theta$, where θ is the angle of the Mn–O–Mn bond. For large distortions, then, θ shrinks and the kinetic energy of the electrons decreases, reducing the hopping and creating a tendency for insulating behaviour.

The bond angle, and, more importantly, the orthorhombic distortion of the manganites, is often quantified through the geometric ‘tolerance factor’, defined as

$$\Gamma = \frac{d_{\text{A–O}}}{\sqrt{2}d_{\text{Mn–O}}}, \tag{7.1}$$

where $d_{\text{A–O}}$ is the distance between the A-site and the nearest oxygen ions, and $d_{\text{Mn–O}}$ is the shortest distance between manganese and oxygen ions [187]. An undistorted structure has $d_{\text{A–O}} = \sqrt{2}$ and $d_{\text{Mn–O}} = 1$, in units of the Mn–O distance, and hence has $\Gamma = 1$. As the A-site ions shrink and the oxygens move away from their ideal positions, $d_{\text{A–O}}$ gets smaller and $\Gamma < 1$, indicating a reduced Mn–O–Mn angle and thus a reduced hopping amplitude as the electron orbital overlap decreases. The tolerance factor is minimised for a bond angle of

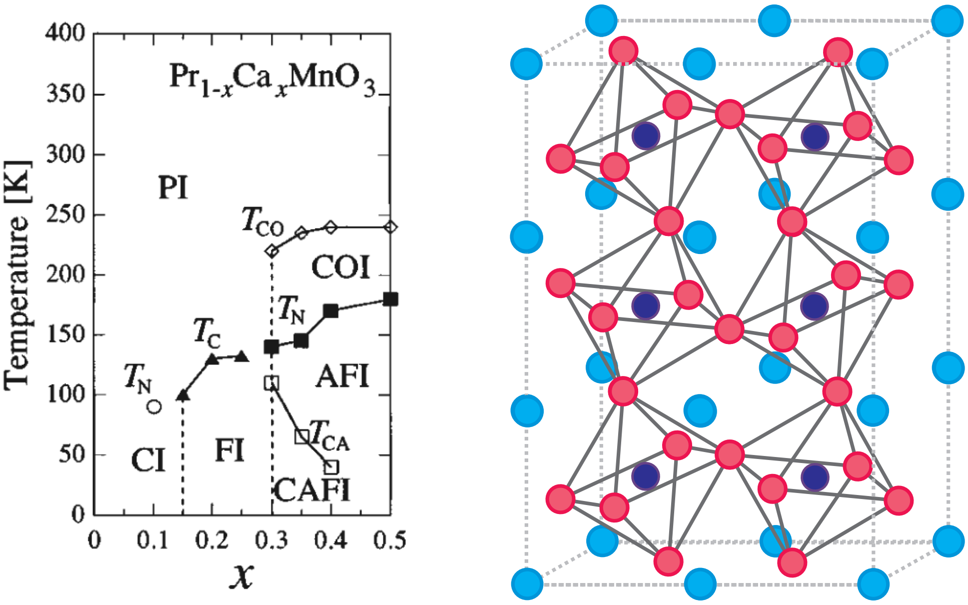

Figure 7.4: The properties of $Pr_{1-x}Ca_xMnO_3$. Left: phase diagram as a function of temperature and doping x. PI, COI, CI, and FI are paramagnetic, charge-ordered, spin-canted, and ferromagnetic insulators, respectively. AFI and CAFI are antiferromagnetic and canted antiferromagnetic insulators. Right: structure of $Pr_{1-x}Ca_xMnO_3$, with the orthorhombic distortion exaggerated for clarity.

90°, when the hopping also vanishes [197, 198].

As well as being affected by doping, the tolerance factor can also be altered by applying pressure. This changes the distortion of the structure, altering both the octahedral tilting and any Jahn-Teller distortions which may be present. In turn, the bandwidth and the conducting properties can be altered. The effect of pressure on resistivity is shown on the right-hand side of figure 7.3 for $La_{0.79}Ca_{0.21}MnO_3$. Here, the resistivity is quashed and the ferromagnetic transition temperature, given by the peak in the resistivity curve, is shifted by increasing the hydrostatic pressure.

7.3 $Pr_{1-x}Ca_xMnO_3$

$Pr_{1-x}Ca_xMnO_3$ (PCMO) is unique among the manganite family inasmuch as it has no insulating phase for any temperature or chemical doping [193]. This is due to the small ionic radius of the calcium cations, which produces a large distortion of the oxygen octahedra and a tendency toward charge localisation. As a result, the tolerance factor Γ is small. The phase diagram of PCMO is shown on the left of figure 7.4, while its structure is shown on the right. In this diagram the tilting has been exaggerated for effect.

Despite of the lack of metallic behaviour with chemical doping, it is possible to induce an insulator–metal phase transition by application of magnetic field [193] and external pressure [199, 200]. Furthermore, at $x = 0.3$, there is a photoinduced metallic phase, which has been characterised by large resistivity changes [201–203].

Given the existence of this photoinduced phase, the importance of the structural distortions on the electronic properties, and the pronounced distortion present in this compound, PCMO would seem to be a natural candidate for a vibrational control experiment. The conducting properties rely on the structure, modulation of which by pressure drives the system metallic. If the structure can be directly modulated using light, it may be possible to drive the system into a conducting phase without excitation of the electrons, but by altering the conducting pathways themselves.

Figure 7.5 shows the optical conductivity of PCMO between 10 and 100 meV [204]. Three modes are present at 23, 42, and 71 meV, corresponding to three infrared active vibrational modes of a cubic perovskite. They are identified as the Pr/Ca site external mode, the Mn–O–Mn bending mode, and the Mn–O stretching mode, respectively [205]. The experiments discussed in the rest of this chapter will focus on large-amplitude coherent excitation of these modes in a bid to drive the system into a metallic state on ultrafast timescales.

7.4 Vibrational Control Experiments

7.4.1 Experimental setup

The experimental setup used for the vibrational control measurements is very similar to that employed in the TaS_2 measurements of chapter 5. Figure 7.6 illustrates the layout. A Ti:sapphire laser operating at 1 kHz and 800nm central wavelength is split into two parts. The larger part of the beam is fed into an optical parametric amplifier (OPA), whose design is the same as that described in chapter 3. This OPA acts as the pump source. The signal and idler outputs are spilt using dichroic mirrors and then recombined non-collinearly in a GaSe crystal, where they interact to produce tunable mid-infrared light by difference frequency

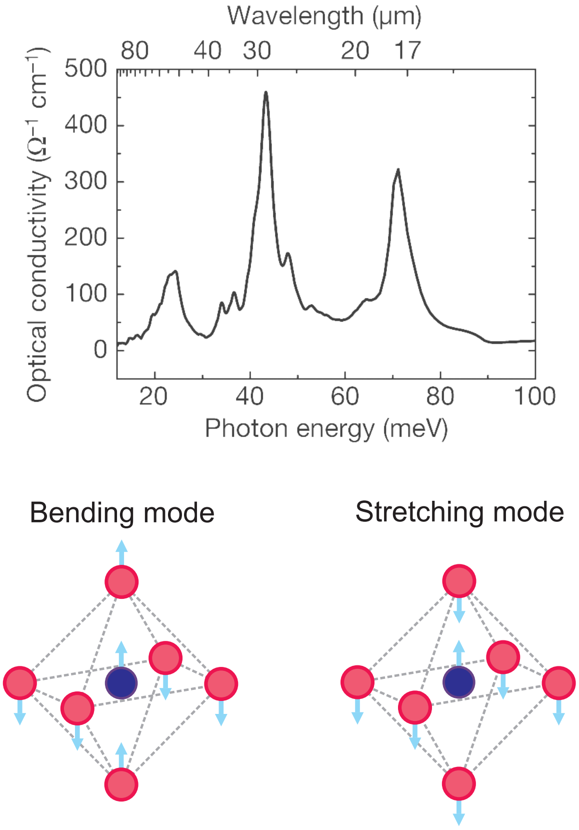

Figure 7.5: Optical conductivity spectrum of $Pr_{0.7}Ca_{0.3}MnO_3$ at 10 K, taken from [204]. Also illustrated are bending and stretching modes of the Mn–O octahedra.

generation (DFG). The non-collinear arrangement allows for spatial filtering of the light, minimising losses due to filters.

The DFG scheme is capable of producing radiation down to around 20 μm (62 meV) with pulse energies of a few microjoule. This makes it ideal as a source to study the response of the highest-lying stretching mode at 71 meV. The pump light generated was then focussed down onto a $Pr_{0.7}Ca_{0.3}MnO_3$ sample with intensities of around 1 mJ cm^{-2}. A doping level of $x = 0.3$ was used to coincide with studies of the photoinduced phase transition already performed at that doping. Henceforth, the term PCMO will only refer to $Pr_{0.7}Ca_{0.3}MnO_3$. The sample was fixed onto a cryostat cold finger, allowing the temperature to be controlled down to a few kelvin.

The second part of the main laser beam was passed into a second OPA, which could be tuned between the visible and the infrared, just as in chapter 5; this constituted the probe

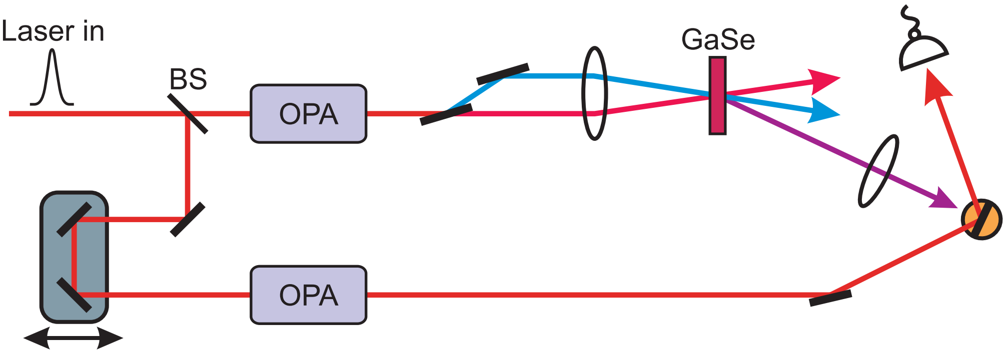

Figure 7.6: Schematic layout for the vibrational control experiment in PCMO. OPA – optical parametric amplifier. BS – beam splitter. The orange circle represents the cryostat cold finger, with the sample (black line) mounted at its centre. The grey-blue box is a delay stage.

beam. Its delay relative to the pump beam was controlled with a delay stage, so that the response to mid-infrared excitation could be mapped out in time.

The pump beam was chopped using a mechanical chopper wheel and reflectance changes to the probe beam were recorded by lock-in detection, all as in chapter 5.

7.4.2 Experimental results

The PCMO sample was held at 30 K and pumped with light resonant to the 71 meV stretching vibration. The reflectance was measured as a function of pump-probe time delay and is shown in figure 7.7(a). A prompt change in reflectance is observed on arrival of the pump, which decays after around 1 ps to a long-lived phase lasting for hundreds of picoseconds, as indicated by the constant change in reflectance at long times. No dependence on pump polarisation was observed in any of the measurements. The reflectance changes observed are qualitatively similar to those seen after excitation at 1.55 eV, with the same dynamics and development of a meta-stable state. In the equilibrium insulating state of PCMO, the insulating gap has size $\Delta = 180\,\mathrm{meV}$ [204]. Crucially, then, the 1.55 eV pump energy is far in excess of the insulating gap size, whereas 71 meV lies below it. This suggests that an ultrafast response that is similar in nature to that formed by above-gap excitation may be induced by pumping below gap.

In order to characterise the photoinduced phase, the reflectance changes were measured across a range of probe energies for the same pump intensity. Figure 7.7(b) summarises

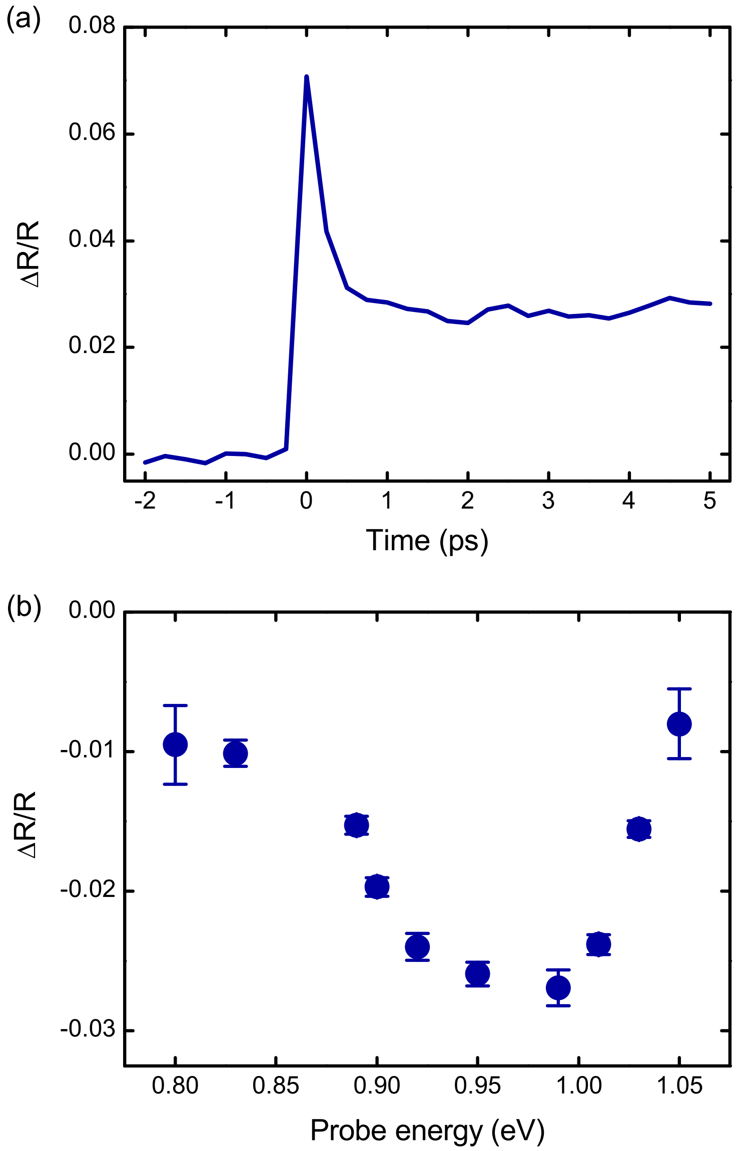

Figure 7.7: Reflectance changes for PCMO after photoexcitation with mid-infrared radiation. (a) Reflectance changes as a function of time after excitation at 71 meV, measured at 0.99 eV (1250 nm). (b) Probe energy dependence of the reflectance changes 1 ps after excitation with 71 meV pulses.

the results obtained in the near-infrared between 1.05 and 0.8 eV, showing the reflectance changes 1 ps after excitation at 71 meV. Additional spectrally resolved measurements were also obtained at higher probe energies by Rini et al. [206]. Overall, a decrease in reflectance is seen for energies between 0.8 and 2 eV, whilst an increase occurs for higher photon energies. This spectrum is consistent with previous results obtained for the photoinduced insulator–metal transition in PCMO [203]. In that study, it was shown that above-band-gap excitation and application of a magnetic field can induce the same spectral features, characterised by a decrease in reflectivity between 0.5 and 1.9 eV and an increase above it. This was attributed to a collapse of the insulating gap present at equilibrium. The direct correlation between the results of figure 7.7(b), combined with those of Rini et al. [206], and the earlier optical study implies that a metallic state is formed promptly as a result of photoexcitation resonant with a lattice vibration of the system.

The response of PCMO to mid-infrared pumping was investigated further by Rini et al. by tuning the pump wavelength across the resonance feature [206]. The reflectance change is maximum when the pump wavelength is resonant with the Mn–O stretching mode, and vanishes as the wavelength is tuned away from it. Conductivity measurements were also carried out by measuring the resistance between gold electrodes fixed to the surface. These showed a five-order-of-magnitude increase in conductivity immediately after excitation, with the change decreasing as the pump was tuned away from resonance [206]. All of this provides further support for the notion of a vibrationally induced ultrafast insulator–metal phase transition.

The results presented in figure 7.7, together with those of Rini et al., show that resonant excitation of the Mn–O phonon mode at 71 meV in PCMO initiates a transition to a meta-stable conducting phase. This happens on femtosecond timescales and persists for nanoseconds. Importantly, this transition does not excite electrons, since the photon energy is below gap, so that the electrons remain in their ground state. Furthermore, since no thermal metallic phase exists for PCMO for any value of doping x, as indicated by figure 7.4, the effect cannot be caused by simple laser heating. Rather, it appears that coherent modulation of the tolerance factor, induced by exciting a vibrational mode of the system, leads to dramatic changes in the electron hopping probability. This demonstrates an alternative mechanism for ultrafast phase transitions in correlated materials, highlighting the important role played by structural effects in these systems.

7.4.3 The next steps

This first experiment demonstrates the possibility of vibrational excitation for driving ultrafast changes in correlated materials. The approach opens the way to understanding the importance of the lattice in a host of interesting and elusive problems, including colossal magnetoresistance and high-temperature superconductivity, where phonons are expected to play a crucial part. The coupling between spin and lattice degrees of freedom also makes the manipulation and control of magnetic states an attractive prospect. Depositing energy directly into specific lattice modes and bypassing the electrons may provide fresh insight into the behaviour of many types of complex material, highlighting the role of the lattice in determining the electronic properties.

However, in order to understand all these effects, there are a few points to consider in moving forward. First, what is the importance of specific modes? Can driving different modes in the system have the same effect or does it differ, and why? Comparing the effects for different modes would help elicit information on the conduction mechanisms in the material and on the role of the structural distortions in the electronic properties more generally. Furthermore, what is the role played by the electric field of the light pulse? What are the sub-cycle distortions caused by the field doing to the electronic structure? These are more long-term goals, but attempting to address them will form the remainder of this chapter.

7.5 Studying Resonant Effects

7.5.1 Laboratory limitations

The measurements carried out in section 7.4 used tabletop sources to produce the light required for studying the highest-lying mode in PCMO. Somewhat serendipitously, the wavelength range afforded by difference frequency generation covers this mode, but stops at around 20 µm (62 meV), making an exploration of the other modes impossible with the available nonlinear optical techniques.

In order to understand the role played by specific structural distortions in ultrafast phase transitions, it is important to be able to study the effects of different modes. This can be achieved by performing experiments in materials which have modes at higher frequencies or by using different sources of light to access lower-frequency modes.

The first route has been explored for the organic one-dimensional Mott insulator (BEDT-TTF)-F_2TCNQ. This compound has phonon modes at 6 μm and 10 μm, which are expected to affect the electronic bandwidth of the system in different ways by altering the electron orbital overlap. By driving these two modes with mid-infrared light from table-top sources, a collapse of the Mott state was found for one mode but not the other, highlighting the different role played by structural distortions in the two cases [207].

However, as can be seen for the manganites in section 7.3, such systems with accessible modes cannot always be found. Free electron lasers offer a way around the limitations of traditional nonlinear techniques, opening up the possibilities for examining other modes of the system.

7.5.2 Free electron lasers

The free electron laser (FEL) is capable of producing tunable radiation over a broad range of wavelengths, from the far-infrared up to X-rays, using a high-energy electron beam as a lasing medium [208–210]. The free electron laser at the superconducting electron linear accelerator with high brilliance and low emittance (FELBE) located at Forschungszentrum Dresden-Rossendorf, Germany, is an FEL operating in the far- to mid-infrared regions [211]. A schematic of the FEL is shown in figure 7.8. The electron beam is generated by a thermionic electron gun and then accelerated by a superconducting linear accelerator. The undulator is a series of magnets whose field direction alternates from section to section, as illustrated in figure 7.8. The magnetic field moves the electrons back and forth in a direction perpendicular to the undulator axis, causing the electrons to emit radiation with a wavelength determined by their energy and the undulator period and gap size. The wavelength of the infrared radiation can thus be tuned by adjusting the undulator gap, for a given period.

The undulator sits in the centre of a resonator consisting of two mirrors whose separation is fixed by the repetition rate of the electron beam, set at 13 MHz. The resonator is tuned to maximise the power output of the FEL. There are two undulators in use at FELBE, which provide almost continuous coverage from 4 to 250 μm [212, 213]. The spectral width of pulses produced by FELBE is typically $\Delta\lambda/\lambda \leqslant 2\%$, depending on the wavelength desired. The

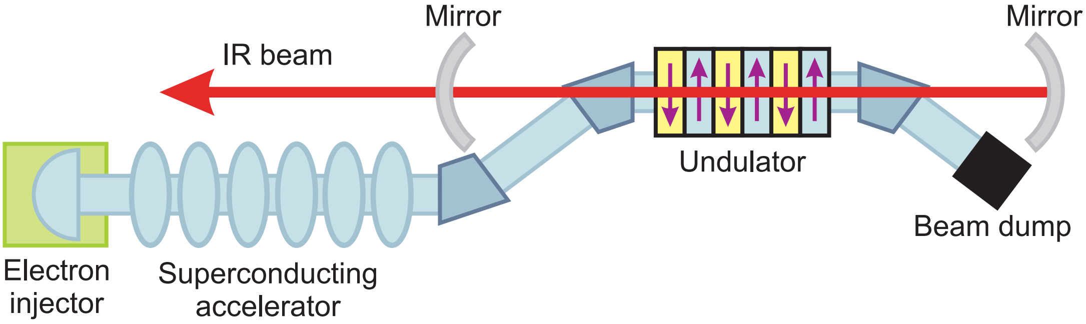

Figure 7.8: Schematic layout of the FEL at FELBE.

pulses are Fourier limited, putting their duration in the range of several picoseconds.

Thus FELBE provides a source of tunable narrowband infrared radiation across a range of wavelengths, making it suitable for studying the role of different phonon modes in vibrational control experiments in PCMO and any number of other complex materials. While it offers narrower bandwidth pulses, which would allow for better understanding of the selectivity of the effects, this naturally comes at the expense of the pulse duration, which is lengthened from the femtosecond to picosecond timescales.

7.5.3 Experiments at FELBE

While excitation of the stretching mode at 71 meV showed an ultrafast insulator–metal phase transition, it is desirable to try to understand what the importance of this particular distortion is. To this end, the FELBE free electron laser could be used to try to excite the two other lower-frequency modes at 23 and 42 meV, corresponding to the Pr/Ca site external mode and the Mn–O–Mn bending mode, respectively. Since conduction in manganites is supposed to take place via double-exchange hopping between manganese and oxygen sites, the bending mode is expected to play an important role in the transport properties, and so an effect similar to that observed for excitation at 71 meV should be seen. However, the lowest-lying external mode does not affect the tolerance factor, leaving the Mn–O bond angle and length unchanged, but moving the Pr/Ca ions relative to the Mn–O octahedra instead. As such, the response is anticipated to be quite different when exciting this mode.

An important technical challenge to overcome in these experiments is concerned with the repetition rate of the FEL. The mid-infrared pulse train has a frequency of 13 MHz, giving a pulse separation of some 77 ns. This is not desirable, since the meta-stable state found in

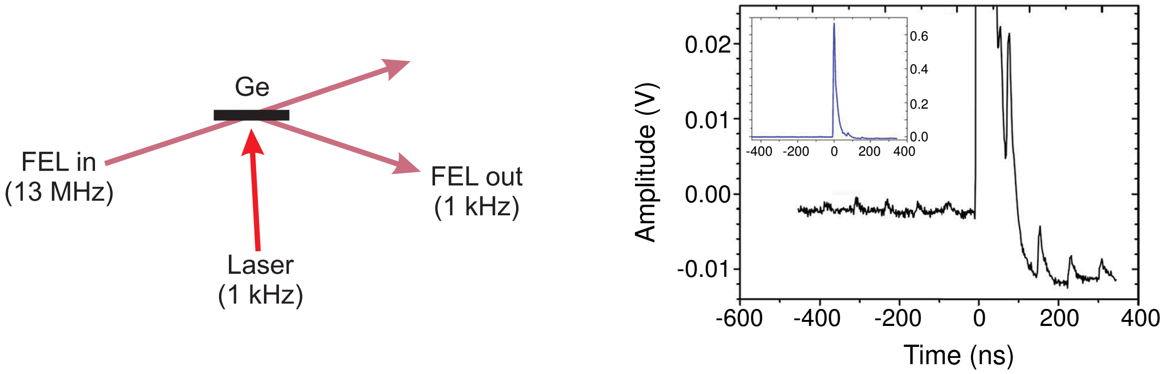

Figure 7.9: Using the optical switch to change the FEL repetition rate. Left: schematic diagram of the switch inputs and outputs. Right: oscilloscope trace showing reflected FEL pulses. The switching laser arrives at 0 ns. The inset shows the full scale of the switched-out pulse for comparison with the unswitched pulses.

the laboratory experiments lasts for some nanoseconds before returning back to equilibrium. Furthermore, the average power of the FEL at the wavelengths of interest is typically on the order of several watts, meaning the laser could potentially heat the sample up. While there is no thermal metallic phase, so that heating is not expected to produce conducting behaviour, the effects of heating with the laser may suppress any transient effects it also induces. As such, it is desirable to first turn down the repetition rate of the FEL to something much lower, increasing the inter-pulse separation and reducing the average power.

This is achieved by using an optical switch, based on laser-generated plasma in germanium [214]. The FEL beam is incident at Brewster's angle onto a germanium plate, such that it is transmitted with minimal reflection. A Nd:YAG amplified laser operating at 1 kHz and 1064 nm is focussed onto the germanium, where it generates an electron-hole plasma. For a sufficiently high plasma density, the optical properties are altered so as to make the germanium reflecting for the FEL. Since the electrons and holes eventually recombine, the effect is only transient; a decay constant of 590 ps has been measured [214]. This means that if the FEL arrives immediately after the Nd:YAG laser pulse, it will be reflected, while for times before and soon after the Nd:YAG pulse, it will be transmitted. Since the laser has a repetition rate of 1 kHz, the reflected pulses will also have a 1 kHz repetition rate, with the remaining pulses blocked after passing through the germanium. This process is shown in figure 7.9. Also shown in this figure is an oscilloscope trace recorded on a HgCdTe detector, sensitive to the mid-infrared wavelengths of the FEL. Ideally, only one pulse would be switched out by the laser; in practice, the plasma is still dense enough to allow for partial switching of some successive pulses. However, as can be seen from the figure and its inset, the ratio between the initial switched pulse and all other pulses is very large, so that the effect of these residual pulses is significantly smaller.

With the switch operational, the FEL repetition rate can be reduced to match the 1 kHz Nd:YAG laser. While the unswitched pulses are not fully suppressed, a contrast ratio of 400:1 for switched to unswitched pulses was found during the experiment. The Nd:YAG laser can also be used to probe the reflectance changes of the PCMO sample following vibrational excitation.

A schematic of the experimental layout for the FEL experiments is shown in figure 7.10. The FEL beam was first sent through a polarisation rotator, consisting of a rotatable periscope. This was designed to optimise the polarisation of the FEL for the optical switch. The unswitched FEL pulses were transmitted through the germanium and blocked by a beam dump. A vacuum chamber similar to that used in chapter 5 was used for the FEL measurements. This design was chosen rather than a more conventional cryostat since it allowed for much smaller focal length optics to be used; this meant that greater pump intensities could be achieved. The Nd:YAG probe beam was made collinear with the pump by passing it through the back of the final pump focussing parabolic mirror. This was necessary as the short focal length mirror crowded the sample. The intensity of the probe beam was monitored using a silicon photodiode, and changes to the reflectance of the sample were measured using lock-in detection. The whole optical table could be enclosed with plastic and purged with nitrogen, which was important to prevent losses of the infrared light due to absorption by water in the air.

7.5.4 Experimental results

As a first feasibility test for using the FEL to drive vibrational excitations, the wavelength was tuned to 17.4 µm (71 meV) to try to repeat the laboratory measurements of section 7.4. The wavelength was then tuned down to 29.4 µm (42 meV), resonant with the bending mode of PCMO. For these initial explorations, the measurements were performed at room temperature, with the intention of cooling down to low temperatures after ironing out any

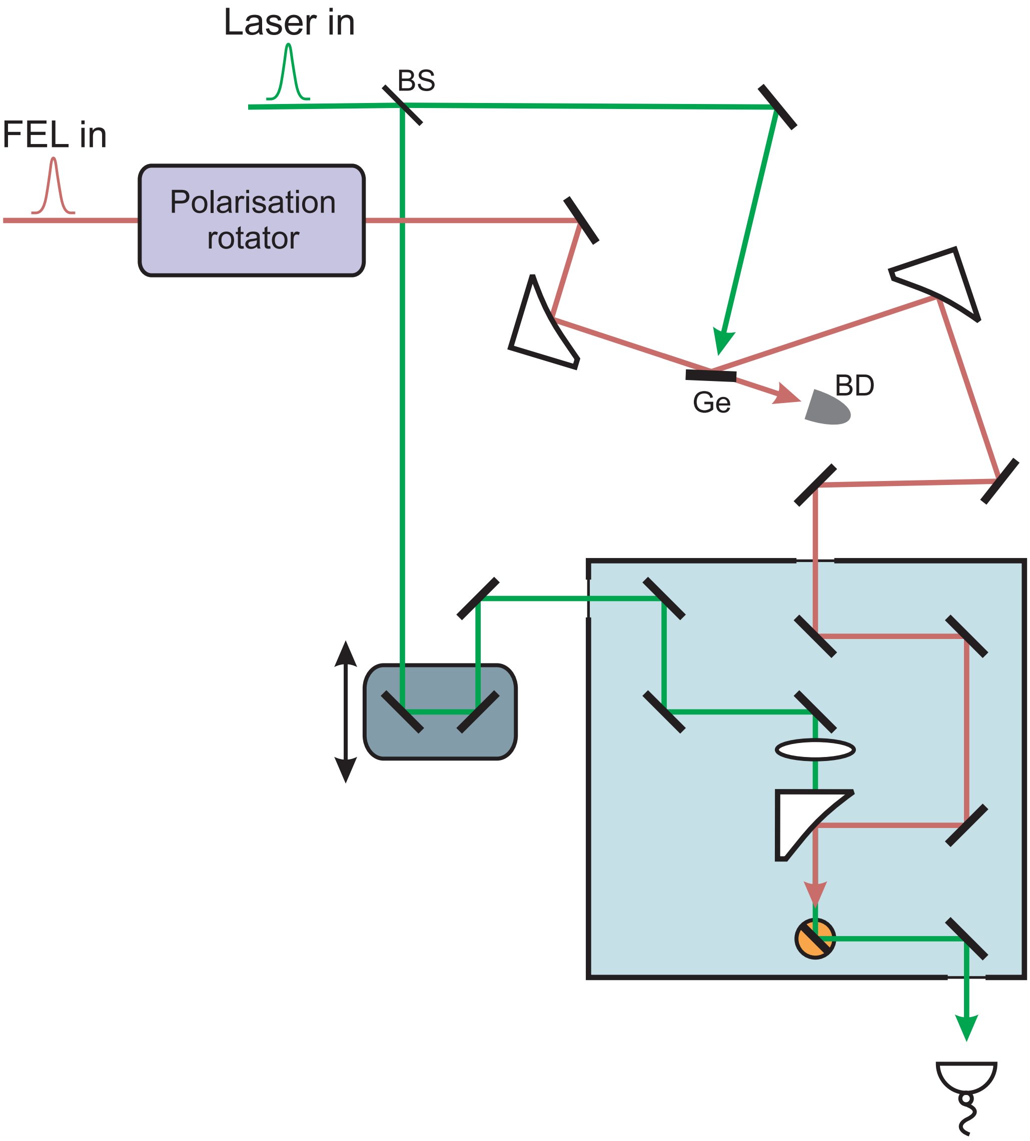

Figure 7.10: Schematic layout for the FELBE experiments. BS – beam splitter. Ge – germanium. BD – beam dump. The orange circle represents the cryostat cold finger. The sample (black line) is mounted to it and can be rotated about an axis perpendicular to the page. The blue-grey box is a delay stage and the light blue box represents the vacuum chamber.

technical issues with using the FEL as a pump source.

The FEL was focussed down to a spot diameter of approximately 300 µm, as measured with a Spiricon infrared camera. The upper limit of intensity for the FEL pulses after the optical switch was estimated as 200 µJ cm^{-2} for the 17.4 µm light, and 820 µJ cm^{-2} at 29.4 µm. The low pulse energies make an accurate determination of the beam intensity at the sample difficult at present, though schemes for calibration are in progress.

The preliminary results obtained by pumping PCMO at 17.4 µm are displayed in figures 7.11(a) and (b). Despite the noise level, a change in reflectance is observed upon arrival of the FEL pump pulse. The probe laser has a pulse duration of ≈ 20 ps, meaning the resulting temporal profile is somewhat different to that observed with the femtosecond sources, although the pump still initiates long-lived reflectance changes. The magnitude of the signal measured 100 ps after excitation shows a roughly linear dependence on the pump intensity. Despite the low intensity achieved with the FEL, a photoinduced response is found, making the FEL a viable source for investigating phonon-induced effects.

The wavelength was then tuned to 29.4 µm; the first results obtained are shown in figures 7.11(c) and (d). As is the case at 17.4 µm, a reflectance change is observed upon excitation by the FEL, leading to a long-lived state. The signals obtained at this wavelength are noisier than those found at the shorter wavelength due to FEL instabilities. However, it is still possible to differentiate the response before and after the pump arrives. This represents the first response from driving the bending mode in this compound.

7.5.5 Further measurements

The results presented from the experiments at FELBE represent the first investigations using this source to study time-dependent phenomena in solids. Much is still to be done to improve the system and understand the nature of the photoinduced dynamics. A better measure for the intensity of the pump pulses is required; currently a scheme using HgCdTe detectors is being implemented. Improvements in FEL stability and optical switch efficiency should also increase the pulse energy and improve the signal-to-noise ratio.

Future measurements will require the cryostat to be used, reducing the temperature of the sample to that used in earlier investigations. This is necessary to optimise the phonon spectrum, reducing broadening introduced by thermal effects. It also allows for a more direct

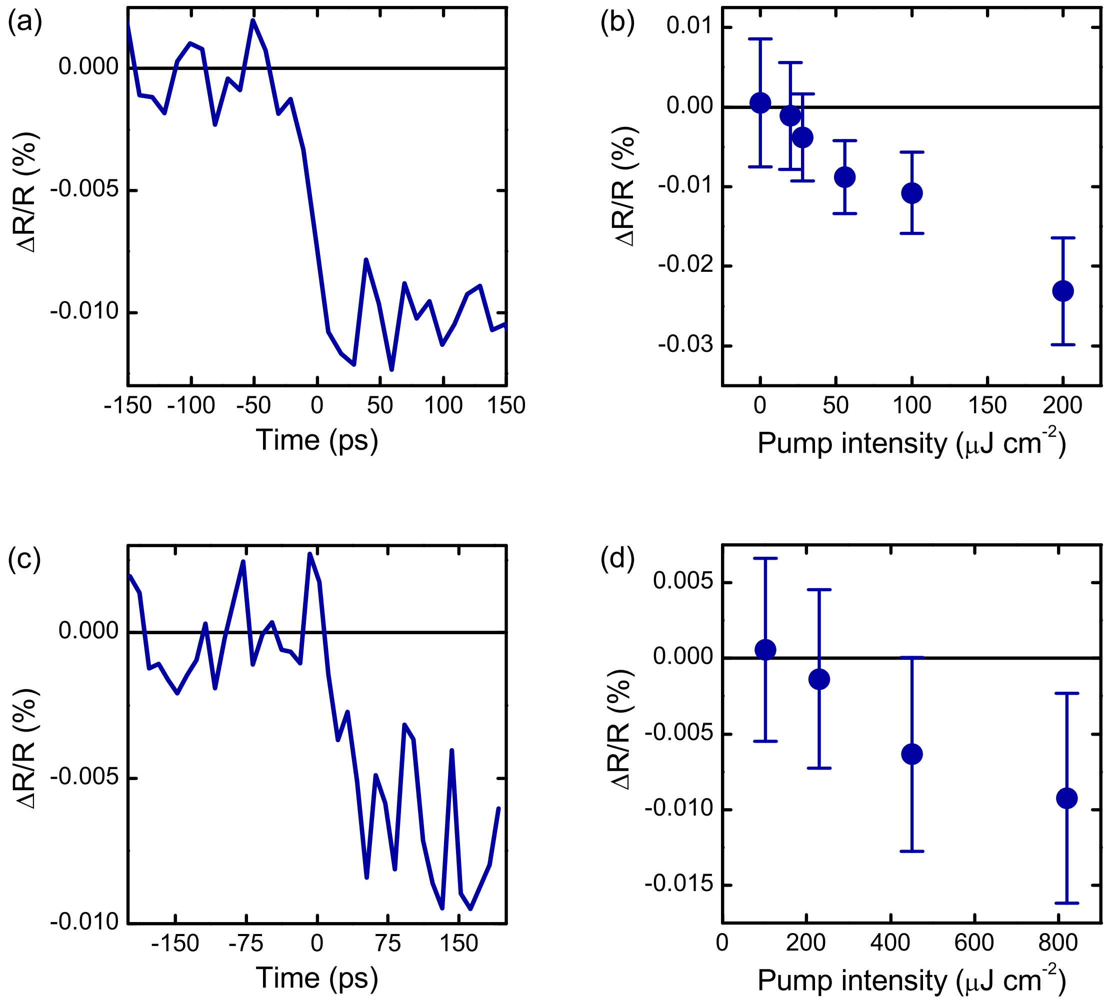

Figure 7.11: Reflectance changes for PCMO after photoexcitation with FEL radiation. (a) and (b): $\Delta R/R$ as a function of time and intensity after excitation at 17.4 μm. (c) and (d): $\Delta R/R$ as a function of time and intensity after excitation at 29.4 μm.

comparison with the laboratory experiments. The tunable narrow bandwidth radiation offered by the FEL means that future experiments should also focus on exploring the resonant nature of the phonon-induced effects in a bid to understand the role of the structural distortion in controlling the conducting properties. The unique characteristic of the FEL is its ability to explore all three main phonons, so that a comparison of the different vibrations is possible. This is important for any future understanding of the nature of ultrafast vibrationally induced phase transitions.

7.6 Field-Resolved Effects

Section 7.4.3 proposed two directions for the field of vibrational control. The first, the exploration of other modes and their role in controlling the electronic bandwidth, was discussed in section 7.5. The second will be briefly discussed in this section.

The idea behind this proposal is to elucidate the importance of the driving electric field when exciting vibrational modes of a complex material. Since the light couples to a structural distortion, it is expected that the field of the pulse may be important to the process as it modulates the ionic bonds. However, the precise nature of the structural modulation remains to be seen.

While DFG is capable of producing infrared radiation resonant with lattice vibrations, this radiation is incoherent in nature, in that the relationship between the carrier phase and the pulse envelope is not well defined from pulse to pulse. This means that for each pulse in the train, the electric field is slightly different and any information concerning the field is lost as the signal is averaged over many pulses.

The carrier–envelope (CE) phase measures the offset between the peak of the electric field and the peak of the pulse envelope. A change in CE phase from pulse to pulse represents the slip of the carrier wave through the pulse envelope. In general, the CE phase evolves as optical pulses propagate through a dispersive medium, where the phase and group velocities are different [215]. This process occurs in mode-locked laser systems, meaning that their CE phase is not stabilised. Instead, it varies by a fixed amount $\Delta\phi_{\mathrm{CE}}$ for each successive pulse. This process is sketched in figure 7.12. If the CE phase was locked for each pump pulse then the driving electric field would always look the same and phase effects may become apparent when dealing with certain phenomena.

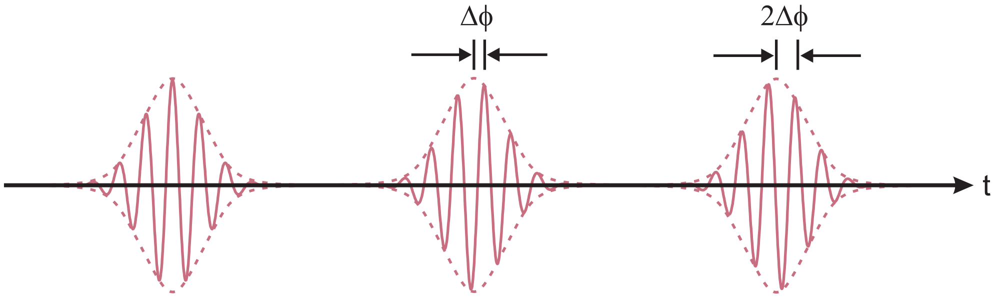

Figure 7.12: Illustration of the carrier-envelope phase evolution from pulse to pulse. The phase offset between pulses changes by an amount $\Delta\phi$.

Techniques exist to stabilise the CE phase of mode-locked laser systems, although these all rely on active feedback mechanisms to correct for the group velocity mis-match in the lasing medium [216]. However, passive stabilisation is also possible using OPAs.

In an OPA, a pump beam amplifies a signal beam, generating an idler beam in the process, as described in chapter 3. It has been shown elsewhere that in parametric amplification the phase of the signal wave is preserved while the beam is amplified [74, 217]. Furthermore, the relationship between the phases ϕ of the pump, signal, and idler is given by

$$\phi_I = \phi_P - \phi_S - \pi/2, \tag{7.2}$$

where I, S, and P represent idler, signal, and pump respectively [217]. If the pump and signal originate from the same laser source then their phases are locked and are related by $\phi_P = \phi_S + \Delta\phi$, where $\Delta\phi$ is constant. From equation (7.2), then, it follows that the idler phase is constant regardless of any CE-phase instability of the laser. This principal has been applied to generate phase-stable infrared light using different frequency components of the same broadband pulse [218].

If two OPAs are driven by the same laser source, it follows that the mutual phase relationship between the signals of the two OPAs should be locked in a similar way to the pump and signal of a single OPA. Then if the signal beams from each OPA are used as the pump and signal in a DFG process, the idler generated from them should have a constant phase for every pulse. This would provide a source of tunable mid-infrared light, as described in chapter 3, except with CE-phase-stabilised pulses.

Such a scheme was employed to generate CE-phase-stable light by DFG in GaSe. The resulting mid-infrared radiation was then detected using electro-optic sampling in a second

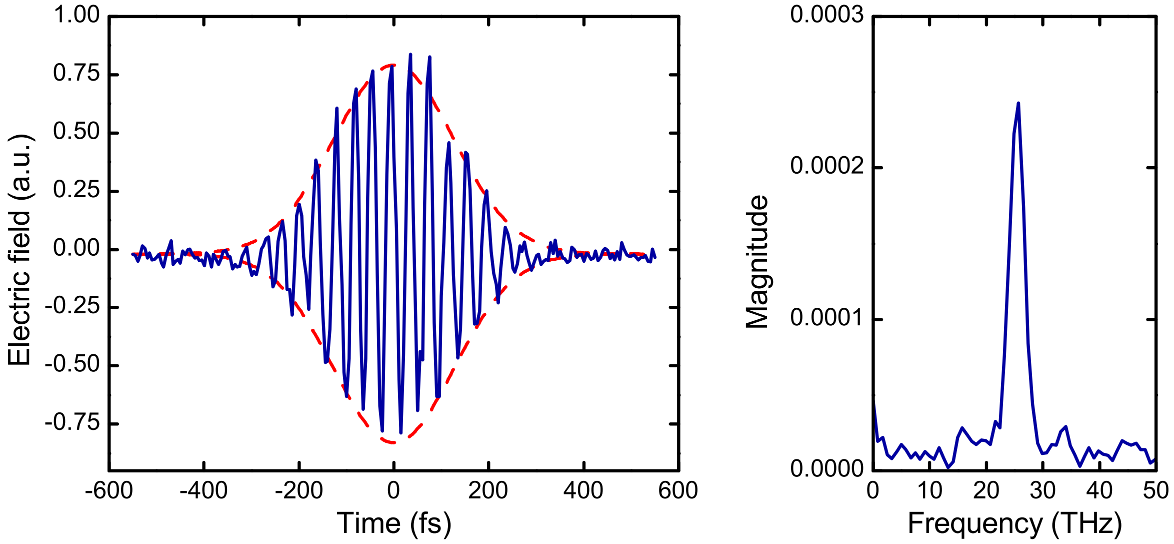

Figure 7.13: A carrier-envelope phase stable pulse generated by DFG between two OPAs. The dashed red lines represent a Gaussian envelope with FWHM ≈ 300 fs. The Fourier transform spectrum is shown on the right. The central frequency is 25.5 THz and the bandwidth is $\Delta\nu = 3\,\text{THz}$.

GaSe crystal, using the same apparatus described in chapter 4. This field-resolved detection of the electric field serves as proof of its phase stability: if the CE phase were not stabilised then the field would slip through the envelope and appear slightly different for each pulse, and the effect of averaging over successive pulses would wash out any field-related effects, leaving only an effect characterising the pulse envelope.

Pulses were generated with typical energies of 0.5 to 2 μJ for wavelengths between 10 and 18 μm. Figure 7.13 shows a CE-phase-stable pulse generated at 11.8 μm (25.5 THz). The stability of the CE phase offset was found to drift slowly over timescales of about an hour, but can be corrected by introducing fused silica wedges into one of the OPA paths before the difference frequency mixing takes place [219].

CE-phase-stable light generated in this way is expected to facilitate the study of field-resolved effects in vibrational control experiments. Currently, investigation is underway in applying these mid-infrared pulses to manganites, where the presence or absence of field-induced effects should reveal important information about the phonon-induced phase transition [220]. Furthermore, their application to organic compounds, where work has already been carried out using non-stabilised pulses, should demonstrate interesting phase-dependent effects as the electron wavefunctions are coherently modulated across the molecule [207].

7.7 Summary

This chapter has tried to offer a brief overview of an emerging new field of ultrafast science, in which light is coupled directly to structural modes of a system without electronic excitation, rather than putting energy directly into the electronic degree of freedom. A first set of experiments showed that it is possible to induce an insulator–metal phase transition by resonant excitation of a stretching mode in a manganite system, presenting exciting new opportunities for understanding the important effect the lattice can have on influencing the electronic properties. The use of FELs can open up the available spectrum for resonant excitation, allowing the role of different modes to be explored across a range of different structures. At the same time, the generation of CE-phase-stable pulses will allow field-dependent effects to be monitored as the structure is modulated.

Subsequent to the first experiment in PCMO, other measurements have shown vibrationally induced melting of charge order [221], control of the Mott criterion in organic insulators [207], the generation of coherent phonons [220], and the creation of a transient superconducting phase in a doped cuprate [222]. The ability to initiate ultrafast dynamics by coupling to phonons rather than electrons offers much promise in untangling the role of different degrees of freedom in strongly correlated materials and will become an important means to understand a variety of problems, from magnetic and electronic ordering to high-temperature superconductivity.

Chapter 8

Conclusion and Future Directions

8.1 Overview

This thesis has used a variety of ultrafast spectroscopic techniques to understand and characterise photoinduced effects in complex materials. An understanding of the response of a system across a range of energies is essential to determining its properties, be it an equilibrium state or a transient photoinduced phase. Photoexcitation of solids enables the interactions of different components to be separated, making ultrafast effects an important element of any material study. In addition, understanding these effects can lead to control of them, which has many potential technologically important applications. The broadband spectroscopic studies presented in this work have combined photon energies from 1 meV up to 20 eV as ultrafast probes of the transient state of $\mathrm{TaS_2}$ induced by light at 1 and 1.5 eV. Meanwhile, the principal of vibrational control in manganites was introduced, which demonstrates a new way to understand and control the lattice in a variety of problems.

8.1.1 Tantalum disulphide

The photoinduced phase of $1T$-$\mathrm{TaS_2}$ was explored using two approaches: broadband optical spectroscopy to study the collective response of the system, and angle-resolved photoemission spectroscopy to understand the single particle behaviour and electronic band structure. The results of these investigations were described in chapters 5 and 6, respectively.

A time-resolved THz time-domain spectroscopy system was developed to allow for field-resolved studies at the lowest energies. By preserving phase information in the pulses, a direct reconstruction of the optical properties of a solid is possible as they evolve in response to photoexcitation. This reveals information on long-range transport properties and can also illuminate the response of phonon modes, allowing for explicit observations of both electronic and structural effects in time in a single measurement. In TaS_2, the complex optical conductivity was recovered as a function of time. It was found that the melting of the Mott gap leads to an increase in low-frequency conductivity, although not to the value found at the thermal phase transition. Additionally, transient asymmetries were observed in the phonon resonances, suggesting a coupling between these low-energy structural modes and a higher-energy electronic excitation.

These low-frequency techniques were complemented by additional higher-frequency approaches. The output of a near-infrared optical parametric amplifier was extended into the mid-infrared region using nonlinear optical techniques. This provided a femtosecond source of probe light over a broad energy range. Whilst it lacks the phase information afforded by THz spectroscopy, it reveals a lot about coherently generated phonons and about the dynamics in a region not normally covered in pump-probe spectroscopy. Studies of the photoinduced reflectance changes in the mid-infrared to visible regions revealed the excitation of the charge density wave amplitude mode at 2.4 THz. This suggests that the charge density wave distortion is only partially undone by photoexcitation, in agreement with earlier studies [28, 71]. Moreover, the reflectance revealed the emergence of a new broad resonance at 155 meV. Given the strong electron-phonon coupling present in this material, this feature was interpreted as a polaron band.

These two methods can characterise the dynamical behaviour of photoinduced phases across a broad region of the spectrum, allowing for insight into ultrafast processes in enormous detail. In addition, a time- and angle-resolved photoemission spectroscopy system was developed, using high harmonic generation to produce photons at 20.8 eV with 50 fs resolution. Such a system enables the single particle response to be studied, capturing the dynamics of electrons with momentum specificity, and mapping out the evolution of the band structure after photoexcitation across large regions of the Brillouin zone. By studying the earliest times of the photoinduced phase transition in TaS_2, the collapse of the Mott gap could be directly observed. Concomitantly, structural relaxation was seen to occur on timescales connected to the charge density wave, indicating a partial unfolding of the Brillouin zone back towards the undistorted higher symmetry phase.

Bringing all these elements together presents a clearer view of the photoinduced phase of TaS_2. This phase is found to be qualitatively different from any of the thermal phases: the Mott gap is lost and conductivity is found to increase, though it remains lower than in the equilibrium metallic phase; the charge-density-wave structural distortion relaxes, but only partly, with the symmetry of the low-temperature phase remaining unchanged; and the transport properties are strongly polaronic, with a polaron band appearing at 155 meV.

8.1.2 Vibrational excitation

Although the majority of the work presented in this thesis is connected to probing techniques, a new type of pumping technique was introduced in chapter 7. This chapter dealt with the idea of vibrational excitation, in which light is directly coupled to the structural modes of a complex material, rather than the electronic excitations. A first set of experiments was presented, in which an insulator–metal phase transition was initiated by modulation of a stretching vibration in a perovskite manganite. This result opens up a new field of ultrafast phase transition, in which electrons are left in their ground state but the lattice is excited. This offers the potential to understand and control a number of processes in strongly correlated electron materials where the lattice plays an important role in the electronic properties.

Following on from this, the potential application of FELs was described, accompanied by some preliminary findings. The aim of these continuing measurements is to investigate other phonon modes in the system and understand the role they play in controlling the conducting properties. Finally, the generation of carrier–envelope phase stable radiation was introduced and demonstrated. This may reveal new field-induced effects in complex materials, which have hitherto been unobservable.

8.2 Looking Ahead

8.2.1 Tantalum disulphide

While the spectroscopic techniques presented in this thesis cover a broad spectral range and go a long way towards characterising the salient features of the photoinduced phase of TaS_2, there is still room for further exploration.

Broadening the THz spectrum beyond 2.8 THz would provide a more complete study of the structural modes of TaS_2, including the anomalous mode identified at 6.2 THz, which is believed to be connected to both structural and electronic changes at the thermal phase transition [60]. At higher frequencies, a finer selection of probe wavelengths would yield more detailed information on the polaron band, which may be connected to the loss and recovery of the Mott gap.

There a number of additional investigations which may offer further information on the photoinduced phase. Few-femtosecond pulses could help further differentiate the electronic and structural processes in the photoinduced phase of TaS_2, where the melting of both Mott and charge-density-wave gaps cannot be distinguished with longer pulses. Also, tuning of the pump photon energy could test the proposal of Perfetti et al. [28] that the photoinduced phase transition originates from electronic temperature effects.

8.2.2 Vibrational excitation

The field of ultrafast vibrationally induced phenomena is still very fresh and offers many possibilities for studying condensed matter systems. Going forward, it will be important to start applying the kinds of spectroscopic technique used in this thesis to characterise the phases induced by driving structural effects. This is important not only to understand their behaviour but also to compare it to transient phases induced by electronic excitations and look for differences between the two. This will help in understanding the competition between electrons and lattice and how this determines the macroscopic properties of the system. Using photoemission spectroscopy will play a key role in this process, since it provides direct measurements of the band structure which can be compared easily to theoretical predictions.

In terms of the initial measurements presented at the end of chapter 7, there is clearly much still to be done. The FEL experiments are still in an early stage of development. However, if successful, these measurements promise to provide much insight into the role of different types of structural excitation in influencing the electronic properties of materials. Furthermore, the effects of carrier–envelope-phase-stable radiation in these transitions needs to be considered, since it offers some interesting prospects for new phases and coherent control.

Many new effects are being observed using vibrational excitation [220, 221], including control of Mott insulators [207] and the induction of cooperative phases such as superconductivity [222]. The real challenge now is to start characterising and understanding these states on a number of different levels. This will require the marriage of ultrafast spectroscopic techniques, such as those presented here, and these new methods for excitation and control.

8.2.3 Further afield

As developments in ultrafast technology continue apace, the condensed matter scientist is increasingly spoilt for choice in the number of tools at his or her disposal. The field of ultrafast science is constantly expanding into new territory, as pulses get ever shorter and the available energy scales expand. These advances usher in fresh promises in terms of understanding the behaviour of matter.

Two questions lie at the heart of this progression: what does light reveal about the different phases of materials, and can light be used to control these states and to create new ones? Controlling material properties has been a long-standing goal of solid state physics, and using pulses of light has opened up avenues for transient and switchable behaviours unattainable with more traditional techniques. Future possibilities include the control of magnetism or superconductivity; if light can be used to coherently control the spin state of a lattice, or generate macroscopic condensed states, then this would pave the way for a variety of exciting technological applications.

The introduction of new spectroscopic techniques to the realm of the ultrafast is important for the future characterisation of these controlled states and also to the broader understanding of complex materials. The methods used in this thesis are making great strides towards this, but it is necessary to bring other advancements into play.

Much as Muybridge's images of horses and Victorian women were able to capture the motion of everyday objects, so now are femtosecond X-ray and electron diffraction techniques on the verge of capturing the motion of atoms [223]. Continuing improvements in free electron lasers also promise snapshots of atomic motion on the shortest timescales and of the smallest and most complex structures [224, 225]. Such developments bring the advent of the 'molecular movie' ever closer, enabling direct observations of lattice dynamics as phase transitions take place. Ultrafast X-ray techniques also bring the ability to understand electron spin and orbital dynamics [27, 226], which are vital to the understanding of magnetic phenomena.

It is also important to understand the electronic dynamics, as discussed in this thesis. Time-resolved photoemission is a powerful tool for doing this, though it is still in its infancy. The band structure measurements it provides can serve as a basis for theories of complex materials and photoinduced phenomena which are still poorly understood. Moreover, as pulses shrink down to the attosecond regime, the ability to observe charge transfer processes, unveiling the precise motion of electrons through a material, is fast approaching [25, 182].

Ultimately, the combination of direct structural characterisation and a full determination of the optical properties will provide a rigorous and comprehensive view of all aspects of the dynamics of many intriguing materials. This deep understanding will also be important when considering control and optimisation of their properties. Ultrafast spectroscopies are vital for the study of all manner of materials, from low-dimensional organic compounds, to high-temperature superconducting cuprates and pnictides, where the complex interplay between different degrees of freedom leads to exciting yet elusive behaviour.

8.3 Final Remarks

The combination of broadband spectroscopic techniques presented here provides the necessary means for a necessary means for a fuller understanding of photoinduced phenomena, which cannot be achieved by looking at small spectral regions in isolation. It has been the aim of this thesis to push these tools forward and to provide a richer characterisation of the photoinduced phases in complex materials, focussing here on $1T$-TaS_2. Future developments offer a number of exciting technical challenges and will ultimately enhance the comprehension and control of these exotic materials. A full determination of structural and electronic dynamics is only achievable by bringing multiple tools to bear, and looking at how the system behaves as a whole; the more pieces of the jigsaw are put together, the clearer the picture becomes.

Bibliography

[1] J. Hecht. *Beam: The Race to Make the Laser* (Oxford University Press, USA, 2005).

[2] "Electronics: the death ray next?". *Newsweek* page 78 (1960).

[3] J. Baar. "Death ray visualised as H-bomb successor". *Washington Post and Times Herald* page A8 (1958).

[4] T. H. Maiman. Stimulated optical radiation in ruby. *Nature* **187**, 493 (1960).

[5] J. Hecht. A short history of laser development. *Applied Optics* **49**, F99 (2010).

[6] E. Muybridge. *'Plate Number 156. Jumping; running straight high jump'* (1887). Collotype on paper, 18 7/16 x 23 1/4 inches. Corcoran Gallery of Art, Washington DC. Museum Purchase, 1887. 87.7.156.

[7] E. Muybridge. *Muybridge's Complete Human and Animal Locomotion* (Dover Publications, 1979).

[8] Nobel prize website (2010). `http://nobelprize.org`.

[9] N. F. Mott. The basis of the electron theory of metals, with special reference to the transition metals. *Proceedings of the Physical Society. Section A* **62**, 416 (1949).

[10] E. Wigner. On the interaction of electrons in metals. *Physical Review* **46**, 1002 (1934).

[11] L. N. Cooper. Bound electron pairs in a degenerate Fermi gas. *Physical Review* **104**, 1189 (1956).

[12] M. Imada, A. Fujimori, and Y. Tokura. Metal-insulator transitions. *Reviews of Modern Physics* **70**, 1039 (1998).

[13] J. Orenstein and G. L. Baker. Photogenerated gap states in polyacetylene. *Physical Review Letters* **49**, 1043 (1982).

[14] C. V. Shank, et al. Picosecond dynamics of photoexcited gap states in polyacetylene. *Physical Review Letters* **49**, 1660 (1982).

[15] M. C. Beard, G. M. Turner, and C. A. Schmuttenmaer. Transient photoconductivity in GaAs as measured by time-resolved terahertz spectroscopy. *Physical Review B* **62**, 15764 (2000).

[16] G. Yu, et al. Transient photoinduced conductivity in single crystals of $YBa_2Cu_3O_{6.3}$: "photodoping" to the metallic state. *Physical Review Letters* **67**, 2581 (1991).

[17] S. Koshihara, et al. Photoinduced valence instability in the organic molecular compound tetrathiafulvalene-p-chloranil (TTF-CA). *Physical Review B* **42**, 6853 (1990).

[18] A. Cavalleri, et al. Femtosecond structural dynamics in VO_2 during an ultrafast solid-solid phase transition. *Physical Review Letters* **87**, 237401 (2001).

[19] K. Sokolowski-Tinten, et al. Femtosecond X-ray measurement of coherent lattice vibrations near the Lindemann stability limit. *Nature* **422**, 287 (2003).

[20] A. Cavalleri, et al. Evidence for a structurally-driven insulator-to-metal transition in VO_2 : A view from the ultrafast timescale. *Physical Review B* **70**, 161102 (2004).

[21] M. Chollet, et al. Gigantic photoresponse in 1/4-filled-band organic salt (EDO-TTF)$_2$PF$_6$. *Science* **307**, 86 (2005).

[22] K. Miyano, T. Tanaka, Y. Tomioka, and Y. Tokura. Photoinduced insulator-to-metal transition in a perovskite manganite. *Physical Review Letters* **78**, 4257 (1997).

[23] D. Polli, et al. Coherent orbital waves in the photo-induced insulator–metal dynamics of a magnetoresistive manganite. *Nature Materials* **6**, 643 (2007).

[24] S. Wall, D. Prabhakaran, A. T. Boothroyd, and A. Cavalleri. Ultrafast coupling between light, coherent lattice vibrations, and the magnetic structure of semicovalent $LaMnO_3$. *Physical Review Letters* **103**, 097402 (2009).

[25] A. L. Cavalieri, et al. Attosecond spectroscopy in condensed matter. *Nature* **449**, 1029 (2007).

[26] A. Cavalleri, et al. Band-selective measurements of electron dynamics in VO_2 using femtosecond near-edge X-ray absorption. *Physical Review Letters* **95**, 067405 (2005).

[27] M. Rini, et al. Transient electronic structure of the photoinduced phase of $Pr_{0.7}Ca_{0.3}MnO_3$ probed with soft X-ray pulses. *Physical Review B* **80**, 155113 (2009).

[28] L. Perfetti, et al. Time evolution of the electronic structure of $1T$-TaS_2 through the insulator-metal transition. *Physical Review Letters* **97**, 067402 (2006).

[29] F. Schmitt, et al. Transient electronic structure and melting of a charge density wave in $TbTe_3$. *Science* **321**, 1649 (2008).

[30] J. A. Wilson and A. D. Yoffe. The transition metal dichalcogenides: discussion and interpretation of the observed optical, electrical and structural properties. *Advances in Physics* **18**, 193 (1969).

[31] J. A. Wilson, F. J. Di Salvo, and S. Mahajan. Charge-density waves in metallic, layered, transition-metal dichalcogenides. *Physical Review Letters* **32**, 882 (1974).

[32] S. Uchida and S. Sugai. Infrared and Raman studies on commensurate CDW states in transition metal dichalcogenides. *Physica B* **105**, 393 (1981).

[33] S. Sugai, K. Murase, S. Uchida, and S. Tanaka. Comparison of the soft modes in tantalum dichalcogenides. *Physica B* **105**, 405 (1981).

[34] B. Dardel, et al. Spectroscopic signatures of phase transitions in a charge-density-wave system: $1T$-TaS_2. *Physical Review B* **46**, 7407 (1992).

[35] J. Demsar, L. Forró, H. Berger, and D. Mihailovic. Femtosecond snapshots of gap-forming charge-density-wave correlations in quasi-two-dimensional dichalcogenides $1T$-TaS_2 and $2H$-TaSe_2. *Physical Review B* **66**, 041101 (2002).

[36] F. Clerc, et al. Fermi surface of layered compounds and bulk charge density wave systems. *Journal of Physics: Condensed Matter* **19**, 355002 (2007).

[37] L. Perfetti, et al. Femtosecond dynamics of electronic states in the Mott insulator $1T$-TaS_2 by time resolved photoelectron spectroscopy. *New Journal of Physics* **10**, 053019 (2008).

[38] B. Sipos, et al. From Mott state to superconductivity in $1T$-TaS_2. *Nature Materials* **7**, 960 (2008).

[39] J. A. Wilson, F. J. D. Salvo, and S. Mahajan. Charge-density waves and superlattices in the metallic layered transition metal dichalcogenides. *Advances in Physics* **24**, 117 (1975).

[40] F. J. Di Salvo. Charge density waves in layered compounds. *Surface Science* **58**, 297 (1976).

[41] R. L. Withers and J. A. Wilson. An examination of the formation and characteristics of charge-density waves in inorganic materials with special reference to the two- and one-dimensional transition-metal chalcogenides. *Journal of Physics C: Solid State Physics* **19**, 4809 (1986).

[42] P. Fazekas and E. Tosatti. Charge carrier localization in pure and doped $1T$-TaS_2. *Physica B* **99**, 183 (1980).

[43] S. van Smaalen. The Peierls transition in low-dimensional electronic crystals. *Acta Crystallographica Section A Foundations of Crystallography* **61**, 51 (2004).

[44] G. Grüner. *Density Waves in Solids.* Frontiers in Physics (Perseus Publishing, 1994).

[45] R. E. Peierls. *Quantum Theory of Solids* (Oxford University Press, 1955).

[46] G. Grüner. The dynamics of charge-density waves. *Reviews of Modern Physics* **60**, 1129 (1988).

[47] A. M. Gabovich and A. I. Voitenko. Superconductors with charge- and spin-density waves: theory and experiment (review). *Low Temperature Physics* **26**, 305 (2000).

[48] A. M. Gabovich, A. I. Voitenko, J. F. Annett, and M. Ausloos. Charge- and spin-density-wave superconductors. *Superconductor Science and Technology* **14**, R1 (2001).

[49] H. Schäfer, et al. Disentanglement of the electronic and lattice parts of the order parameter in a 1D charge density wave system probed by femtosecond spectroscopy. *Physical Review Letters* **105**, 066402 (2010).

[50] J. H. D. Boer and E. J. W. Verwey. Semi-conductors with partially and with completely filled $3d$-lattice bands. *Proceedings of the Physical Society* **49**, 59 (1937).

[51] N. F. Mott and R. Peierls. Discussion of the paper by de Boer and Verwey. *Proceedings of the Physical Society* **49**, 72 (1937).

[52] J. Hubbard. Electron correlations in narrow energy bands. II. The degenerate band case. *Proceedings of the Royal Society of London. Series A. Mathematical and Physical Sciences* **277**, 237 (1964).

[53] A. Thompson, R. F. Gamble, and J. F. Revelli. Transitions between semiconducting and metallic phases in $1T$-TaS$_2$. *Solid State Communications* **9**, 981 (1971).

[54] P. Fazekas and E. Tosatti. Electrical, structural and magnetic properties of pure and doped $1T$-TaS$_2$. *Philosophical Magazine Part B* **39**, 229 (1979).

[55] J. van Landuyt, G. van Tendeloo, and S. Amelincky. Electron diffraction study of inter- and intrapolytypic phase transitions in transition metal dichalcogenides. I. Electron diffraction patterns. *Physica Status Solidi (A)* **26**, 359 (1974).

[56] T. Pillo, et al. Remnant Fermi surface in the presence of an underlying instability in layered $1T$-TaS$_2$. *Physical Review Letters* **83**, 3494 (1999).

[57] F. Clerc, et al. Lattice-distortion-enhanced electron-phonon coupling and Fermi surface nesting in $1T$-TaS$_2$. *Physical Review B* **74**, 155114 (2006).

[58] A. S. Barker, J. A. Ditzenberger, and F. J. DiSalvo. Infrared study of the electronic instabilities in tantalum disulfide and tantalum diselenide. *Physical Review B* **12**, 2049 (1975).

[59] A. R. Beal, H. P. Hughes, and W. Y. Liang. The reflectivity spectra of some group VA transition metal dichalcogenides. *Journal of Physics C: Solid State Physics* **8**, 4236 (1975).

[60] L. Gasparov, et al. Phonon anomaly at the charge ordering transition in $1T$-TaS$_2$. *Physical Review B* **66**, 094301 (2002).

[61] J. R. Duffey, R. D. Kirby, and R. V. Coleman. Raman scattering from $1T$-TaS$_2$. *Solid State Communications* **20**, 617 (1976).

[62] A. Spijkerman, et al. X-ray crystal-structure refinement of the nearly commensurate phase of $1T$-TaS$_2$ in $(3 + 2)$-dimensional superspace. *Physical Review B* **56**, 13757 (1997).

[63] R. E. Thomson, B. Burk, A. Zettl, and J. Clarke. Scanning tunneling microscopy of the charge-density-wave structure in $1T$-TaS$_2$. *Physical Review B* **49**, 16899 (1994).

[64] N. V. Smith, S. D. Kevan, and F. J. DiSalvo. Band structures of the layer compounds $1T$-TaS$_2$ and $2H$-TaSe$_2$ in the presence of commensurate charge-density waves. *Journal of Physics C: Solid State Physics* **18**, 3175 (1985).

[65] K. Rossnagel and N. V. Smith. Spin-orbit coupling in the band structure of reconstructed $1T$-TaS$_2$. *Physical Review B* **73**, 073106 (2006).

[66] J. A. Wilson. Questions concerning the form taken by the charge-density wave and the accompanying periodic-structural distortions in $2H$-TaSe$_2$, and closely related materials. *Physical Review B* **17**, 3880 (1978).

[67] B. Dardel, et al. Temperature-dependent pseudogap and electron localization in $1T$-TaS$_2$. *Physical Review B* **45**, 1462 (1992).

[68] J. J. Kim, W. Yamaguchi, T. Hasegawa, and K. Kitazawa. Observation of Mott localization gap using low temperature scanning tunneling spectroscopy in commensurate $1T$-TaSa$_2$. *Physical Review Letters* **73**, 2103 (1994).

[69] Y. Toda, K. Tateishi, and S. Tanda. Anomalous coherent phonon oscillations in the commensurate phase of the quasi-two-dimensional $1T$-TaS$_2$ compound. *Physical Review B* **70**, 033106 (2004).

[70] T. Onozaki, Y. Toda, S. Tanda, and R. Morita. Coherent double-pulse excitation of charge-density-wave oscillation. *Japanese Journal of Applied Physics* **46**, 870 (2007).

[71] M. Eichberger, et al. Ultrafast order parameter melting in a 2-D charge density wave $1T$-TaS$_2$ probed by femtosecond electron diffraction. In *International Conference on Ultrafast Phenomena*, OSA Technical Digest (CD), page MA2 (Optical Society of America, 2010).

[72] D. E. Spence, P. N. Kean, and W. Sibbett. 60-fsec pulse generation from a self-mode-locked Ti:sapphire laser. *Optics Letters* **16**, 42 (1991).

[73] G. Cerullo and S. De Silvestri. Ultrafast optical parametric amplifiers. *Review of Scientific Instruments* **74**, 1 (2003).

[74] R. W. Boyd. *Nonlinear Optics* (Academic Press, 2003), 2nd edition.

[75] R. L. Fork, et al. Femtosecond white-light continuum pulses. *Optics Letters* **8**, 1 (1983).

[76] A. L. Gaeta. Catastrophic collapse of ultrashort pulses. *Physical Review Letters* **84**, 3582 (2000).

[77] J.-C. Diels and W. Rudolph. *Ultrashort Laser Pulse Phenomena: Fundamentals, Techniques, and Applications on a Femtosecond Time Scale (Optics and Photonics Series)* (Academic Press, 1996).

[78] P. B. Allen. Theory of thermal relaxation of electrons in metals. *Physical Review Letters* **59**, 1460 (1987).

[79] J. Shah. *Ultrafast Spectroscopy of Semiconductors and Semiconductor Nanostructures (Springer Series in Solid-State Sciences)* (Springer, 1999), 2nd edition.

[80] W. H. Knox, et al. Femtosecond carrier thermalization in dense Fermi seas. *Physical Review Letters* **61**, 1290 (1988).

[81] S. D. Brorson, et al. Femtosecond room-temperature measurement of the electron-phonon coupling constant γ in metallic superconductors. *Physical Review Letters* **64**, 2172 (1990).

[82] N. W. Ashcroft and N. D. Mermin. *Solid State Physics* (Brooks Cole, 1976), 1st edition.

[83] K. A. Nelson, D. D. Dlott, and M. D. Fayer. Excited state dynamics in pure molecular crystals: perylene and the excimer problem. *Chemical Physics Letters* **64**, 88 (1979).

[84] M. Hase and M. Kitajima. Interaction of coherent phonons with defects and elementary excitations. *Journal of Physics: Condensed Matter* **22**, 073201 (2010).

[85] H. J. Zeiger, et al. Theory for displacive excitation of coherent phonons. *Physical Review B* **45**, 768 (1992).

[86] G. A. Garrett, T. F. Albrecht, J. F. Whitaker, and R. Merlin. Coherent THz phonons driven by light pulses and the Sb problem: What is the mechanism? *Physical Review Letters* **77**, 3661 (1996).

[87] J. Demsar, K. Biljaković, and D. Mihailovic. Single particle and collective excitations in the one-dimensional charge density wave solid $K_{0.3}MoO_3$ probed in real time by femtosecond spectroscopy. *Physical Review Letters* **83**, 800 (1999).

[88] K. Ishioka, et al. Ultrafast electron-phonon decoupling in graphite. *Physical Review B* **77**, 121402 (2008).

[89] D. Auston. Impulse response of photoconductors in transmission lines. *IEEE Journal of Quantum Electronics* **19**, 639 (1983).

[90] D. H. Auston, K. P. Cheung, and P. R. Smith. Picosecond photoconducting Hertzian dipoles. *Applied Physics Letters* **45**, 284 (1984).

[91] N. Katzenellenbogen and D. Grischkowsky. Efficient generation of 380 fs pulses of THz radiation by ultrafast laser pulse excitation of a biased metal-semiconductor interface. *Applied Physics Letters* **58**, 222 (1991).

[92] A. Nahata, A. S. Weling, and T. F. Heinz. A wideband coherent terahertz spectroscopy system using optical rectification and electro-optic sampling. *Applied Physics Letters* **69**, 2321 (1996).

[93] Q. Wu and X. C. Zhang. Ultrafast electro-optic field sensors. *Applied Physics Letters* **68**, 1604 (1996).

[94] Q. Wu and X. C. Zhang. 7 terahertz broadband GaP electro-optic sensor. *Applied Physics Letters* **70**, 1784 (1997).

[95] Q. Wu and X.-C. Zhang. Design and characterization of traveling-wave electrooptic terahertz sensors. *IEEE Journal of Selected Topics in Quantum Electronics* **2**, 693 (1996).

[96] C. Kübler, R. Huber, and A. Leitenstorfer. Ultrabroadband terahertz pulses: generation and field-resolved detection. *Semiconductor Science and Technology* **20**, S128 (2005).

[97] Y. R. Shen. *The Principles of Nonlinear Optics (Wiley Classics Library)* (Wiley-Interscience, 2002).

[98] K. Liu, J. Xu, and X. C. Zhang. GaSe crystals for broadband terahertz wave detection. *Applied Physics Letters* **85**, 863 (2004).

[99] C. Kübler, R. Huber, S. Tübel, and A. Leitenstorfer. Ultrabroadband detection of multi-terahertz field transients with gase electro-optic sensors: Approaching the near infrared. *Applied Physics Letters* **85**, 3360 (2004).

[100] E. M. Lifshitz, L. D. Landau, and L. P. Pitaevskii. *Electrodynamics of Continuous Media* (Butterworth-Heinemann, 1984), 2nd edition.

[101] M. Born and E. Wolf. *Principles of Optics* (CambridgeUniversity Press, 1998, 1998).

[102] G. Grüner (editor). *Millimeter and Submillimeter Wave Spectroscopy of Solids* (Springer, 1998), 1st edition.

[103] W. J. Duffin. *Electricity and Magnetism* (McGraw Hill Higher Education, 1990), 4th edition.

[104] S. C. Howells and L. A. Schlie. Transient terahertz reflection spectroscopy of undoped InSb from 0.1 to 1.1 THz. *Applied Physics Letters* **69**, 550 (1996).

[105] T. I. Jeon and D. Grischkowsky. Characterization of optically dense, doped semiconductors by reflection THz time domain spectroscopy. *Applied Physics Letters* **72**, 3032 (1998).

[106] A. Pashkin, et al. Phase-sensitive time-domain terahertz reflection spectroscopy. *Review of Scientific Instruments* **74**, 4711 (2003).

[107] S. Nashima, O. Morikawa, K. Takata, and M. Hangyo. Measurement of optical properties of highly doped silicon by terahertz time domain reflection spectroscopy. *Applied Physics Letters* **79**, 3923 (2001).

[108] M. Khazan, R. Meissner, and I. Wilke. Convertible transmission-reflection time-domain terahertz spectrometer. *Review of Scientific Instruments* **72**, 3427 (2001).

[109] M. C. Nuss, D. H. Auston, and F. Capasso. Direct subpicosecond measurement of carrier mobility of photoexcited electrons in gallium arsenide. *Physical Review Letters* **58**, 2355 (1987).

[110] L. Fekete, et al. Ultrafast carrier dynamics in microcrystalline silicon probed by time-resolved terahertz spectroscopy. *Physical Review B* **79**, 115306 (2009).

[111] J. Kitagawa, et al. Terahertz conductivity of localized photoinduced carriers in a Mott insulator $YTiO_3$ at low excitation density, contrasted with the metallic nature in a band semiconductor Si. *Journal of Physics: Condensed Matter* **19**, 406224 (2007).

[112] B. I. Greene, et al. Far-infrared light generation at semiconductor surfaces and its spectroscopic applications. *IEEE Journal of Quantum Electronics* **28**, 2302 (1992).

[113] R. D. Averitt, et al. Conductivity artifacts in optical-pump THz-probe measurements of $YBa_2Cu_3o_7$. *Journal of the Optical Society of America B* **17**, 327 (2000).

[114] H. Wald. Carrier dynamics in $YBa_2Cu_3O_{7-x}$ studied by pump and probe terahertz excitation. *Physica C: Superconductivity* **362**, 324 (2001).

[115] M. C. Hoffmann, et al. THz-pump/THz-probe spectroscopy of semiconductors at high field strengths [invited]. *Journal of the Optical Society of America B* **26**, A29 (2009).

[116] M. C. Hoffmann and D. Turchinovich. Semiconductor saturable absorbers for ultrafast terahertz signals. *Applied Physics Letters* **96**, 151110 (2010).

[117] J. Hebling, et al. Nonlinear optical effects in germanium in the THz range: THz-pump - THz-probe measurement of carrier dynamics. In P. Corkum, et al. (editors), *Ultrafast Phenomena XVI*, volume 92, chapter 214, pages 660–662 (Springer Berlin Heidelberg, Berlin, Heidelberg, 2009).

[118] J. T. Kindt and C. A. Schmuttenmaer. Theory for determination of the low-frequency time-dependent response function in liquids using time-resolved terahertz pulse spectroscopy. *The Journal of Chemical Physics* **110**, 8589 (1999).

[119] E. Knoesel, M. Bonn, J. Shan, and T. F. Heinz. Charge transport and carrier dynamics in liquids probed by THz time-domain spectroscopy. *Physical Review Letters* **86**, 340 (2001).

[120] M. C. Nuss, et al. Dynamic conductivity and coherence peak in $YBa_2Cu_3O_7$ superconductors. *Physical Review Letters* **66**, 3305 (1991).

[121] M. Tinkham. Energy gap interpretation of experiments on infrared transmission through superconducting films. *Physical Review* **104**, 845 (1956).

[122] A. Thoman, A. Kern, H. Helm, and M. Walther. Nanostructured gold films as broadband terahertz antireflection coatings. *Physical Review B* **77**, 195405 (2008).

[123] J. F. Federici, et al. Direct picosecond measurement of photoinduced Cooper-pair breaking in lead. *Physical Review B* **46**, 11153 (1992).

[124] H. Beutler. Über Absorptionsserien von Argon, Krypton und Xenon zu Termen zwischen den beiden Ionisierungsgrenzen $^2P^0_{3/2}$ und $^2P^0_{1/2}$. *Zeitschrift für Physik A Hadrons and Nuclei* **93**, 177 (1935).

[125] U. Fano. Sullo spettro di assorbimento dei gas nobili presso il limite dello spettro d'arco. *Il Nuovo Cimento* **12**, 154 (1935).

[126] U. Fano. Effects of configuration interaction on intensities and phase shifts. *Physical Review* **124**, 1866 (1961).

[127] A. R. P. Rau. Perspectives on the Fano resonance formula. *Physica Scripta* **69**, C10 (2004).

[128] M. Kroner, et al. The nonlinear Fano effect. *Nature* **451**, 311 (2008).

[129] A. E. Miroshnichenko, S. Flach, and Y. S. Kivshar. Fano resonances in nanoscale structures. *Reviews of Modern Physics* **82**, 2257 (2010).

[130] F. Cerdeira, T. A. Fjeldly, and M. Cardona. Effect of free carriers on zone-center vibrational modes in heavily doped p-type Si. II. Optical modes. *Physical Review B* **8**, 4734 (1973).

[131] A. Damascelli, K. Schulte, D. van der Marel, and A. A. Menovsky. Infrared spectroscopic study of phonons coupled to charge excitations in FeSi. *Physical Review B* **55**, R4863 (1997).

[132] S. Lupi, et al. Fano effect in the $a-b$ plane of $\mathrm{Nd_{1.96}Ce_{0.04}CuO_{4+y}}$: Evidence of phonon interaction with a polaronic background. *Physical Review B* **57**, 1248 (1998).

[133] I. Kézsmárki, et al. Variation of the charge dynamics in bandwidth- and filling-controlled metal-insulator transitions of pyrochlore-type molybdates. *Physical Review B* **73**, 125122 (2006).

[134] W. J. Padilla, et al. Infrared signatures of hole and spin stripes in $\mathrm{La_{2-x}Sr_xCuO_4}$. *Physical Review B* **72**, 205101 (2005).

[135] J. D. Lee, J. Inoue, and M. Hase. Ultrafast Fano resonance between optical phonons and electron-hole pairs at the onset of quasiparticle generation in a semiconductor. *Physical Review Letters* **97**, 157405 (2006).

[136] M. Hase, J. Demsar, and M. Kitajima. Photoinduced Fano resonance of coherent phonons in zinc. *Physical Review B* **74**, 212301 (2006).

[137] U. Siegner, M. A. Mycek, S. Glutsch, and D. S. Chemla. Ultrafast coherent dynamics of Fano resonances in semiconductors. *Physical Review Letters* **74**, 470 (1995).

[138] L. C. Davis and L. A. Feldkamp. Interaction of many discrete states with many continua. *Physical Review B* **15**, 2961 (1977).

[139] A. Perucchi, et al. Optical investigation of the metal-insulator transition in $\mathrm{FeSb_2}$. *The European Physical Journal B - Condensed Matter and Complex Systems* **54**, 175 (2006).

[140] M. A. Ordal, et al. Optical properties of the metals Al, Co, Cu, Au, Fe, Pb, Ni, Pd, Pt, Ag, Ti, and W in the infrared and far infrared. *Applied Optics* **22**, 1099 (1983).

[141] M. Dressel and G. Grüner. *Electrodynamics of Solids* (Cambridge University Press, 2002), 1st edition.

[142] G. R. Allcock. On the polaron rest energy and effective mass. *Advances in Physics* **5**, 412 (1956).

[143] J. Appel. Polarons. In F. Seitz, D. Turnbull, and H. Ehrenreich (editors), *Solid State Physics*, volume 21, pages 193–391 (Academic Press, 1968).

[144] L. D. Landau. Über die Bewegung der Elektronen in Kristalgitter. *Physikalische Zeitschrift der Sowjetunion* **3**, 644 (1933).

[145] S. I. Pekar. Issledovanija po ekektronnoj teorii kristallov. *Gostekhizdat, Moskva* (1951).

[146] H. Fröhlich, H. Pelzer, and S. Zienau. Properties of slow electrons in polar materials. *Philosophical Magazine Series 7* **41**, 221 (1950).

[147] H. Fröhlich. Electrons in lattice fields. *Advances in Physics* **3**, 325 (1954).

[148] J. Yamashita and T. Kurosawa. On electronic current in NiO. *Journal of Physics and Chemistry of Solids* **5**, 34 (1958).

[149] T. Holstein. Studies of polaron motion: Part II. The "small" polaron. *Annals of Physics* **8**, 343 (1959).

[150] X. Wu, F. M. Peeters, and J. T. Devreese. Effect of screening on the optical absorption of a two-dimensional electron gas in GaAs-$\mathrm{Al}_x\mathrm{Ga}_{1-x}\mathrm{As}$ heterostructures. *Physical Review B* **34**, 2621 (1986).

[151] G. Q. Hai, F. M. Peeters, and J. T. Devreese. Polaron energy and effective mass in a quantum well. *Physical Review B* **42**, 11063 (1990).

[152] H. M. Rønnow, et al. Polarons and confinement of electronic motion to two dimensions in a layered manganite. *Nature* **440**, 1025 (2006).

[153] L. Perfetti, et al. Spectroscopic indications of polaronic carriers in the quasi-one-dimensional conductor $(\mathrm{TaSe}_4)_2\mathrm{I}$. *Physical Review Letters* **87**, 216404 (2001).

[154] L. Perfetti, et al. Mobile small polarons and the Peierls transition in the quasi-one-dimensional conductor $\mathrm{K}_{0.3}\mathrm{MoO}_3$. *Physical Review B* **66**, 075107 (2002).

[155] ASf for Windows, copyright University of Stuttgart. (2008). Email `steffen.schultz@gmx.de`.

[156] X. X. Bi and P. C. Eklund. Polaron contribution to the infrared optical response of $\mathrm{La}_{2-x}\mathrm{Sr}_x\mathrm{CuO}_{4+\delta}$ and $\mathrm{La}_{2-x}\mathrm{Sr}_x\mathrm{NiO}_{4+\delta}$. *Physical Review Letters* **70**, 2625 (1993).

[157] J. T. Devreese and J. Tempere. Large-polaron effects in the infrared spectrum of high-T_c cuprate superconductors. *Solid State Communications* **106**, 309 (1998).

[158] S. Lupi, et al. Evolution of a polaron band through the phase diagram of $Nd_{2-x}Ce_xCuO_{4-y}$. *Physical Review Letters* **83**, 4852 (1999).

[159] S. Ciuchi and S. Fratini. Signatures of polaronic charge ordering in optical and dc conductivity using dynamical mean field theory. *Physical Review B* **77**, 205127 (2008).

[160] S. Iwai, et al. Ultrafast optical switching to a metallic state by photoinduced Mott transition in a halogen-bridged nickel-chain compound. *Physical Review Letters* **91**, 057401 (2003).

[161] K. Kimura, et al. Ultrafast photoinduced transitions in charge density wave, Mott insulator, and metallic phases of an iodine-bridged platinum compound. *Physical Review B* **79**, 075116 (2009).

[162] A. Damascelli, D. H. Lu, and Z. X. Shen. From Mott insulator to overdoped superconductor: evolution of the electronic structure of cuprates studied by ARPES. *Journal of Electron Spectroscopy and Related Phenomena* **117-118**, 165 (2001).

[163] M. Grioni, S. Pons, and E. Frantzeskakis. Recent ARPES experiments on quasi-1D bulk materials and artificial structures. *Journal of Physics: Condensed Matter* **21**, 023201 (2009).

[164] Z. X. Shen and D. S. Dessau. Electronic structure and photoemission studies of late transition-metal oxides – Mott insulators and high-temperature superconductors. *Physics Reports* **253**, 1 (1995).

[165] A. Damascelli, Z. Hussain, and Z. X. Shen. Angle-resolved photoemission studies of the cuprate superconductors. *Reviews of Modern Physics* **75**, 473 (2003).

[166] A. Damascelli. Probing the electronic structure of complex systems by ARPES. *Physica Scripta* **T109**, 61 (2004).

[167] N. V. Smith, P. Thiry, and Y. Petroff. Photoemission linewidths and quasiparticle lifetimes. *Physical Review B* **47**, 15476 (1993).

[168] R. Haight, et al. Picosecond time-resolved photoemission study of the InP(110) surface. *Physical Review Letters* **54**, 1302 (1985).

[169] H. S. Rhie, H. A. Dürr, and W. Eberhardt. Femtosecond electron and spin dynamics in Ni/W(110) films. *Physical Review Letters* **90**, 247201 (2003).

[170] I. C. E. Turcu, et al. Ultrafast science and development at the Artemis facility. In V. I. Vlad (editor), *ROMOPTO 2009: Ninth Conference on Optics: Micro- to Nanophotonics II*, volume 7469, page 746902 (SPIE, 2009).

[171] R. Manzke, et al. On the phase transitions in $1T$-TaS_2. *Europhysics Letters* **8**, 195 (1989).

[172] T. Pillo, et al. Fine structure in high-resolution photoemission spectra of quasi-two-dimensional $1T$-TaS_2. *Physical Review B* **64**, 245105 (2001).

[173] M. Bovet, et al. Pseudogapped Fermi surfaces of $1T$-TaS_2 and $1T$-TaSe$_2$: A charge density wave effect. *Physical Review B* **69**, 125117 (2004).

[174] L. Perfetti, et al. Unexpected periodicity in the quasi-two-dimensional Mott insulator $1T$-TaS_2 revealed by angle-resolved photoemission. *Physical Review B* **71**, 153101 (2005).

[175] A. M. Woolley and G. Wexler. Band structures and fermi surfaces for $1T$-TaS_2, $1T$-TaSe$_2$ and $1T$-VSe$_2$. *Journal of Physics C: Solid State Physics* **10**, 2601 (1977).

[176] S. Sharma, L. Nordström, and B. Johansson. Stabilization of charge-density waves in $1T$-TaX_2 (X=S,Se,Te): First-principles total energy calculations. *Physical Review B* **66**, 195101 (2002).

[177] M. Bovet, et al. Interplane coupling in the quasi-two-dimensional $1T$-TaS_2. *Physical Review B* **67**, 125105 (2003).

[178] J. K. Freericks, et al. Theoretical description of time-resolved pump/probe photoemission in TaS_2: a single-band DFT+DMFT(NRG) study within the quasiequilibrium approximation. *Physica Status Solidi (B)* **246**, 948 (2009).

[179] X. F. Li, et al. Multiple-harmonic generation in rare gases at high laser intensity. *Physical Review A* **39**, 5751 (1989).

[180] A. L'Huillier and P. Balcou. High-order harmonic generation in rare gases with a 1-ps 1053-nm laser. *Physical Review Letters* **70**, 774 (1993).

[181] P. B. Corkum. Plasma perspective on strong field multiphoton ionization. *Physical Review Letters* **71**, 1994 (1993).

[182] P. B. Corkum and F. Krausz. Attosecond science. *Nature Physics* **3**, 381 (2007).

[183] P. Agostini and L. F. DiMauro. The physics of attosecond light pulses. *Reports on Progress in Physics* **67**, 813 (2004).

[184] F. Frassetto, et al. Design and characterization of the xuv monochromator for ultrashort pulses at the artemis facility. In A. M. Khounsary, C. Morawe, and S. Goto (editors), *Advances in X-Ray/EUV Optics and Components III*, volume 7077, page 707713 (SPIE, 2008).

[185] M. Pascolini, et al. Gratings in a conical diffraction mounting for an extreme-ultraviolet time-delay-compensated monochromator. *Applied Optics* **45**, 3253 (2006).

[186] G. H. Jonker and J. H. Van Santen. Ferromagnetic compounds of manganese with perovskite structure. *Physica* **16**, 337 (1950).

[187] E. Dagotto. *Nanoscale Phase Separation and Colossal Magnetoresistance* (Springer, 2003), 1st edition.

[188] C. Zener. Interaction between the d shells in the transition metals. *Physical Review* **81**, 440 (1951).

[189] J. Kanamori. Crystal distortion in magnetic compounds. *Journal of Applied Physics* **31**, S14 (1960).

[190] P. M. Woodward. Octahedral tilting in perovskites. I. Geometrical considerations. *Acta Crystallographica Section B* **53**, 32 (1997).

[191] S. Jin, et al. Thousandfold change in resistivity in magnetoresistive La-Ca-Mn-O films. *Science* **264**, 413 (1994).

[192] G. C. Xiong, et al. Giant magnetoresistive memory effect in $\mathrm{Nd_{0.7}Sr_{0.3}MnO_2}$ films. *Applied Physics Letters* **67**, 3031 (1995).

[193] Y. Tomioka, et al. Magnetic-field-induced metal-insulator phenomena in $\mathrm{Pr_{1-\mathit{x}}Ca_{\mathit{x}}MnO_3}$ with controlled charge-ordering instability. *Physical Review B* **53**, R1689 (1996).

[194] Y. Tokura and Y. Tomioka. Colossal magnetoresistive manganites. *Journal of Magnetism and Magnetic Materials* **200**, 1 (1999).

[195] J. J. Neumeier, M. F. Hundley, J. D. Thompson, and R. H. Heffner. Substantial pressure effects on the electrical resistivity and ferromagnetic transition temperature of $\mathrm{La_{1-\mathit{x}}Ca_{\mathit{x}}MnO_3}$. *Physical Review B* **52**, R7006 (1995).

[196] C. Zener. Interaction between the d-shells in the transition metals. II. Ferromagnetic compounds of manganese with perovskite structure. *Physical Review* **82**, 403 (1951).

[197] P. W. Anderson and H. Hasegawa. Considerations on double exchange. *Physical Review* **100**, 675 (1955).

[198] J. Kanamori. Superexchange interaction and symmetry properties of electron orbitals. *Journal of Physics and Chemistry of Solids* **10**, 87 (1959).

[199] H. Y. Hwang, T. T. M. Palstra, S. W. Cheong, and B. Batlogg. Pressure effects on the magnetoresistance in doped manganese perovskites. *Physical Review B* **52**, 15046 (1995).

[200] Y. Moritomo, H. Kuwahara, Y. Tomioka, and Y. Tokura. Pressure effects on charge-ordering transitions in perovskite manganites. *Physical Review B* **55**, 7549 (1997).

[201] M. Fiebig, K. Miyano, Y. Tomioka, and Y. Tokura. Visualization of the local insulator-metal transition in $\mathrm{Pr_{0.7}Ca_{0.3}MnO_3}$. *Science* **280**, 1925 (1998).

[202] M. Fiebig, et al. Action spectra of the two-stage photoinduced insulator-metal transition in $\mathrm{Pr}_{1-x}\mathrm{Ca}_x\mathrm{MnO}_3$. *Physical Review B* **60**, 7944 (1999).

[203] M. Fiebig, K. Miyano, Y. Tomioka, and Y. Tokura. Sub-picosecond photo-induced melting of a charge-ordered state in a perovskite manganite. *Applied Physics B: Lasers and Optics* **71**, 211 (2000).

[204] Y. Okimoto, et al. Optical study of $\mathrm{Pr}_{1-x}\mathrm{Ca}_x\mathrm{MnO}_3$ ($x = 0.4$) in a magnetic field: Variation of electronic structure with charge ordering and disordering phase transitions. *Physical Review B* **59**, 7401 (1999).

[205] A. V. Boris, et al. Infrared optical properties of $\mathrm{La_{0.7}Ca_{0.3}MnO_3}$ epitaxial films. *Journal of Applied Physics* **81**, 5756 (1997).

[206] M. Rini, et al. Control of the electronic phase of a manganite by mode-selective vibrational excitation. *Nature* **449**, 72 (2007).

[207] S. Kaiser, et al. Controlling "Mottness" in a correlated electron system via coherent vibrational excitation. In *International Conference on Ultrafast Phenomena*, OSA Technical Digest (CD), page ThC5 (Optical Society of America, 2010).

[208] D. A. G. Deacon, et al. First operation of a free-electron laser. *Physical Review Letters* **38**, 892 (1977).

[209] I. B. Bernstein and J. L. Hirshfield. Theory of a free-electron laser. *Physical Review Letters* **40**, 761 (1978).

[210] Z. Huang and K. J. Kim. Review of x-ray free-electron laser theory. *Physical Review Special Topics - Accelerators and Beams* **10**, 034801 (2007).

[211] S. A. Zvyagin, et al. Terahertz-range free-electron laser electron spin resonance spectroscopy: Techniques and applications in high magnetic fields. *Review of Scientific Instruments* **80**, 073102 (2009).

[212] P. Michel, et al. First lasing at the ELBE mid-IR FEL. In *Proceedings of the 26th International Free Electron Laser Conference, Trieste, Italy, 29 August3 September 2004*, page MOAIS04 (2004).

[213] U. Lehnert, et al. First experiences with the fir-fel at elbe. In *Proceedings of the 29th International Free Electron Laser Conference, Novosibirsk, Russia, 2631 August 2007*, page MOPPH036 (2007).

[214] W. Seidel, et al. Remote controlled IR-diagnostic station for the FEL at Rossendorf. In *Proceedings of the 28th International Free Electron Laser Conference, Berlin, Germany, 27 August - 1 September 2006*, page TUPPH015 (2006).

[215] S. T. Cundiff. Phase stabilization of ultrashort optical pulses. *Journal of Physics D: Applied Physics* **35**, R43 (2002).

[216] D. J. Jones, et al. Carrier-envelope phase control of femtosecond mode-locked lasers and direct optical frequency synthesis. *Science* **288**, 635 (2000).

[217] A. Baltuška, T. Fuji, and T. Kobayashi. Controlling the carrier-envelope phase of ultrashort light pulses with optical parametric amplifiers. *Physical Review Letters* **88**, 133901 (2002).

[218] R. Huber, A. Brodschelm, F. Tauser, and A. Leitenstorfer. Generation and field-resolved detection of femtosecond electromagnetic pulses tunable up to 41 THz. *Applied Physics Letters* **76**, 3191 (2000).

[219] C. Manzoni, M. Först, H. Ehrke, and A. Cavalleri. Single-shot detection and direct control of carrier phase drift of midinfrared pulses. *Optics Letters* **35**, 757 (2010).

[220] M. Först, et al. Coherent polarons in ferromagnetic $La_{0.7}Sr_{0.3}MnO_3$. In *International Conference on Ultrafast Phenomena*, OSA Technical Digest (CD), page ME46 (Optical Society of America, 2010).

[221] R. I. Tobey, D. Prabhakaran, A. T. Boothroyd, and A. Cavalleri. Ultrafast electronic phase transition in $La_{1/2}Sr_{3/2}MnO_4$ by coherent vibrational excitation: Evidence for nonthermal melting of orbital order. *Physical Review Letters* **101**, 197404 (2008).

[222] D. Fausti, et al. Photo-induced superconductivity in charge ordered LESCO ($La_{1.8-x}Er_{0.2}Sr_xCuO_4$, $x = 0.125$). In *International Conference on Ultrafast Phenomena*, OSA Technical Digest (CD), page MG4 (Optical Society of America, 2010).

[223] R. J. D. Miller, et al. 'Making the molecular movie': first frames. *Acta Crystallographica Section A* **66**, 137 (2010).

[224] R. Neutze, et al. Potential for biomolecular imaging with femtosecond X-ray pulses. *Nature* **406**, 752 (2000).

[225] H. N. Chapman, et al. Femtosecond diffractive imaging with a soft-X-ray free-electron laser. *Nature Physics* **2**, 839 (2006).

[226] M. Chergui. Picosecond and femtosecond X-ray absorption spectroscopy of molecular systems. *Acta Crystallographica Section A* **66**, 229 (2010).